ISAS - INTERNATIONAL SCHOOL FOR ADVANCED STUDIES

First-Principles Study of α-Sn Surfaces

Thesis submitted for the degree of

"Doctor Philosophiæ"

CANDIDATE

Zhong-Yi LU

SUPERVISORS

Dott. Guido L. Chiarotti

Dott. Sandro Scandolo

Prof. Erio Tosatti

October 1996

SISSA - SCUOLA INTERNAZIONALE SUPERIORE DI STUDI AVANZATI

TRIESTE

Strada Costiera 11

TRIESTE

Table of Contents

1 General Introduction

Essentially all semiconductor surfaces are reconstructed. As is well known, this can be traced back to the strong covalency of their bulk band structure, where valence electronic states s and p hybridize to form sp^3 filled bonding states and empty anti-bonding states with a large energy gap in between. At surfaces, hybridized sp^3 bonds are cut, and become dangling bonds. The corresponding dangling-bond electronic surface states fall in the bulk energy gap, and are only half filled. As a result, ideal semiconductor surfaces should be strongly metallic and possess a very high surface energy. The uniqueness of covalent systems, as opposed to, for example, regular metals, is that bulk covalent bonding is very directional and relatively inflexible. Consequently, it generally costs too much energy to locally rearrange the electron wave functions at the surface as required by the presence of dangling bonds, without major lattice readjustments. Reconstructions represent in this sense a useful compromise, in that they are able to eliminate dangling bonds as much as possible.

Often, reconstructions include a partial electron-charge-transfer mechanism, often without a major disturbance to the deeper layers. This artificial surface ionicity is controlled by surface atomic displacements, e.g. buckling, and represents one

example of Anderson's "negative U"[1]. This kind of surface ionic phenomena in a system which is purely covalent in the bulk is less pronounced for lower atomic numbers. Valence p states are more localized in C than in Si, Ge and Sn, and are more and more extended with increasing atomic number. Correspondingly, the intra-atomic Coulomb repulsion decreases with increasing atomic number.

The reconstructions of semiconductor surfaces tend to preserve the surface bond lengths close to the bulk value as much as possible. Let us consider a second-order expansion of the total energy δE in terms of atomic displacements with respect to a set of stable points[2],

$$\delta E = \frac{k_r}{2} \sum_{pairs\ ij} (dr_{ij})^2 + \frac{k_\theta r^2}{2} \sum_{angles\ ijk} (d\theta_{ijk})^2,$$

where dr_{ij} is the change of the bond length between nearest neighbors i and j (bond stretching), $d\theta_{ijk}$ denotes the change of the angle between the pairs ij and jk (bond bending) controlled by the radial and angular force constants, k_r and k_θ respectively, and r is the equilibrium distance between the nearest neighbors. For Si, the bond stretching force constant k_r is about 8.7 eV/Å while the bond bending force constant k_θ is only 0.29 eV/Å [3]. Since $k_r >> k_\theta$, the surface bond length will try to remain close to the bulk value. In practice, when we have no better information, we can begin to build reconstruction models with initial bond lengths equal to the bulk value.

Of course, a surface reconstruction is a balance between several factors of saturating dangling bonds, electron charge transfer, ionic energy and so on. Because of the complexity of this balance, a semiconductor surface may have several local free energy mimima corresponding to different reconstructions. In real life, the observed

surface reconstruction will be the lowest free energy structure kinetically accessible under the given preparation conditions. For example, the cleaved Si(111) and Ge(111) structures are the 2×1 π-bonded chain reconstruction, whereas annealing to high temperatures produces the Si(111)-(7×7)-DAS (Dimer-Adatom-Stacking-Fault) and Ge(111)-$c(2 \times 8)$ adatom reconstructions, respectively. The latter can be proven to represent, at $T = 0$, the ground states of Si(111)and Ge(111), respectively. The 2×1 states are the lowest energy states which can be built without adatoms. which come about only after annealing. Finally, we address the role of temperature. Starting with a kinetically constructed phase, temperature will generally convert irreversibly the surface into a lower free energy, genuine equilibrium reconstruction. So, for example, Ge and Si(111) surfaces switch irreversibly from the 2×1 π-bonded chain to the adatom reconstructions. At higher temperatures, reconstructed surfaces deconstruct, which usually implies a loss of the extra periodicities, and the recovery of a 1×1 unit cell.

Existing work on group IV semiconductor surfaces focuses on Si, Ge and C. After C, Si and Ge, Sn is the last group IV element with a diamond structure, i.e., α-Sn (grey tin). It has a lattice parameter of 6.483 Å (at 90 K) [4], and shows a semimetal character (i.e., zero-band-gap semiconductor.). Sn is thus the sort of a brigde element in group IV semiconductors from insulator, semiconductor to metal. When the temperature is raised to 286 K at atmospheric pressure or pressure is raised to 5 Kbar at zero temperature, α-Sn transforms into the fully metallic β-Sn (white tin) phase. β-Sn has a double body-centered tetragonal structure of its own, with lattice parameters a=5.8317 Å and c=3.1813 Å at 298 K, and its space

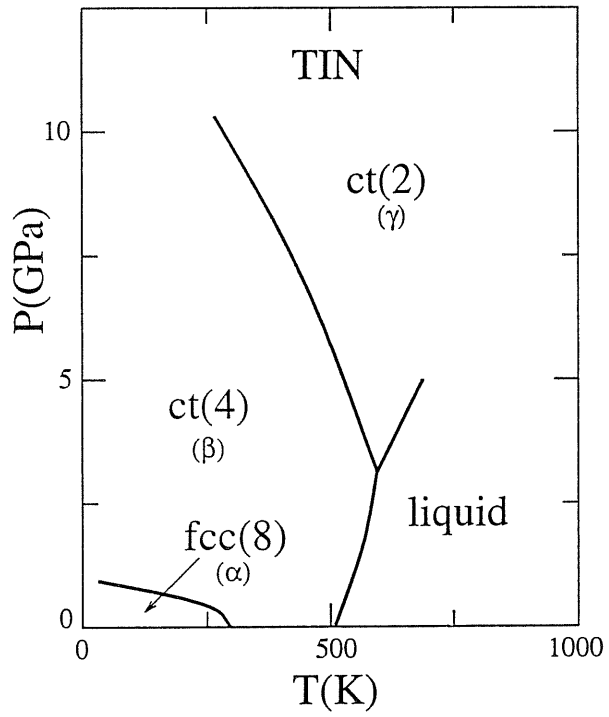

Figure 1.1: The phase diagram of Sn

group is $I4_1/amd$. The melting temperature of β-Sn is 505 K. Upon increasing the pressure to 9.4 GPa at room temperature, β-Sn further tranforms into γ-Sn. The structure of γ-Sn is body-centered tetragonal with lattice parameters $a = 3.81\mathring{A}$, $c = 3.48\mathring{A}$ at 3.9 GPa and 587 K, and its space group is $I4/mmm$. The overall phase diagram[5] of tin is shown in Fig.1.1

While a large number of experiments and calculations have clarified the nature of bulk Sn, the situation is different for Sn surfaces, where only recently some groups[6, 7] have been successful in growing α-Sn(111) and α-Sn(100) on InSb(111) and InSb(100) using molecular beam expitaxy (MBE) (single crystals of α-Sn appear

Table 1.1: Summary of different reconstruction mechanisms for (111) semiconductor surfaces.

	C	Si	Ge
2×1 π-bonded chain	dimerized (*) (?)	buckled	more buckled
adatom/ rest atom	not found	7×7 DAS(*)	c(2×8) adatom (*)
2×1 buckled	not found	saddle-point	saddle-point
metallic	graphitic $T \geq 2700$K (?)	$T \geq 1500$K (?)	$T \geq 1050$K

(*) Stable structure at $T = 0$.

(?) Pending confirmation.

difficult to obtain). These data indicate for α-Sn(111) a metastable 3×3 structure turning to 2×2 upon annealing[7], and for α-Sn(100) $p(2 \times 2)$ and $c(4 \times 4)$ structures appear, respectively, when grown α-Sn is 500-1000 Å and 1000-2500 Å thick[6]. At the moment of writing no theoretical calculations (apart from those printed in this thesis) are available for α-Sn surfaces. It is expected that the interest in α-Sn surfaces will rapidly grow in the near future due to the potential applications of some of these surfaces, and to the availability of fine experimental techniques, such as, STM, XPS, which can be used on the thin epitaxial films.

This thesis is, therefore, devoted to the first theoretical study of α-Sn (111) and (100) surfaces. In particular, since there are no conclusive structural data available, *ab initio* calculations are crucial in comparing various possible reconstruction mechanisms, and understanding the trends relative to the other semiconductors.

Systematic investigation of Diamond, Si and Ge (111) and (100) surfaces, both theoretically and experimentally, indicate that a variety of different reconstruction mechanisms are realized. A summary is presented in Tables 1.1 and 1.2.

As seen in Table 1.1 and 1.2, essentially all (111) surfaces possess a π-bonded

Table 1.2: Summary of differen reconstructions for (100) semiconductor surfaces.

	C	Si	Ge
2 × 1- dimer reconstruction	symmetric	buckled	more buckled
high order reconstruction	not found	p(2 × 2), c(4 × 2)	p(2 × 2), c(4 × 2)

chain 2 × 1 reconstructed state. As a true ground state, however, π-bonded chains only prevail in diamond, either reflecting the difficulty of obtaining well annealed adatoms on this surface or the high energetic cost of ionic adatoms in carbon.

Finally, Table 1.1 considers, as further types of reconstruction, either simple buckling or the possible transformation of a thin surface layer from semiconducting to metallic. Simple buckling, the so-called Haneman model, never really prevails, and is considered for completeness, and for its simplicity. The possibility of surface metallization is suggested by the bulk phase diagrams of Si, Ge and Sn, where fully metallic phases completely surround the semiconducting phases, under any combination of either high pressure or temperature. There is considerable evidence that surface metallization does in fact play a relevant role on Ge(111), at high temperatures[8], and there is a prediction that it should prevail at $T = 0$ on Ga(001)[9]. It might perhaps be relevant to α-Sn, due to the bulk metallic β-Sn phase being very close to α-Sn in energy, as is the case of Ga[9].

The second surface to be considered in this thesis is α-Sn(100). In the (100) surfaces, well-known 2 × 1 dimer reconstructed structures are stable in C, Si and Ge. Simple 2 × 1 structure prevails in Diamond, while the ground state for both Si (100) and Ge (100) surface is $c(4 \times 2)$ or $p(2 \times 2)$ reconstruction, which are almost degenerate. These $c(4 \times 2)$ and $p(2 \times 2)$ reconstructed states consist also of

dimers, which constitute the basic building blocks. Recent *ab initio* calculations[10] suggest a symmetric 2×1 dimer reconstruction of Diamond(100). On Si(100) and Ge(100) surfaces, the symmetric dimer structure is metallic and energetically higher than the asymmetric dimer structure with 0.4 Å and 0.8Å buckling on Si and Ge, respectively, as shown by experiments[11, 12] and confirmed by both tight binding [13] and *ab initio* calculations[10, 14, 15]. Experiments and calculations indicate that the $c(4 \times 2)$ and $p(2 \times 2)$ reconstructions consist of asymmetric dimer structures.

By extrapolating the trends of Table 1.1 and 1.2 we are led to expect the following: for α-Sn (111), (i) the 2×1 π-bonded chain reconstruction should be present, with an even larger buckling than in Ge;
(ii) This reconstruction will be in energetic competition with some adatom/restatom reconstructions, the latter being likely to prevail;
(iii) A surface metallization mechanism might be possible because of the closeness of the metallic β-Sn in energy.
For α-Sn (100), we expect that
(i) the 2×1 dimer reconstruction will probably also take place in α-Sn(100), with a larger buckling than in Si and Ge. As in Si and Ge, the symmetric dimer structure should be metallic and energetically higher than the asymmetric dimer structure;
(ii) as on Si and Ge (100) surfaces[16], several high order reconstructions, for instance $c(4 \times 2)$ and $p(2 \times 2)$, will compete for the ground state structure, which consists of asymmetric dimers with large bucklings.

In this work we shall find that (apart from metallization, which turns out to be a harder problem) these trends are generally well borne out by our *ab initio*

calculations.

For the α-Sn(111) surface, a 2×1 π-bonded chain reconstruction prevails in the absence of adatoms, and a $c(4 \times 2)$ or (2×2) basic adatom-restatom unit reconstruction does otherwise, and accompanying surface bucklings or relaxations are in both cases larger than in Si and Ge, with consequently large ionic charge transfers predicted. The annealed 2×2 phase could be explained by a simple adatom-restatom reconstruction. As for the metastable (3×3) reconstruction observed in experiment[7]. our calculation places them energetically much higher than the (2×2) adatom-restatom model. There are two further possibilities: either we did not optimize the best (3×3) structure, or we did it and the reason it still appears at low growth temperatures is an out-of-equilibrium phenomenon.

For α-Sn(100) surface, the expected 2×1 asymmetric dimer structure was confirmed to possess a much lower energy than that of symmetric dimer structure as in Si and Ge and unlike diamond. The asymmetric dimer buckling is large (about 1 Å) compared with 0.4 Å and 0.74 Å in Si and Ge (100) surfaces[11, 12], respectively. This reconstruction is the basic building block for high-order reconstructions in which $p(2 \times 2)$ and $c(4 \times 2)$ reconstructions are best among all considered possibilities.

This thesis is organized as follows. In the next chapter I will briefly describe the computational methods, and some key technical points related to our calculations. In chapter III and IV, the calculated results for Sn(111) and (100) will be described, respectively. Finally, I will summarize the results and further discuss them in chapter V.

2 Computational Method, Bulk Properties of α and β Sn

2.1 Computational Method

In the present *ab initio* calculations for α-Sn (bulk and surface) and β-Sn (bulk), we use the first-principles pseudopotential plane-wave self-consistent calculation method[17] which is based on the density functional theory (DFT) within the local density approximation (LDA)[18, 19].

Based on the Born-Oppenheimer, or adiabatic approximation we are able to decouple the electronic and ionic degrees of freedom of a solid. Futhermore, we can regard the ions as classical particles, due to their huge mass, while the electrons are regarded as a quantum many-body system. For any given set of ionic positions, the Hamiltonian describing the quantum system of the electrons is

$$\mathcal{H} = T + U + V_{ext}, \tag{2.1}$$

where T is the electronic kinetic energy, U is the electron-electron interaction, and V_{ext} is the external potential due to the ions or other possible external sources such as electric fields.

Hohenberg and Kohn[18] proved that as for as the ground state of Hamiltonian (2.1) is considered the electron charge density $n(\vec{r})$ uniquely determines the external potential, the ground state wavefunction $|\Psi>$ and all other electronic properties of the system. Thus the ground state wavefunction $|\Psi>$ is a function of $n(\vec{r})$, the expectation value of Hamiltonian (2.1) in the ground state can be written as:

$$\begin{array}{c} <\Psi|\mathcal{H}|\Psi>= E_{tot}[n(\vec{r})] = F[n(\vec{r})] + \int d\vec{r} V_{ext}(\vec{r}) n(\vec{r}), \\ F[n(\vec{r})] =<\Psi|T+U|\Psi> . \end{array} \tag{2.2}$$

As proposed by Kohn and Sham[19], the above many-body system can be mapped onto a single-particle noninteracting system whose density is equal to $n(\vec{r})$.

Introducing the single-particle orbitals $\phi_i(\vec{r})$, the density is written as

$$n(\vec{r}) = \sum_i |\phi_i(\vec{r})|^2, \tag{2.3}$$

and the density functional $F[n(\vec{r})]$ as (in atomic units):

$$F[n] = -\frac{1}{2}\sum_i <\phi_i(\vec{r}|\nabla^2|\phi_i(\vec{r})> + \frac{1}{2}\int d\vec{r} d\vec{r}' \frac{n(\vec{r})n(\vec{r}')}{|\vec{r}-\vec{r}'|} + E_{xc}[n]. \tag{2.4}$$

Eq. (2.4) defines the new quantity $E_{xc}[n]$, known as the exchange-correlation functional. Now the variation of the total energy $E_{tot}[n]$ with respect to the density $n(\vec{r})$, combined with the constraint $\int n(\vec{r}) d\vec{r} = N$ (N is the total number of electrons), results in the following set of single-particle equations (Kohn-Sham equations):

$$\begin{array}{c} \mathcal{H}_{KS}\phi_i(\vec{r}) = (-\nabla^2 + \int \frac{n(\vec{r}')}{|\vec{r}-\vec{r}'|} d\vec{r}' + V_{xc}(\vec{r}))\phi_i(\vec{r}) = \epsilon_i \phi_i(\vec{r}), \\ n(\vec{r}) = \sum_i \theta(\epsilon_i - \epsilon_F)|\phi_i(\vec{r})|^2, \end{array} \tag{2.5}$$

where the exchange-correlation potential is the functional derivative

$$V_{xc}(\vec{r}) = \frac{\delta E_{xc}[n]}{\delta n(\vec{r})},$$

and ϵ_F is the Fermi energy.

Since the exact functional form of $E_{xc}[n]$ is unknown, various different approximations have been proposed, the most common being the local density approximation (LDA). LDA assumes that the density $n(\vec{r})$ is slowly varying in space so that the uniform-electron gas approximation holds locally, and $E_{xc}[n]$ can be expressed in the form:

$$E_{xc}[n] = \int d\vec{r}\epsilon_{xc}(n(\vec{r}))n(\vec{r}), \tag{2.6}$$

where $\epsilon_{xc}(n)$ is the exchange and correlation energy per electron of a uniform electron gas of density n. In our calculations, we adopted the Ceperley-Alder exchange and correlation potential functional with the parameterization of Perdew and Zunger[20].

We use a plane-wave basis set to expand the single-particle Kohn-Sham (KS) orbitals. Having the Bloch form, the KS orbitals can be expanded as:

$$\phi_{n\vec{k}}(\vec{r}) = e^{i\vec{k}\cdot\vec{r}}u_{n\vec{k}}(\vec{r}) = \sum_{\vec{G}} e^{i(\vec{k}+\vec{G})\cdot\vec{r}}C_{n\vec{k}}(\vec{G}), \tag{2.7}$$

where $u_{n\vec{k}}(\vec{r})$ is a periodic Bloch function, $\vec{G}$ is a reciprocal lattice vector, $\vec{k}$ is a vector belonging to the first Brillouin Zone of the crystal, and n denotes the band index. The use of a plane-wave basis set has invaluable numerical advantages such as the simple form of the kinetic energy in the Kohn-Sham Hamiltonian, and in the use of Fast-Fourier-transformations (FFT) to deal with real-space terms such as the exchange and correlation potential. Also, the use of a plane-wave basis set is completely independent of the structure of the considered system so that results obtained for different structures can be directly compared with each other. The

plane wave basis set is determined, for each value of $\vec{k}$, by

$$|\vec{k} + \vec{G}|^2 \leq E_{cut}, \tag{2.8}$$

where E_{cut} is a fixed kinetic energy cutoff. A rough estimate of the number of plane waves is given by

$$N_{PW} \approx \frac{4\pi}{3\Omega_{BZ}}(E_{cut})^{\frac{3}{2}}, \tag{2.9}$$

where Ω_{BZ} is the volume of the Brillouin Zone.

In order to avoid the huge number of plane waves required to describe strongly localized core electrons and the rapid oscillations of the valence wavefunctions in the core region, the electron-ion interaction is modeled by pseudopotentials. Since the physics of bonding in solids is dominated by the valence electrons, the main idea underlying the use of pseudopotential is to map the all-electron system onto an equivalent system including only the valence electrons, where "pseudo"-wavefunctions are made smooth in the core regions. Widely used first-principles pseudopotentials are the *ab initio* norm-conserving Hamann, Schluter, and Chiang (HSC) pseudopotentials[21, 22]. The main features of these pseudopotentials are: (i) real and pseudo valence eigenvalues are the same for a chosen all-electron atomic configuration; (ii) real and pseudo valence atomic wavefunctions agree beyond a chosen "core radius" r_c; (iii)integrals from 0 to r of the real and pseudo wavefunctions are equal for $r > r_c$ for each valence state (norm conservation); (iv) the logarithmic derivatives of the real and pseudo wavefunctions and their first energy derivatives are equal beyond core radius r_c. Properties (iii) and (iv) guarantee the pseudopotentials to have the optimum transferability to different chemical environments. However, to take these

Table 2.1: Coefficients of the pseudopotential of Sn in the Kleinman-Bylander form from Ref.[24] with notation of Ref.[22].

L	α_1	α_2	α_3	c_1	c_2	c_3	c_4	c_5	c_6
core	2.00	0.80		5.1824	-4.1824				
0	1.47	1.86	2.93	-6.8310	0.4151	0.1260	0.2234	0.0285	-0.0176
1	1.30	1.63	2.01	-5.6815	0.5008	-0.0901	0.1155	0.0710	0.0124
2	1.11	1.36	1.45	-5.7003	0.1856	-0.2167	-0.0772	-0.0653	-0.0191

norm conservation rules into account the pseudopotentials are forced to be nonlocal, i.e. angular momentum dependent, which is computationally very costly. Kleinman and Bylander[23] showed that a significant reduction of the computational effort can be acheived by transforming the original semi-local (i.e. non-local in angular coordinates but local in radial coordinates) HSC pseudopotential into a fully non-local form[23].

We use, in our calculations, an *ab-initio* norm-conserving pseudopotential[24] in the Kleinman-Bylander form[23]. This pseudopotential is constructed by fitting its pseudo eigenvalues and eigenfunctions to a relativistic all-electron self-consistent calculation where spin averaging is performed to produce the l-components of the pseudopotentials.

The parameters of this pseudopotential, with the notation of Bachelet, Hamann and Schluter[22], are listed in the Table 2.1.

The surface properties of α-Sn have been studied by standard slab calculations. Periodic boundary conditions are in fact unavoidable in plane-wave calculations, and surfaces have to be dealt with using periodically repeated slabs of finite height, separated by a vacuum layer that has to be sufficiently thick to avoid spurious

interactions between the slabs. In almost all calculations presented, the slab contains twelve atomic layers plus a vacuum layer of 11 Å . We checked convergence using ten atomic layers and 9 Å vacuum to compute the surface energies of the 2×2 adatom-restatom reconstruction on Sn(111) and the 2×1 symmetric-dimer reconstruction on Sn(100). The surface energies changed by less than 4 meV/(1×1 cell). The detailed geometries for the different surfaces will be illustrated in the respective chapters.

Tests on the convergence of the results with respect to the kinetic energy cutoff are described in the next section, and show that for our choice of the pseudopotential, 12 Ryd is the proper energy cutoff for both bulk and surface calculations.

Most of the reconstructed surfaces we deal with require the use of large supercells. In order to perform large-scale electronic structure calculations, we employed the powerful block Davidson's iterative scheme[25] to solve the single-particle Kohn-Sham Hamiltonian, and the modified Broyden scheme[26] to accelerate convergence in the iterative procedure for the self-consistent solution. We optimized (relaxed) the considered surface structures by moving atoms according to the calculated Hellmann-Feynman forces by means of the Broyden-Fletcher-Goldfarb-Shannon algorithm[27]. Surface structures are considered optimized when the residual Hellmann-Feynman forces on atoms are less than 5 meV/Å.

Surface Brillouin Zone (SBZ) integration is a delicate issue, particularly when comparing the surface energies of different reconstructed surface calculations. We adopted the following strategy: we first computed the surface energy for the ideal surface and test its convergence with respect to k-point summation. We then considered the ideal surface as the reference state, and performed a variety of reconstructed

surface calculations using a k-point sampling equivalent to that of the ideal case, i.e. obtained by refolding the set of k-points of the ideal surface onto the SBZ of the reconstructed surfaces under consideration. This equivalence would however lead in some cases, as, for instance, in the α-Sn(111) 3×3 reconstruction to an untreatable number of k-points. In these cases, we repeated the ideal surface calculations using a different and more appropriate k-point sampling, and carefully testing the k-summation independence of the results. When we met metallic surfaces, we also used a Gaussian broadening of 0.001 Ryd and first order approximation for the Fermi distribution function[28]. This procedure allows a safe comparison of surface energies for different surfaces, with an overall resolution in surface energy differences of 5 meV/(1 × 1 cell). The detailed SBZ k-point sampling will be illustrated in the following chapters.

In the next part of this section, we illustrate how we compute the surface electronic band structure, the surface work function, and the layer-projected density of states, that are all the physical quantities relevant to the interpretation of our results.

Surface Electronic Band Structure: When the Kohn-Sham equations are self-consistently solved on the finite grid of k-points specified above, one obtains the self-consistent electronic charge density. Using this self-consistent density we solve the Kohn-Sham equation along the chosen high-symmetry axes of the irreducible part of the Surface Brillouin Zone (ISBZ), and construct the slab electronic band structure. In order to resolve contributions due to surface states we also calculate the surface projected bulk electronic bands. The surface bands thus clearly show up

in the projected bulk gap regions.

Surface Work function: The surface work function is one of the most typical electronic properties of a surface, and can be directly measured in experiments. The surface work function ϕ is defined as $\phi = \bar{V}_H(vacuum) - E_F$, where E_F is the Fermi energy and $\bar{V}_H(\vec{r})$ is the macroscopic average of the Hartree potential $V_H(\vec{r})$. The Hartree potential $V_H(\vec{r})$ satisfies Poisson's equation

$$\nabla^2 V_H(\vec{r}) = 4\pi\rho(\vec{r}) \tag{2.10}$$

and can easily be obtained from the self-consistent electronic charge density. Following the approach proposed by Baldereschi, Baroni and Resta[29], we compute $\bar{V}_H$ using

$$\bar{V}_H(z) = \frac{1}{a}\int_{z-a/2}^{z+a/2} ds \int_{S_0} dxdy V_H(x,y,s), \tag{2.11}$$

where S_0 is the surface unit area, a is the α-Sn bulk lattice parameter, and z is the coordinate normal to the surface. Physically, $\bar{V}_H(z)$ should be constant in the vacuum and central region of the slab.

Layer-projected Density of States (LDOS): In real space, at position $\vec{r}$, the local density of states $\rho(\vec{r}, E)$ of the slab is defined as

$$\rho(\vec{r}, E) = \sum_n \int_{SBZ} d\vec{k} |\Psi_{\vec{k}}^{(n)}(\vec{r})|^2 \delta(E - E_n(\vec{k})), \tag{2.12}$$

where n is the band index, $\Psi^{(n)}$ and E_n are the eigenstate and eigenvalue of th nth band, respectively. Integration over the whole slab yields the total density of states $\rho(E)$ of the slab which contains contributions from both the surface and the bulk. If the slab has no vacuum region or if the number of atomic layers of the slab goes

to infinity, $\rho(E)$ becomes the exact bulk density of states. $\rho(\vec{r}, E)$ can be projected onto the different atom layers in the slab as:

$$\rho(m, E) = \sum_n \int_{SBZ} d\vec{k} \int_{S_0} dxdy \int_{z_m-\Delta/2}^{z_m+\Delta/2} dz |\Psi_{\vec{k}}^{(n)}(x, y, z)|^2 \delta(E - E_n(\vec{k})), \quad (2.13)$$

where z_m denotes the mth atom-layer position, and Δ is the distance between two nearest neighbor atom-layers. This LDOS will resemble the bulk density of states $\rho(E)$ in the central atom-layer of the slab. By comparison, the LDOS in the surface layer or the second layer will display the distribution of the surface states. The LDOS is a relevant quantity and can be used to interpret angular integrated photoemission spectroscopy experiments. In our practical calculation, due to the finite resolution of our k-point sampling, we replaced the δ-function in formula (2.13) by a Gaussian function with a broadening of 25 meV.

2.2 Bulk Properties

We have first calculated the bulk properties of α and β Sn, in order to check the pseudopotential choice and the calculation scheme, and also to determine the energy cutoff to be used in the surface calculations.

The zero temperature structure of bulk Sn is the α phase with a diamond lattice [32] of lattice spacing 6.483 Å (at 90 K) [4]. If the temperature is raised to 286 K at atmospheric pressure, semimetallic α-Sn transforms into the fully metallic β-Sn phase[33]. Under pressure, this transformation occurs at lower temperatures. Extrapolating the experimental data to T=0 K[33, 34] indicates a transformation pressure of 0.5 GPa. This differs from Si and Ge which instead maintain the diamond

Table 2.2: Calculated lattice parameter, bulk moduli (K_0) and its pressure derivative (DK_0), and bulk energy (E_{bulk}) for bulk α-Sn phase are listed, respectively, for different energy cutoffs E_{cut}. Corresponding experimental values are also listed in the last line. RT denotes the room temperature.

E_{cut}	a_0	K_0	DK_0	E_{bulk}
Ryd	Å	GPa		Ryd/atom
35	6.442	43.80	4.330	-7.12031
30	6.442	43.80	4.330	-7.12014
25	6.441	43.80	4.341	-7.11900
20	6.441	44.20	4.318	-7.11599
15	6.442	44.35	4.273	-7.11337
12	6.446	44.21	4.311	-7.11119
10	6.476	43.83	3.819	-7.10060
Exp.	6.491[RT][a]	53[90 K][b]		

[a]Reference [30]
[b]Reference [31]

structure up to more than 8 GPa. Although α-Sn and β-Sn are energetically very close, they differ completely in their atomic structure and electronic properties. α-Sn is a zero-band-gap semiconductor with diamond structure, while β-Sn is a complete metal with double-bct (body center tetregonal) structure.

It is well known that relativistic effects play an important role in heavy element systems. In particular, the zero-band-gap semiconducting property of α-Sn is primarily attributed to relativistic effects[35, 17]. The *ab initio* total energy LDA calculations of J.L. Corkill *et al.*[34] included scalar-relativistic effects and confirmed that at zero temperature and zero pressure the β phase is energetically very close to the α phase, their energy difference being 44 meV/atom, with a transition pressure to the β phase of 0.8 GPa. Were the relativistic effects not included[36], a worse agreement with experiments would be obtained. In the present *ab-initio* calculations for α-Sn and β-Sn, we do consider relativistic effects in our pseudopotential, including only scalar effects, as described above.

Although α-Sn is a zero-band gap semiconductor, its band structure in whole Brillouin Zone has a gap except at the Γ point. For the α-Sn bulk calculation, we thus used 10 special k-points[38] to sample the Irreducible Brillouin Zone (IBZ) of the diamond phase. For the metallic β phase, instead, we find that 160 k-points are needed to describe accurately the IBZ summations, with an additional Gaussian broadening of 0.14 eV [28]. We have tested that increasing the k-point integration to 24 special k-points and 200 k-points in the IBZ of α-Sn and β-Sn phases, respectively, alters these results only within $\sim$5 meV. For simplicity, we fixed the c/a ratio of β-Sn to the experimental value of 0.546.

Table 2.3: Calculated lattice parameter, bulk moduli (K_0) and its pressure derivative (DK_0), and bulk energy (E_{bulk}) for the bulk β-Sn phase are listed, respectively, for different energy cutoffs E_{cut}. Corresponding experimental values are also listed in the last line. RT denotes the room temperature.

E_{cut}	a_0	K_0	DK_0	E_{bulk}
Ryd	Å	GPa		Ryd/atom
35	5.765	54.21	4.736	-7.11875
30	5.765	54.15	4.737	-7.11855
25	5.765	54.16	4.733	-7.11735
20	5.763	54.31	4.755	-7.11410
15	5.762	54.50	4.772	-7.11140
12	5.764	54.87	4.775	-7.10950
10	5.778	55.37	4.613	-7.09985
Exp.	5.820[RT][a]	54.9[RT][b]		

[a]Reference [30]
[b]Reference [37]

Table 2.4: The energy difference ΔE between bulk β-Sn and bulk α-Sn and the pressure inducing structural phase transition from *alpha*-Sn to β-Sn are listed, respectively, for different energy cutoffs E_{cut}, The last line lists the known experimental value.

E_{cut}	ΔE	P
Ryd	meV/atom	GPa
35	21.2	0.50
30	21.6	0.50
25	22.4	0.50
20	25.7	0.50
15	26.8	0.50
12	23.0	0.50
10	10.2	0.30
Exp.		0.5(0 K)[a]

[a]reference [39]

We have also checked the dependence of plane-wave expansion of various physical properties of both α and β-Sn on the cutoff, ranging from 35 Ryd to 10 Ryd. The dependence of the energy difference between α-Sn and β-Sn and their transition pressure on the cutoff were also checked.

Results for lattice parameter a_0, bulk moduli K_0 and its pressure derivative DK_0, total energy, and energy difference between the two phases are reported in Table 2.2(α-Sn), Table 2.3(β-Sn) and Table 2.4. As can be seen, for any energy cutoff higher than 12 Ryd, the β-phase is disfavored with respect to the α-phase by the same energy (23.0 meV/atom) within our accuracy. Also, the $\alpha \rightarrow \beta$ transition pressure of 0.50 GPa is in exact agreement with experiments. On the contrary, if

the energy cutoff is lower than 12 Ry, the transition pressure becomes 0.30 GPa (at 10 Ryd) and the energy difference drops to 10.2 meV/atom. Thus, 12 Ryd cutoff can be considered to reproduce accurately enough the experimental results, and will be adopted for all the surface calculations.

The electronic band structure of α-Sn is reported in Fig. 2.1 and that of β-Sn[40] in Fig. 2.2. As can be seen, in particular, the semimetallic character of the α-phase (zero gap only at Γ) and the fully metallic character of the β-phase are correctly borne out in our calculations. This is at variance with the calculation by J.L.Corkill *et. al.*[17] where the first conduction band dips below the top valence band at Γ point, i.e. their calculated band gap is negative. This fact was artificially attributed by the authors to the local density approximation and the neglect of spin-orbit effects.

The excellent success of our LDA calculations in predicting these extremely delicate energy differences in bulk phases provides confidence in extending this approach towards exploring surface properties.

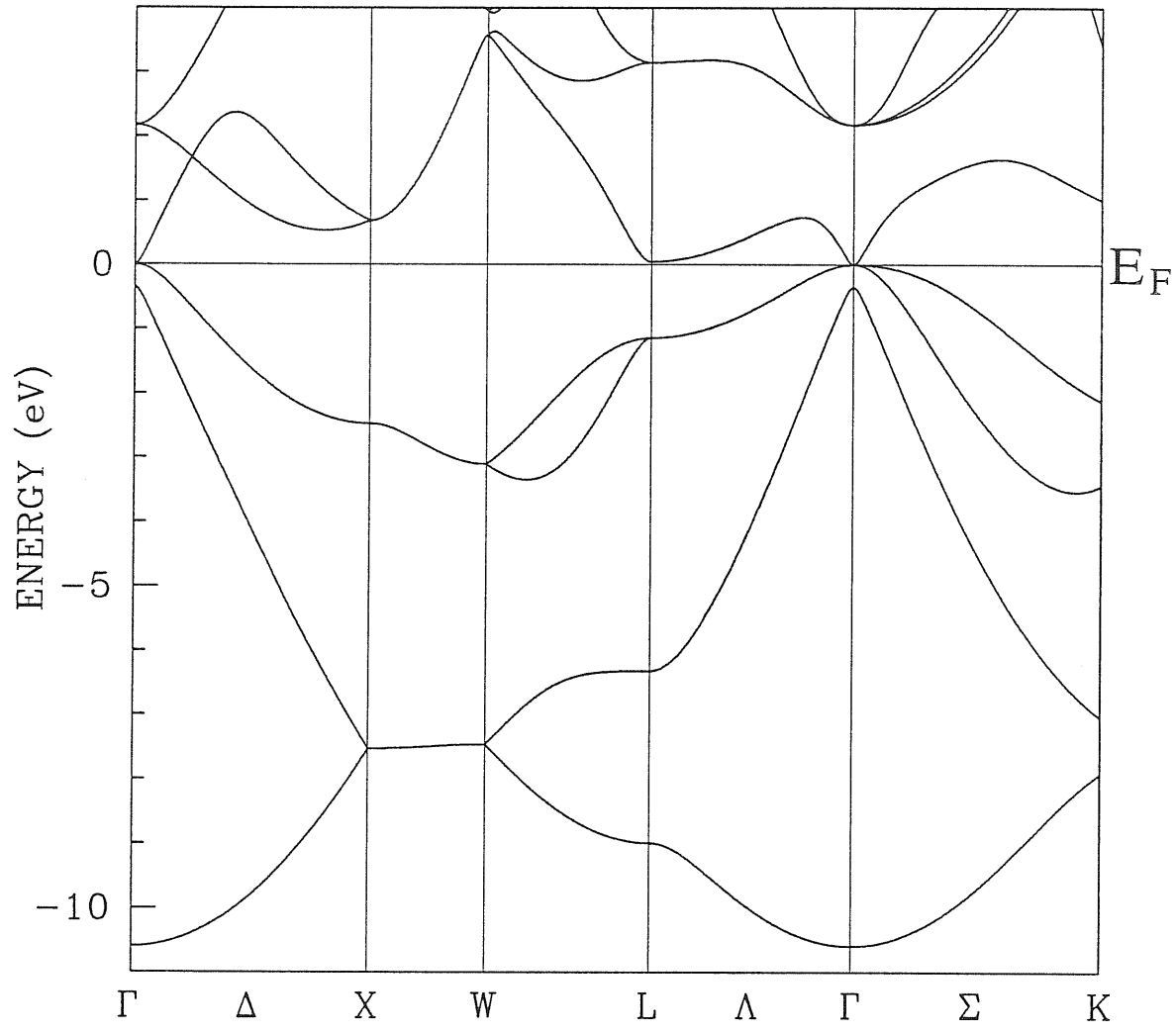

Figure 2.1: Electronic structure of bulk α-Sn. The zero in energy corresponds to the Fermi level.

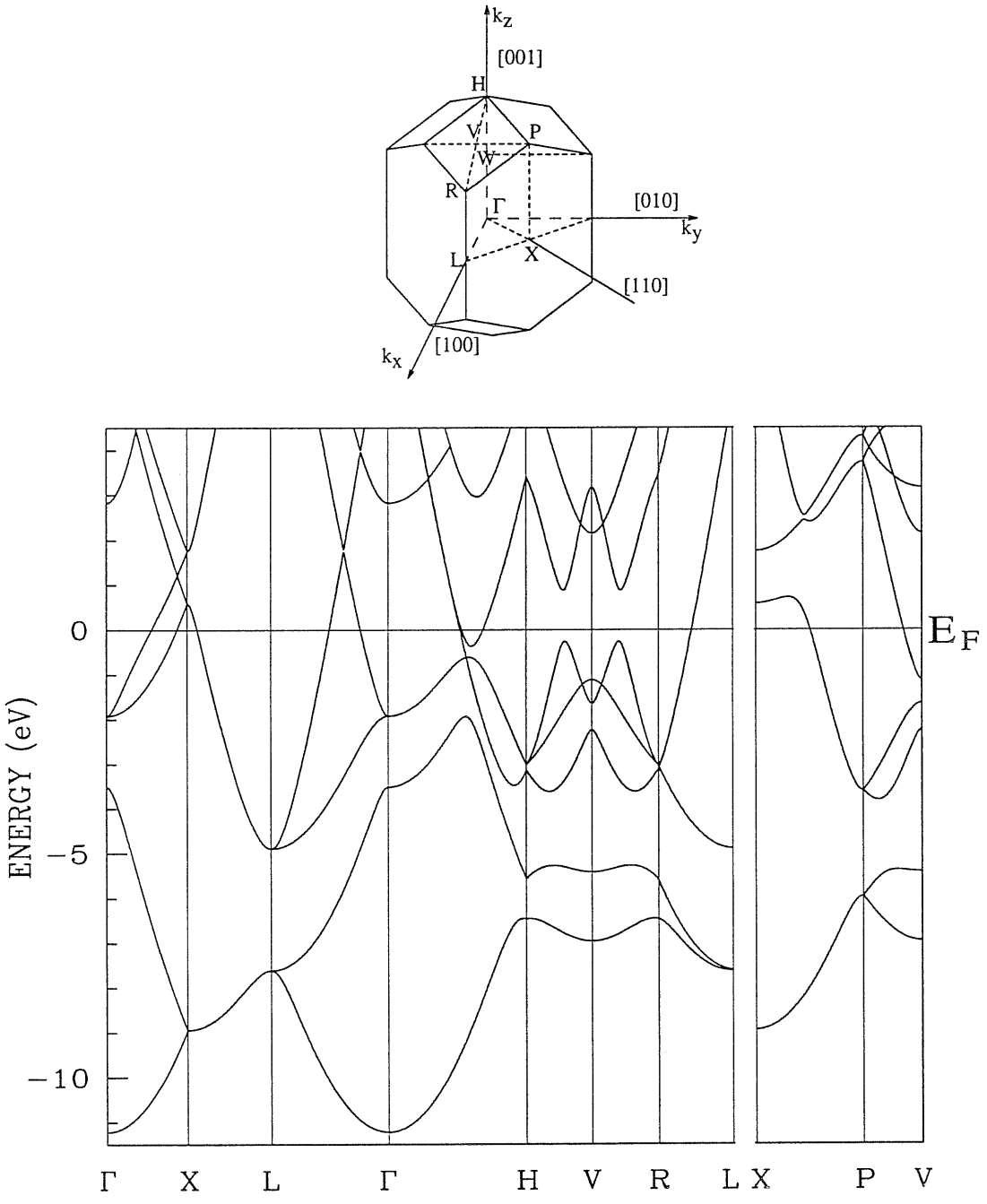

Figure 2.2: Brillouin zone and electronic structure of bulk β-Sn. The zero in energy corresponds to the Fermi level.

3 The α-Sn (111) Surfaces

This chapter is organized as follows. First of all, in Sect. 3.1 we deal with the ideal, unreconstructed α-Sn (111) surface, whose properties we study without and with surface relaxation. We find partly filled dangling bond states in the ideal surface electronic structure, which as usual suggest that this is not a stable surface. This is confirmed in next section—Sect. 3.2, where a simple 2×1 buckled (Haneman) reconstruction is shown to lower the surface energy without energy barriers. The more interesting π-bonded chain reconstruction is considered in Sect. 3.3. It is found that a very strongly buckled 2×1 π-bonded chain state exists for α-Sn (111), its energy being lower than that of the Haneman state. Sect. 3.4 is devoted to the alternative possibility of adatom/restatom reconstructions. We find this latter possibility to be energetically most favourable, both in the (2×2) and in the $c(4 \times 2)$ local geometry. This therefore suggests that the stable annealed (2×2) surface structure observed in experiment[7] is of the adatom-restatom type. The (3×3) reconstructions suggested by experiment[7] are considered in Sect. 3.5. We consider two models, a Dimer-Adatom-Stacking-Fault (DAS) model and a distorted $\sqrt{3} \times \sqrt{3}$ model. It is found that their surface energies are higher than that of the 2×2

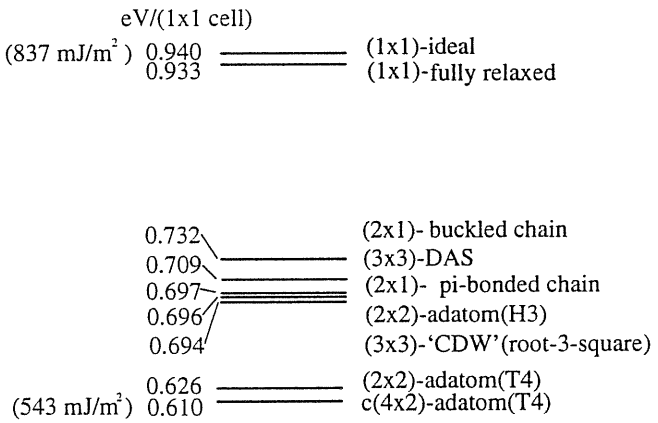

Figure 3.1: The calculated surface energies for α-Sn(111) surfaces

adatom-restatom model, which is at best compatible with metastability of this kind of 3×3 structures. In Sect. 3.6 we briefly describe an attempt to find a stable metallic reconstructed surface ground state, which however turns out to be inconclusive. Our calculated surface energies are schematically and tabularly reported in Fig. 3.1 and Table 3.7, respectively.

3.1 The Relaxed, Unreconstructed α-Sn (111) Surface

We study the surface properties of α-Sn (111) by a standard slab calculation, as described in Chapter 2. One of the two surfaces of the slab is frozen in its ideal geometry, together with the first three adjacent layers (a total of two rigid bilayers). The atoms belonging to the remaining layers are allowed to fully relax guided by the corresponding Hellmann-Feynman forces. Convergence is assumed when forces

are less than 5 meV/Å . The number of atomic layers in the slab is fixed in this case to a total of 12 layers (not including the adatom layer when present). Each layer consists of either one, two, or four Sn atoms, in correspondence to choosing 1×1, 2×1, and 2×2 [or $c(4 \times 2)$] surface cells, respectively. The number of "vacuum layers" is fixed to 6 (vacuum thickness $\sim$ 11 Å), and the number of k points in the Irreducible Surface BZ (ISBZ) is chosen according to the size of the surface cell and its geometry, as described case by case. The initial atomic positions are chosen according to the calculated equilibrium bulk lattice spacing ($a_o = 6.446$ Å). This guarantees that the forces on the atoms of the central layers are smaller than 4 meV/Å for all the surfaces studied. In all cases, surface energies E_{surf} are given as $E_{surf} = E_{slab} - NE_{bulk} - E_{surf}^{ideal}$, where E_{slab} is the total energy of the slab, E_{bulk} is the energy per atom of bulk α-Sn as computed in Sect. 2.2 [E_{bulk}=-96.753 eV/atom][41], N is the total number of atoms in the slab. Furthermore, $E_{surf}^{ideal} = [E_{slab}^{ideal} - NE_{bulk}]/2$ is the energy of the frozen ideal surface. Here E_{slab}^{ideal} is the total energy of a slab with both surfaces rigid and ideal, computed using the same supercell geometry and k-point set as E_{slab}. We therefore have to repeat ideal surface calculations several times in different supercells and k-point sets corresponding to different surface reconstruction slab calculations in order to compare different reconstructed surface energies. The convergence of our results with respect to the k-points sampling has been tested for each surface by increasing the k-point number after the atomic relaxation. Accordingly, we can estimate our overall energy resolution to be better than 10 meV/(1×1 cell). We have also calculated the full electronic band structure of the relaxed surfaces. This was done by using the

Kohn-Sham eigenvalues of a 10-layer slab, obtained by removing the seven bottom layers of the simulation slab and replacing them by the inverted image of the topmost five relaxed layers. The reason for this procedure is threefold. First, we get rid of the undesired states related to the bottom rigid ideal surface. Second, we increase the effective symmetry of the supercell, thus decreasing the computational effort of the band structure calculation. Third, although the interaction of identical surface states belonging to opposite surfaces generally lifts their degeneracy (again an undesired effect), their average energy still corresponds, to second order in their coupling, to the noninteracting value in the ideal case of an infinite slab.

As a first case we have considered the (1×1) unreconstructed surface. Six special k-points in the hexagonal ISBZ have been used [42]. The electronic band structure of the ideal (1×1) surface is reported in Fig. 3.2. There are various surface states lying in the projected gaps. The surface states crossing the Fermi level inside the fundamental gap are clearly related to the presence of unsaturated surface dangling bonds. This feature is common to all group IV insulators and semiconductors, and is responsible for the high grade of instability of the ideal (111) surface, as mentioned in Chapter 1. The electron density corresponding to the surface state is analysed in Fig. 3.3, and reveals a high degree of surface localization as well as a clear dangling-bond character.

As a next step, we allowed the surface, i.e. all atoms in the eight topmost surface layers, to relax, according to the Hellmann-Feynman forces, so as to reduce the surface energy. Despite the presence of unsaturated dangling bonds, the result of this energy minimization shows that surface atoms do not relax significantly (see Table

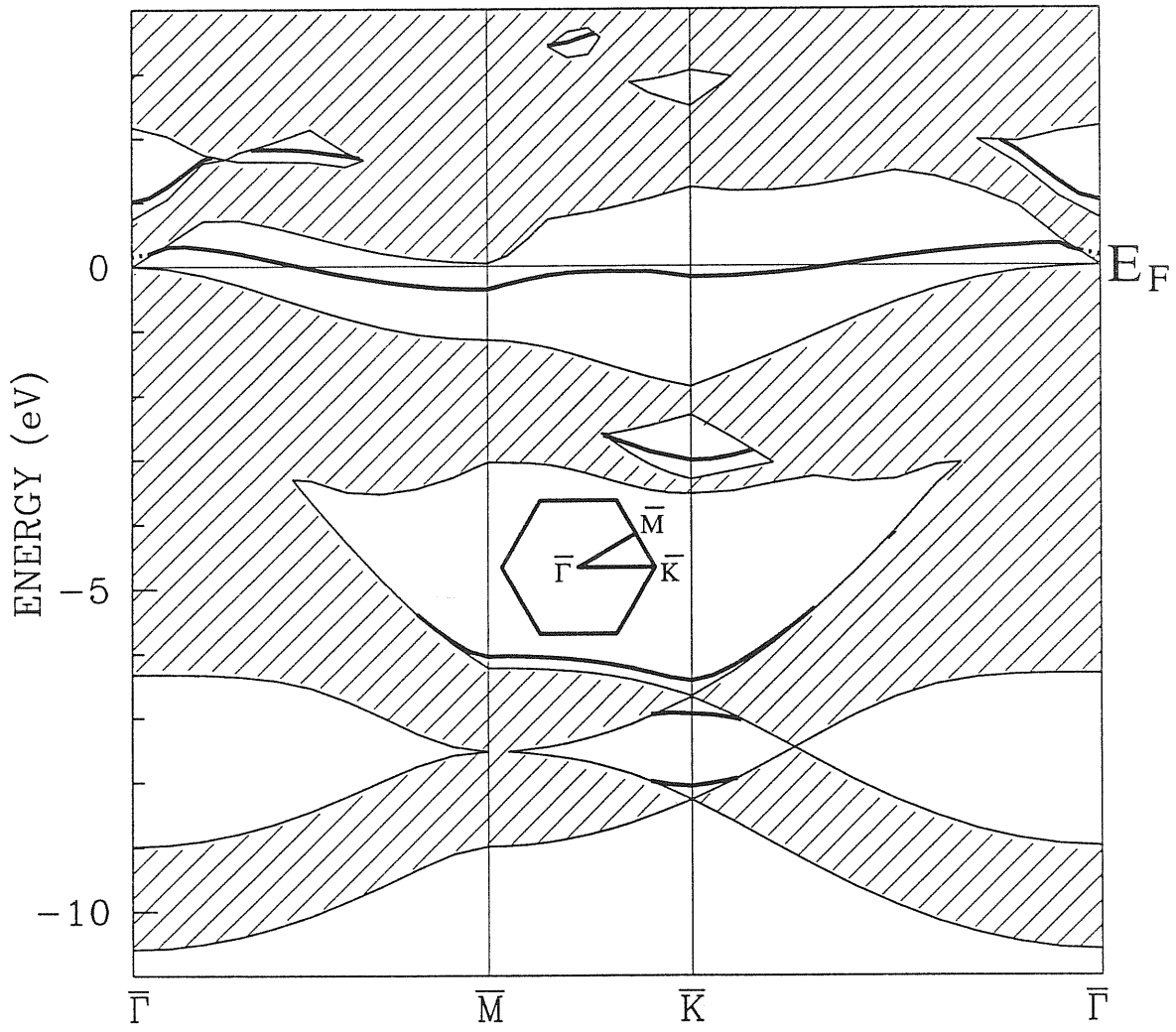

Figure 3.2: Surface electronic structure of the ideal α-Sn(111) surface reported along high-symmetry lines of the (1 × 1) hexagonal irreducible Brillouin zone. Shaded areas correspond to surface-projected bulk states, while thicker lines correspond to surface states. The surface Brillouin zone is given in the inset. Note that the dangling bond surface state crosses the fermi level E_F.

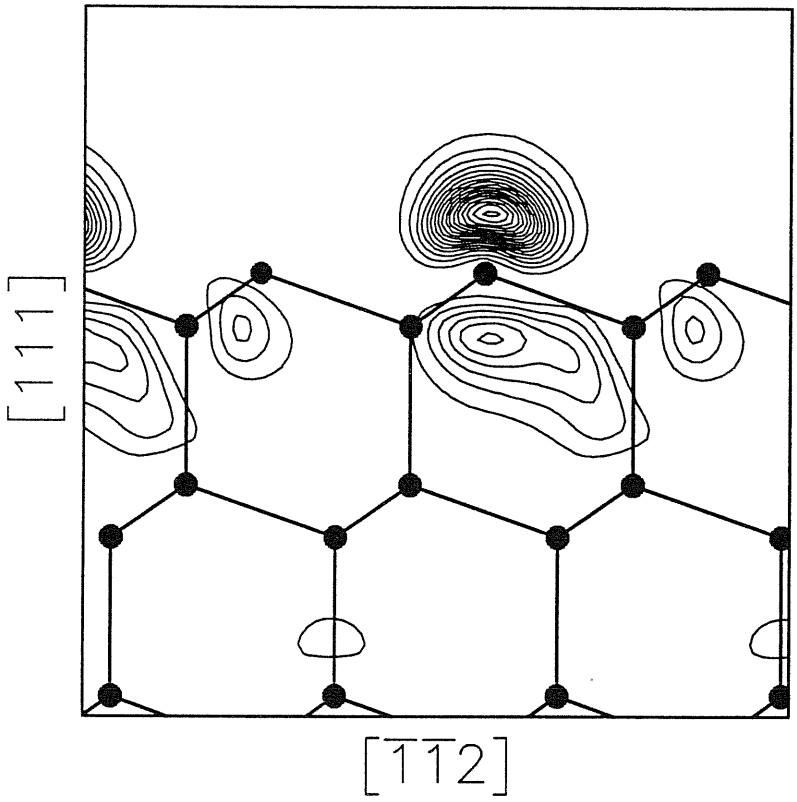

Figure 3.3: Electron density contour of the highest occupied state of the ideal α-Sn(111)-(1 × 1) surface at $\bar{K}$, on the (110) plane passing through top atoms. Full circles correspond to Sn atoms, and thicker straight lines to bonds among Sn atoms. Contour lines are separated by 0.0005 (a.u.). Note the dangling bond character of this state.

3.7), with a surprisingly small surface energy gain of only 7 meV/$(1 \times 1)cell$, and a downward relaxation of the top layer of 0.02 Å . We also checked that increasing the k-point number from six to eighteen changed none of the above results.

3.2 Haneman (2×1) "Buckled Atom" Reconstruction

In the preceding calculation, relaxation was allowed, but reconstruction was forbidden by symmetry. If the symmetry constraints imposed by the choice of a (1×1) cell are relaxed, the ideal surface is provided with a simple mechanism for the partial saturation of the dangling bonds. Such a mechanism, first proposed by Haneman [43], consists of a simple in-out buckling of the topmost layer, resulting in a (2×1) displacive reconstruction. The inward motion of one surface atom implies an $sp^3 \rightarrow sp^2$ rehybridization, and a p_z-like dangling bond for that atom. The outward motion of the other atom, by contrast, causes dehybridization, and an s-like dangling bond. Since in the atom $E_s << E_{p_z}$, electrons will flow from the inward to the outward relaxed atom. This charge transfer empties and saturates respectively the two dangling bonds and therefore removes partly filled surface states from the gap, stabilizing the surface. This buckled (2×1) reconstruction, although actually never observed, has been recently suggested to play the role of a transition state, a kind of "stepping stone", in the dynamical process leading from an unreconstructed state towards, e.g., a (2×1) π-bonded chain state[44]. In order to study the possible occurence of such a buckled atom reconstruction on α-Sn (111), we have repeated our calculation in a (2×1) surface cell, using 4 special k-points in the rectangular (2×1) ISBZ[42]. We find, indeed, that the surface spontaneously buckles as in

the Haneman distortion just described, against which the ideal surface is therefore unstable, very much as Ge (111)[44]. The energy gain from the ideal to the optimal buckled geometry (Table 3.7), is about 0.22 eV/$(1 \times 1)cell$, measured relative to the energy of the ideal surface computed using the same (2×1) supercell and k-point set. The buckling of the top layer is found to be enormous, namely 1.23 Å . The final atomic coordinates of the relaxed top five atomic layers are given in Table 3.1.

3.3 (2×1) π-Bonded Chain Reconstruction

The instability of the ideal (111) surface against (2×1) buckling is interesting, but probably academic, except possibly in dynamics, or in some local region where it can be rehybridized by a defect. In our pursuit of the true (111) ground state surface structure, we consider next the surface reconstruction geometries which are experimentally observed in the other group-IV insulator and semiconductors. Here we consider the (111) 2×1 π-bonded chain reconstruction. In the lack of any experimental and theoretical data, we arranged the surface atoms in the structure proposed by Pandey [45]. Pandey's structure can be obtained by simultaneously suppressing one surface atom into the second layer and correspondingly raising one second layer atom, so that i) the number of dangling bonds per surface atom is the same as before; ii) all bond lengths are set to the bulk value. The atomic coordinates in Pandey's structure are given in Table 3.3. Subsequently, we allowed the atomic positions to relax according to *ab-initio* forces, using the same supercell and same k-point sampling as in the previous section. At convergence, we find that

Table 3.1: Ideal, and optimized atomic positions of the α-Sn (111) (2×1) buckled (Haneman) surface. In the rectangular supercell, coordinates are given by $\mathbf{r} = c_1\mathbf{a}_1 + c_2\mathbf{a}_2 + c_3\mathbf{a}_3$, where $\mathbf{a}_i$ is defined in the conventional cubic coordinate system as $\mathbf{a}_1 = (a_0/2)(-1, 2, -1)$, $\mathbf{a}_2 = (a_0/2)(-1, 0, 1)$, $\mathbf{a}_3 = a_0(1, 1, 1)$ and a_0 (=6.446 Å) is the lattice parameter.

	Atom	Ideal			Optimal		
	no.	c_1	c_2	c_3	c_1	c_2	c_3
buckled-layer							
	1	.000	.000	.000	.009	.000	-.048
	2	.500	.500	.000	.485	.500	.062
2nd-layer							
	3	.167	.500	.083	.132	.500	.077
	4	.667	.000	.083	.692	.000	.077
3rd-layer							
	5	.167	.500	.333	.169	.500	.330
	6	.667	.000	.333	.667	.000	.332
4th-layer							
	7	.333	.000	.417	.334	.000	.415
	8	.833	.500	.417	.836	.500	.417
5th-layer							
	9	.333	.000	.667	.334	.000	.665
	10	.833	.500	.667	.833	.500	.667

Table 3.2: The magnitude of buckling, the bond length, and the buckling angle of the π-bonded chain in C, Si, Ge, and α-Sn (111) surfaces.

	buckling length (Å)	bond length (Å)	buckling angle
C[a]	0	1.44	0°
Si[b]	0.4	2.25	10°
Ge[c]	0.8	2.42	19°
α-Sn[d]	1.15	2.80	24.25°

[a]Reference [47] (calculated value).
[b]Reference [11] (measured value).
[c]Referenec [44] (measured value).
[d]This work.

the energy gain of this 2 × 1 reconstruction, with respect to the ideal surface, is 0.24 eV/(1 × 1)*cell* (Table 3.7), i.e., slightly larger than that of the buckled 2 × 1 reconstruction. The optimal atomic coordinates of the top five atomic layers are given in Table 3.3. The bond lengths within the π-bonded chain are 2.80 Å , only 0.4 % longer with respect to the ideal bulk bond length (2.79 Å). The chain buckling (1.15 Å) is however very large if compared with that of Si or Ge (0.4 Å [46, 11], and 0.8 Å [44], respectively), fully confirming the trends discussed in Section I and listed in Table 1.1. The π-bonded chain of α-Sn thus forms an angle of $\theta = 24.25°$ with the (111)-plane, (θ is defined as: $\sin\theta =$ *chain buckling length/chain bond length*). This value is again very large if compared with that of Si and Ge, and in the trend from C to Si. to Ge, and to α-Sn (see Table 3.2). The magnitude of this buckling

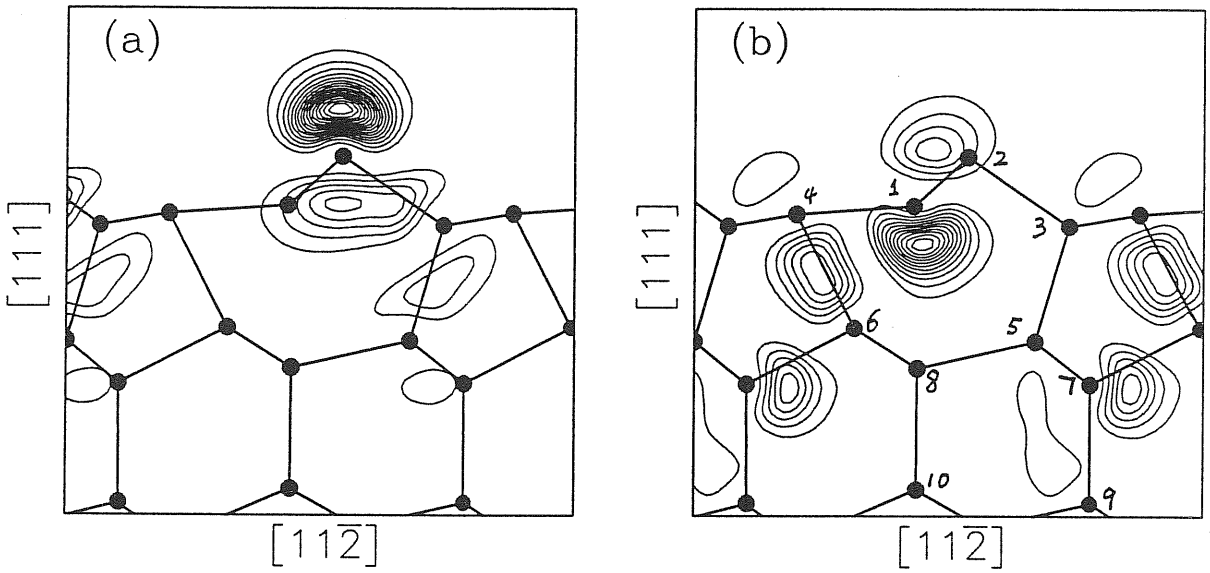

Figure 3.4: Electron density contours of the highest occupied state (panel (a)) and of the lowest unoccupied state (panel (b)) in the α-Sn(111) (2×1) π-bonded chain reconstruction at $\bar{J}$, on the (110) plane passing through the up (down) atom. In panel (b) atoms are labelled according to the optimal positions of Table 3.3. Contour lines are separated by 0.0005 (a.u.).

is so large, that the whole π-bonded chain is now lying onto an essentially vertical plane (see Fig. 3.4). The large chain buckling is accompanied by a large electron transfer from the lowered to the raised chain atom, which again tends to saturate the raised atom dangling bond, and empty the lowered one. This is clearly seen in Fig. 3.4, where the charge distributions of the highest occupied (panel (a)) and lowest unoccupied states (panel (b)) are shown. This charge rearrangement is accompanied by the opening of a large gap in the dangling bond surface state, as seen in the electronic structure of Fig. 3.5. Here the highest occupied (lowest unoccupied)

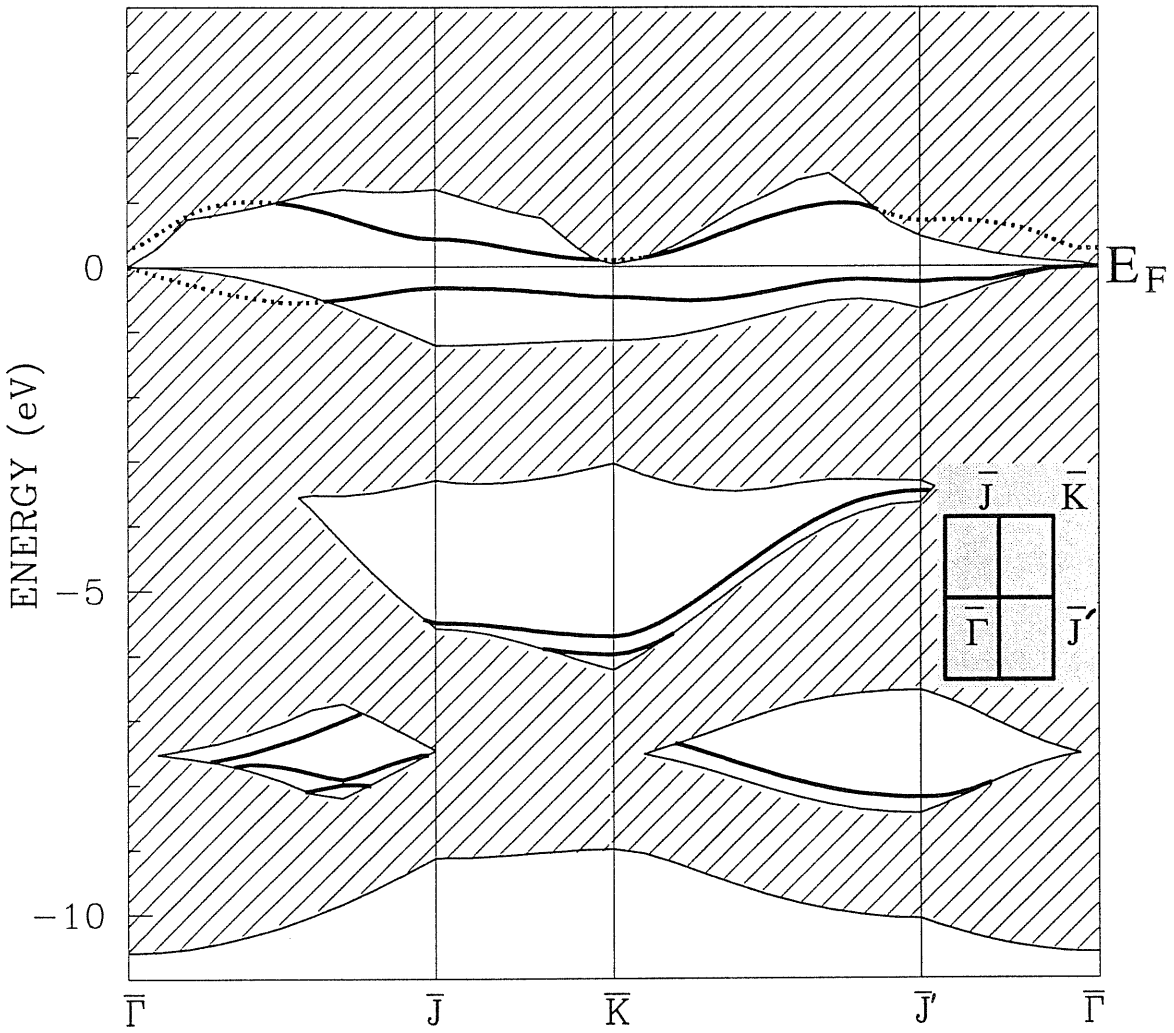

Figure 3.5: Surface electronic structure of the α-Sn(111) (2 × 1) π-bonded chain reconstructed surface reported in the (2 × 1) rectangular irreducible Brillouin zone (see inset). Shaded areas correspond to surface-projected bulk states, while thicker lines correspond to surface states. The dangling bond band is now split into two bands. The splitting of the original dangling bond state is evident.

surface states correspond to raised (lowered) atom dangling bonds, respectively. Finally, since the alternative possibility of a dimerization of the chain was excluded in our cell due to symmetry constraints, we tried slightly dimerizing the initial, unbuckled π-bonded chain, and also the final, fully buckled one (thereby doubling the number of k-points in the ISBZ). However, we found these configurations to be energetically disfavored with respect to the undimerized chain.

3.4 Adatom-Restatom Reconstructions

As the next likely candidate for the reconstruction of α-Sn (111), we now consider an adatom-restatom reconstruction, known to be the stable mechanism for both Si and Ge. Although this reconstruction shows up with rather more complex surface unit cells, such as the (7×7) DAS model in Si[48] and the $c(2 \times 8)$ in Ge[49], the building block of this class of reconstructions is simple. It is based on the presence of one adatom every four (1×1) first-layer atoms. The adatom sits in a threefold site, saturating three first-layer atoms, leaving one (the restatom) unsaturated[50]. Of the two available threefold sites, namely T_4 (on top of a second-layer atom), and H_3 (hollow site), the adatoms prefer, at least in Si and Ge[50, 51], the T_4 site. Moreover, the T_4 site adatoms may still be arranged in a (2×2) or $c(4 \times 2)$ geometry. For instance in Ge (111) $c(2 \times 8)$, they are stacked in alternating (2×2) and $c(4 \times 2)$ cells. Here we assume the pure (2×2) [or pure $c(4 \times 2)$] T_4 structure as the prototype adatom-restatom reconstruction, restricting for simplicity our analysis to this case only.

As was the case for the π-bonded chain reconstruction, we have no data to guide

Table 3.3: Initial (Pandey's), and optimized atomic positions of the α-Sn (111) (2 × 1) π-bonded surface. In the rectangular supercell, coordinates are given by $\mathbf{r} = c_1\mathbf{a}_1 + c_2\mathbf{a}_2 + c_3\mathbf{a}_3$, where $\mathbf{a}_i$ is defined in the conventional cubic coordinate system as $\mathbf{a}_1 = (a_0/2)(-1, 2, -1)$, $\mathbf{a}_2 = (a_0/2)(-1, 0, 1)$, $\mathbf{a}_3 = a_0(1, 1, 1)$ and a_0 (= 6.446 Å) is the lattice parameter.

	Atom	Pandey's[a]			Optimal		
	no.	c_1	c_2	c_3	c_1	c_2	c_3
π-bonded layer							
	1	-.148	.000	.023	-.167	.000	.060
	2	-.019	.500	.023	-.020	.500	-.043
2nd-layer							
	3	.315	.500	.106	.278	.500	.100
	4	.519	.000	.106	.484	.000	.077
3rd-layer							
	5	.167	.500	.333	.178	.500	.341
	6	.667	.000	.333	.657	.000	.317
4th-layer							
	7	.333	.000	.417	.336	.000	.431
	8	.833	.500	.417	.831	.500	.400
5th-layer							
	9	.333	.000	.667	.337	.000	.678
	10	.833	.500	.667	.834	.500	.654

[a]For corresponding bulk-like positions, see the ideal case of Table 3.1.

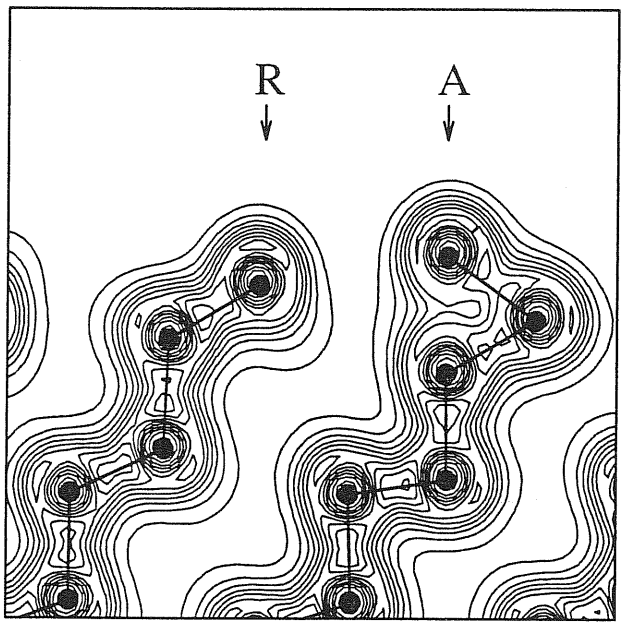

Figure 3.6: Geometry, and electron density contour of the α-Sn(111) (2×2) adatom / restatom reconstruction, on the plane passing through the adatom and the rest atom. Contour lines are separated by 0.005 (a.u.). Note the strong outward relaxation of the restatom, and the strong inward relaxation of the second and third layer atoms beneath the adatom. (R: restatom, A: adatom)

us. We start with an ideal T_4 position for the adatom (see Table 3.4) such that the lengths of the adatom bonds with the three first-layer atoms are equal to the bulk bond-length. The relative positions of atoms are initially chosen according to the (2×2) [or $c(4 \times 2)$] case of Table 3.4 [or Table 3.5]. The k-point sampling of this larger supercell is restricted to a single special point (mean-value point) of the hexagonal (2×2) ISBZ[42]. We then calculate Hellmann-Feynman forces, and let the atoms relax to the equilibrium positions. We also find that increasing the number of special k-points of the relaxed surface to three and six does not change the surface energy within 5 meV/(1×1)*cell*. As before we must also repeat the rigid ideal slab calculation using this larger supercell and k-point sampling. As shown in Table 3.7, the energy of the relaxed adatom-reconstructed surface turns out to be lower than all previous reconstructions by as much as 0.09 eV/(1×1)*cell*. This indicates that the adatom-restatom reconstruction is the most efficient way of saturating the highly unstable dangling bonds of the clean (111) surface of α-Sn. The alternative choice of a $c(4 \times 2)$ adatom-restatom geometry (using the two k-points obtained from the refolding in the $c(4 \times 2)$ ISBZ of the four ones used in the above (2×1) reconstruction calculations) confirms this result, yielding an energy 16 meV/(1×1)*cell* lower than the (2×2) choice. This energy difference is however comparable with our overall energy resolution. Similarly, our calculation does not rule out the existence of more complex surface reconstructions. It does however suggest that, if this is the case, then the adatom-rest atom mechanism is very likely to constitute the basic building block, as is the case in Si [48] and Ge [49]. Moreover, the advantage over the π-bonded chain reconstruction is larger in α-Sn, confirming

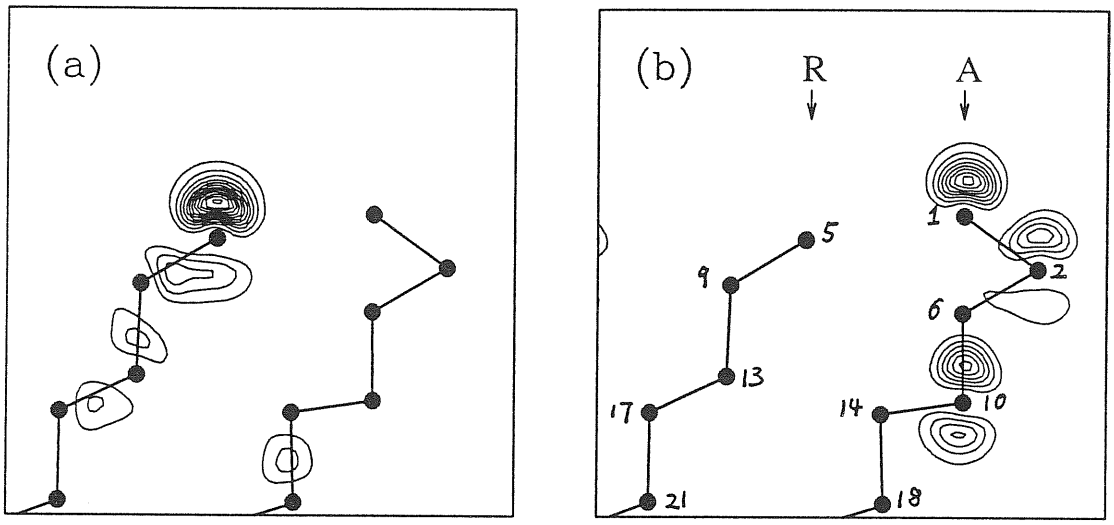

Figure 3.7: Electron density contours of the highest occupied state (panel (a)) and of the lowest unoccupied state (panel (b)) in the α-Sn(111) (2×2) adatom / restatom reconstruction at $\bar{K}$, on the same plane as in Fig. 3.6. In panel (b) atoms are labelled according to the optimal positions of Table 3.4. Contour lines are separated by 0.0004 (a.u.). Note the strong restatom / adatom characters, with a larger penetration of the adatom empty state.

the Si-Ge trend.

In Table 3.4 we report the relaxed atomic coordinates of the (2×2) adatom-restatom reconstructed surface. Due to the symmetry constraint, the adatom and restatom only relax in the z direction. The in-plane distance between the rest atom and its three neighbors has shrunk by about 10 % with respect to the ideal bulk value. The rest atom moves outward from its initial bulk-like position by 0.8 Å again a very large relaxation if compared with values in Si (0.3 Å), and in Ge (0.55 Å). Due to this relaxation, the rest atom forms bond angles of 94.0°, a value closer to total s, p dehybridization (90°) than to the original sp^3 one (109°), and bond lengths of 2.84 Å (bulk bond length is 2.79 Å). In turn, the adatom bond lengths with the

three neighboring first-layer atoms are 2.97 Å , larger by 7 % than the bulk bond length, and the adatom bond angles are 93.4°, quite similar to the rest atom. The second-layer atom beneath the adatom prevents further downward relaxation of the adatom, and is itself pushed downward. Although its final distance from the adatom (2.99 Å) is comparable with the other adatom bond lengths, there is no bond-like accumulation of electronic charge between them, as can be seen in the total charge density reported in Fig. 3.6. Rather, most of the adatom charge is transferred to the restatom dangling bond. This charge transfer is not directly visible in the total charge density of Fig. 3.6, but shows up clearly in the band structure of Fig. 3.8. The half filled surface-localized band typical of unsaturated dangling bonds (see Fig. 3.2), is here split into a lower filled band with prevailing rest-atom character, and an upper empty band mainly related to the adatom. This charge transfer is believed to constitute the fundamental mechanism for the stabilization of the adatom-rest atom reconstruction in Si and Ge [50, 51], and does appear to do so in Sn, as well. A glance at the charge density associated with the lower and upper surface bands (see Fig. 3.7) confirms this expectation. The charge associated with the lower band, shown in panel (a) of Fig. 3.7, has a strong rest-atom character and extends very little into the bulk, thus confirming its picture of saturated dangling bond. On the contrary, the upper unoccupied band (panel (b) of Fig. 3.7) has a strong adatom character, but extends largely below the adatom, and might therefore be thought to as a band of so called "floating bonds" [52] associated with both the adatom and the five-fold coordinated atom immediately underneath.

The optimal atomic positions and electronic band structure of the $c(4 \times 2)$

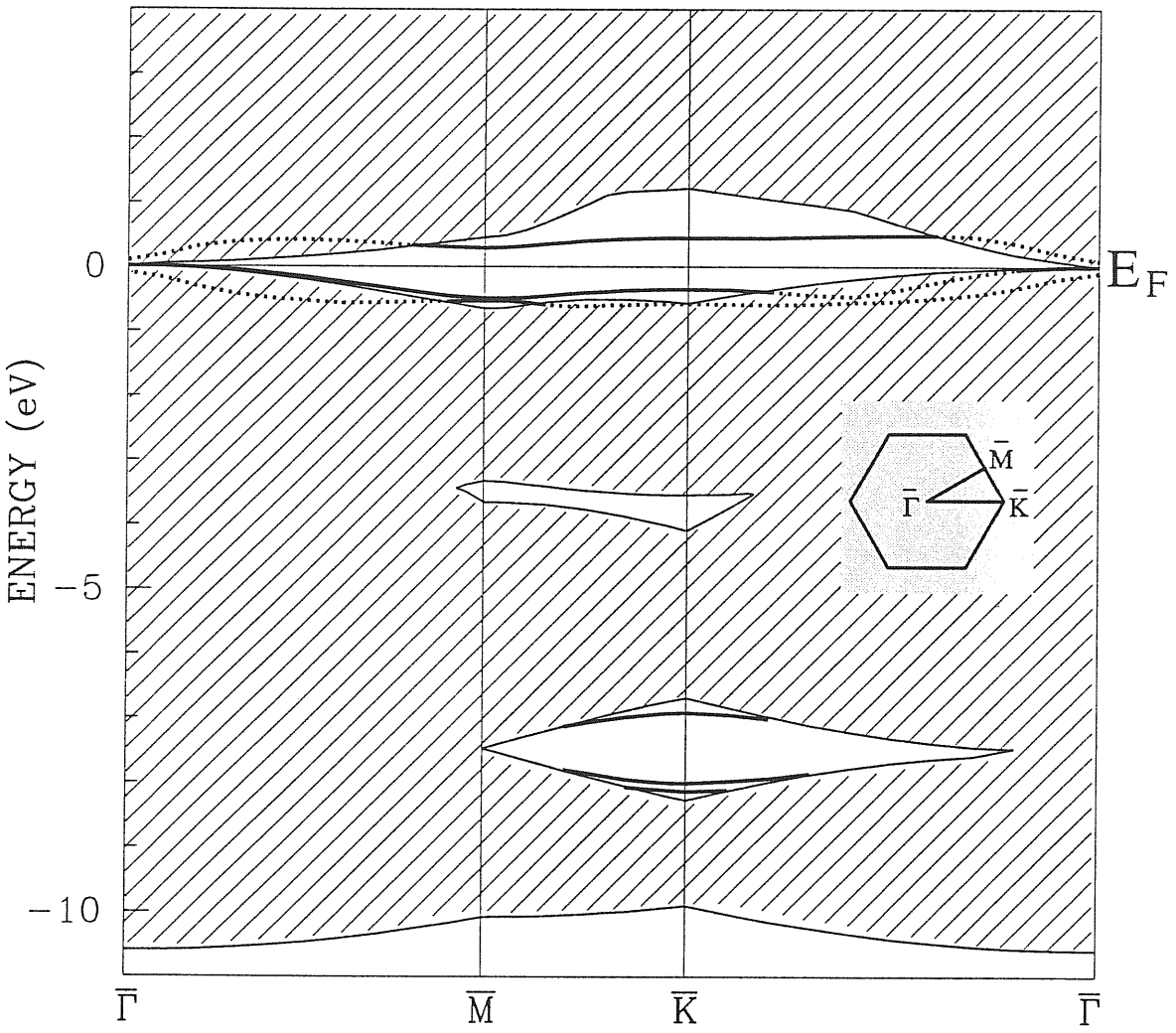

Figure 3.8: Surface electronic structure of the α-Sn(111)-(2×2) adatom-restatom reconstructed surface reported in the (2×2) hexagonal irreducible Brillouin zone (see inset). Shaded areas correspond to surface-projected bulk states, thicker lines correspond to surface states, dotted lines to surface resonances. The $\sim$ 1 eV splitting of the surface state reflects the adatom-restatom electron transfer.

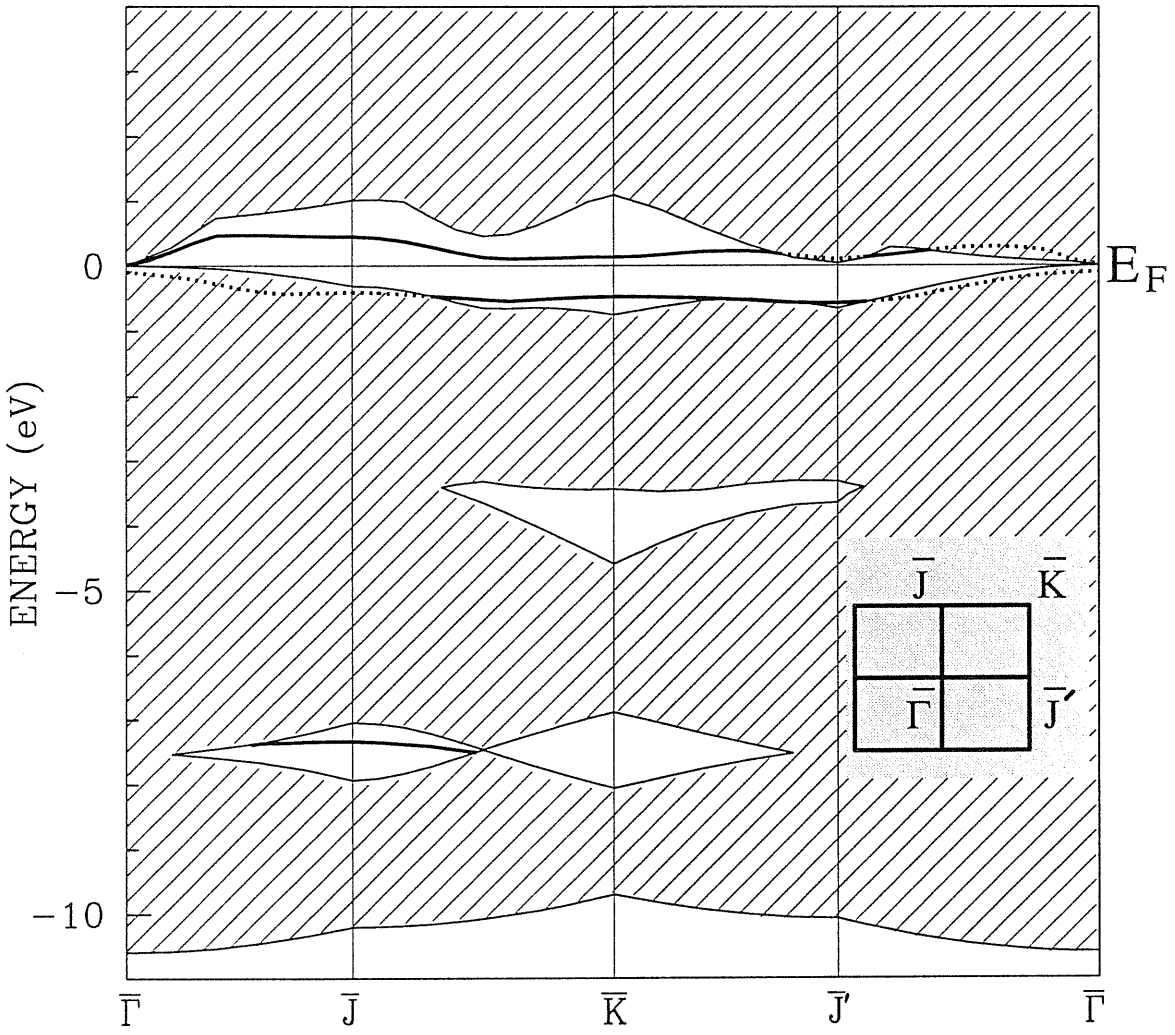

Figure 3.9: Surface electronic structure of the α-Sn(111)-$c(4 \times 2)$ adatom-restatom reconstructed surface reported in the $c(4 \times 2)$ rectangular irreducible Brillouin zone (see inset). Shaded areas correspond to surface-projected bulk states, thicker lines correspond to surface states, dotted lines to surface resonances.

adatom-restatom reconstruction are given in Table 3.5 and Fig. 3.9. Differences in the atomic relaxations and charge densities are negligible with respect to the (2×2) case, and will not be re-discussed.

We have verified that the H_3 site for the adatom is not energetically favored, the surface energy of this surface being higher than the one with adatoms in T_4 sites by about 70 meV/(1×1)*cell*. Its optimal atomic coordinates are given in Table 3.6.

We have also calculated the bridge site configuration for the adatom, where the adatom sits in the middle of the T_4 site and H_3 site. It turned out that an energy barrier of 0.70 eV is for the adatom diffusion between T_4 and H_3 sites on α-Sn(111), in analogy with Si(111) (a barrier of 1.1 eV[53]) and Ge(111) (a barrier of 0.8 eV[54]).

The adatom-restatom mechanism has just been shown to be the most efficient known mechanism to lower the surface energy of α-Sn(111) as of Si(111) and Ge(111). The true ground states of Si(111) and Ge(111) are respectively dimer-adatom-stacking-fault (DAS) (7×7) and $c(2\times8)$ adatom reconstructions, where the adatom-restatom structure is the basic unit. Thus, it is reasonable to expect that also the true ground state of α-Sn(111) will have the adatom-restatom structure as basic unit, as Si(111) and Ge(111).

Recent data on α-Sn surfaces have been obtained by epitaxial growth of α-Sn on other semiconductor surfaces. Recently a Japanese experimental group has grown α-Sn epitaxially on InSb(111) up to a thickness of about 30 monolayers (roughly 100 Å) at room temperature[7]. They found the Sb-free α-Sn(111) surface (more than four monolayers) to have a (3×3) reconstruction when grown at lower temperature, and "irreversibly" changing to a (2×2) structure upon annealing at high tempera-

tures. Finally the structure turns to 1×1 when the underlying Sb diffuses out. This experiment thus seems to suggest that the (2×2) reconstruction could be the ground state of α-Sn(111) surface, with the (3×3) reconstruction as a strong metastable state. Our calculations so far suggest therefore that the stable (2×2) structure obtained by high-temperature annealing could be the adatom-restatom reconstruction just described. We are presently planning further vibrational calculations in order to make more detailed predictions for future experiments.

3.5 (3×3) Reconstructions

In this section we analyze possible candidates for the (3×3) reconstructions observed in experiment[7]. Since we have no direct clues, a 3×3 DAS model is a natural candidate. On the other hand, the so-called α-phase of Pb/Ge(111) has recently been found to transform from a basic $\sqrt{3}\times\sqrt{3}$ adatom structure into a 3×3 Charge-Density-Wave (CDW)[55, 56] at low temperature. The basic electronic structure of a $\sqrt{3}\times\sqrt{3}$ Sn adatom overlayer on α-Sn(111) would be very similar. Hence, we restrict ourselves to consider the above two structures. The possible (3×3) reconstructions we consider are therefore the (3×3) DAS structure and a $\sqrt{3}\times\sqrt{3}$ overlayer enlarged to 3×3 (here called $\sqrt{3}^2$). There are several possibilities for "enlarging"the $\sqrt{3}\times\sqrt{3}$ structure, depending on the number of adatoms (one, two, or three, in the latter case combined with a CDW) present on the 3×3 cell. The configuration with three adatoms should be favored since the number of dangling bonds is the smallest.

Table 3.4: Initial, and optimized atomic positions of the α-Sn (111) (2×2) adatom / restatom (T_4 configuration) reconstructed surface. In the hexagonal supercell, coordinates are given by $\mathbf{r} = c_1\mathbf{a}_1 + c_2\mathbf{a}_2 + c_3\mathbf{a}_3$, where $\mathbf{a}_i$ is defined in the conventional cubic coordinate system as $\mathbf{a}_1 = (a_0/2)(-1,2,-1)$, $\mathbf{a}_2 = (a_0/2)(-1,0,1)$, $\mathbf{a}_3 = (a_0/3)(1,1,1)$ and a_0 (= 6.446 Å) is the lattice parameter.

	Atom	Initial			Optimal		
	no.	c_1	c_2	c_3	c_1	c_2	c_3
adatom	1	.000	.000	2.375	.000	.000	2.509
1st-layer							
	2	-.167	.500	2.125	-.158	.475	2.077
	3	.333	.000	2.125	.317	.000	2.077
	4	-.167	-.500	2.125	-.158	-.475	2.077
rest atom	5	.333	-1.000	2.125	.333	-1.000	2.343
2nd-layer							
	6	.000	.000	1.875	.000	.000	1.705
	7	.500	.500	1.875	.485	.544	1.935
	8	.000	-1.000	1.875	.030	-1.000	1.935
	9	.500	-.500	1.875	.485	-.544	1.935
3rd-layer							
	10	.000	.000	1.125	.000	.000	.963
	11	.500	.500	1.125	.500	.501	1.175
	12	.000	-1.000	1.125	.000	-1.000	1.175
	13	.500	-.500	1.125	.500	-.501	1.175
4th-layer							
	14	.167	.500	.875	.175	.525	.864
	15	.667	.000	.875	.667	.000	.926
	16	.167	-.500	.875	.175	-.525	.864
	17	.667	-1.000	.875	.650	-1.000	.864
5th-layer							
	18	.167	.500	.125	.170	.510	.110
	19	.667	.000	.125	.667	.000	.175
	20	.167	-.500	.125	.170	-.510	.110
	21	.667	-1.000	.125	.660	-1.000	.110

Table 3.5: Initial, and optimized atomic positions of the α-Sn (111) $c(4 \times 2)$ adatom / restatom (T_4 configuration) reconstructed surface. In the rectangular supercell, coordinates are given by $\mathbf{r} = c_1\mathbf{a}_1 + c_2\mathbf{a}_2 + c_3\mathbf{a}_3$, where $\mathbf{a}_i$ is defined in the conventional cubic coordinate system as $\mathbf{a}_1 = (a_0/2)(-1, 2, -1)$, $\mathbf{a}_2 = (a_0/2)(-1, 0, 1)$, $\mathbf{a}_3 = (a_0/3)(1, 1, 1)$ and a_0 (=6.446Å) is the lattice parameter.

Atom		Initial			Optimal		
no.	c_1	c_2	c_3	c_1	c_2	c_3	
adatom	1	.000	.000	2.375	.004	.000	2.527
1st-layer							
	2	.167	.500	2.125	.158	.469	2.083
	3	-.333	.000	2.125	-.313	.000	2.102
	4	.167	-.500	2.125	.158	-.469	2.083
rest atom	5	-.333	-1.000	2.125	-.341	-1.000	2.325
2nd-layer							
	6	.000	.000	1.875	-.006	.000	1.716
	7	-.500	.500	1.875	-.489	.525	1.941
	8	.000	-1.000	1.875	-.027	-1.000	1.945
	9	-.500	-.500	1.875	-.489	-.525	1.941
3rd-layer							
	10	.000	.000	1.125	.001	.000	.975
	11	-.500	.500	1.125	-.501	.501	1.178
	12	.000	-1.000	1.125	.005	-1.000	1.182
	13	-.500	-.500	1.125	-.501	-.501	1.178
4th-layer							
	14	-.167	.500	.875	-.174	.525	.880
	15	-.667	.000	.875	-.650	.000	.874
	16	-.167	-.500	.875	-.174	-.525	.880
	17	-.667	-1.000	.875	-.665	-1.000	.907
5th-layer							
	18	-.167	.500	.125	-.169	.509	.127
	19	-.667	.000	.125	-.661	.000	.123
	20	-.167	-.500	.125	-.169	-.509	.127
	21	-.667	-1.000	.125	-.668	-1.000	.149

Table 3.6: Initial, and optimized atomic positions of the α-Sn(111) (2 × 2) adatom / restatom (H_3 configuration) reconstructed surface. In the hexagonal supercell, coordinates are given by $\mathbf{r} = c_1\mathbf{a}_1 + c_2\mathbf{a}_2 + c_3\mathbf{a}_3$, where $\mathbf{a}_i$ is defined in the conventional cubic coordinate system as $\mathbf{a}_1 = (a_0/2)(-1,2,-1)$, $\mathbf{a}_2 = (a_0/2)(-1,0,1)$, $\mathbf{a}_3 = (a_0/3)(1,1,1)$ and a_0 (= 6.446 Å) is the lattice parameter.

	Atom	Initial			Optimal		
	no.	c_1	c_2	c_3	c_1	c_2	c_3
adatom	1	.167	.500	2.375	.167	.500	2.525
1st-layer							
	2	-.167	.500	2.125	-.142	.500	2.090
	3	.333	.000	2.125	.321	.037	2.090
rest atom	4	-.167	-.500	2.125	-.167	-.500	2.271
	5	.333	-1.000	2.125	.321	-1.037	2.090
2nd-layer							
	6	.000	.000	1.875	-.015	-.046	1.848
	7	.500	.500	1.875	.531	.500	1.848
	8	.000	-1.000	1.875	-.015	-.954	1.848
	9	.500	-.500	1.875	.500	-.500	1.984
3rd-layer							
	10	.000	.000	1.125	.000	-.001	1.102
	11	.500	.500	1.125	.501	.500	1.102
	12	.000	-1.000	1.125	.000	-.999	1.102
	13	.500	-.500	1.125	.500	-.500	1.199
4th-layer							
	14	.167	.500	.875	.167	.500	.861
	15	.667	.000	.875	.663	-.012	.883
	16	.167	-.500	.875	.175	-.500	.883
	17	.667	-1.000	.875	.663	-.988	.883
5th-layer							
	18	.167	.500	.125	.167	.500	.105
	19	.667	.000	.125	.665	-.006	.133
	20	.167	-.500	.125	.171	-.500	.133
	21	.667	-1.000	.125	.665	-.994	.133

3.5.1 DAS Reconstruction

We first consider the DAS (3 × 3) reconstruction. In the DAS structure the top three layers are reconstructed and have defects, while the layers below are complete. The arrangement of atoms in the DAS structure can be obtained by the stacking of triangular lattices in the order of either $\ldots AABBCCAAB + adatoms$ or $\ldots AABBCCAAC + adatoms$, where A, B, C denote the three inequivalent stacking arrangements along the [111] direction of bulk α-Sn. The adatom layer is formed by adatoms sitting in T_4 sites (2 × 2-like arrangement) on triangular sites of the first layer. Here, half the atoms occupy a site B (cubic diamond site) and the other half a site C (hexagonal diamond site). There is therefore a stacking fault below C but not below B, with an antiphase boundary between the two triangular B and C regions. The second layer is entirely A, but one atom is missing. Furthermore, the second-layer atoms at the antiphase border between the B and C regions are dimerized.

In detail, in the DAS (7 × 7) reconstruction of Si(111) surface each 7 × 7 unit cell consists of (i) twelve adatoms in the adatom layer, (ii) forty-two atoms in the first layer, six of which being restatoms, (iii)forty-eight atoms in the second layer with a single vacancy at the triangular apex, and nine dimers along the antiphase boundary. Thus there are nineteen dangling bonds in each unit cell. By contrast, a DAS (3 × 3) reconstruction consists of (i) two adatoms in the adatom layer, (ii) six atoms in the first layer, none of them being a rest atom, (iii) eight atoms in the third layer, one vacancy at the triangular vertex, and three dimers formed along the antiphase boundary. With this type of reconstruction, the dangling bonds are

reduced from nine to three in each 3×3 unit cell. The absence of restatoms represents a qualitative difference between the DAS (7 × 7) and (3 × 3).

As in the other surfaces also in this DAS-(3 × 3) reconstruction we have no data available to guide us to construct the details of this complicated reconstruction. We modeled the DAS (3 × 3) surface structure using a periodically repeated slab of twelve Sn monolayers (including one adatom layer on both sides) with inversion symmetry through the center of the slab, separated by a vacuum layer of 11 Å . We stack the three relevant layers containing two T_4 adatoms, one corner hole, and one half stacking fault. Starting the third layer and below we have the ideal α-Sn structure. We initially set the lengths of all bonds equal to that of the bulk bond (2.79 Å) without any dimerizations. The detailed initial atomic coordinates are given in Table 3.8, and Fig. 3.10 schematically shows what our initial atomic configuration looks like. Our slab is very large, containing eighty-six Sn atoms plus the vacuum region, we maintain the energy cutoff of 12 Ryd. We use one special k-point in the 3 × 3 ISBZ integration, which is equivalent to nine k-points in the (1 × 1) ISBZ. For the non-reconstructed reference surface we repeated the ideal α-Sn(111) surface calculation in the (1 × 1) unit cell, using the nine k-point set in the (1 × 1) ISBZ.

In our slab calculation for the DAS-(3 × 3) reconstruction, we have frozen the two innermost layers in the slab, and allowed all atoms in other layers to relax according to the calculated Hellmann-Feynman forces. The full relaxation was slow, and needed a very large amount of computation. The final surface energy of the optimized DAS (3 × 3) reconstruction on α-Sn(111) is 0.709 eV/(1 × 1 cell), sub-

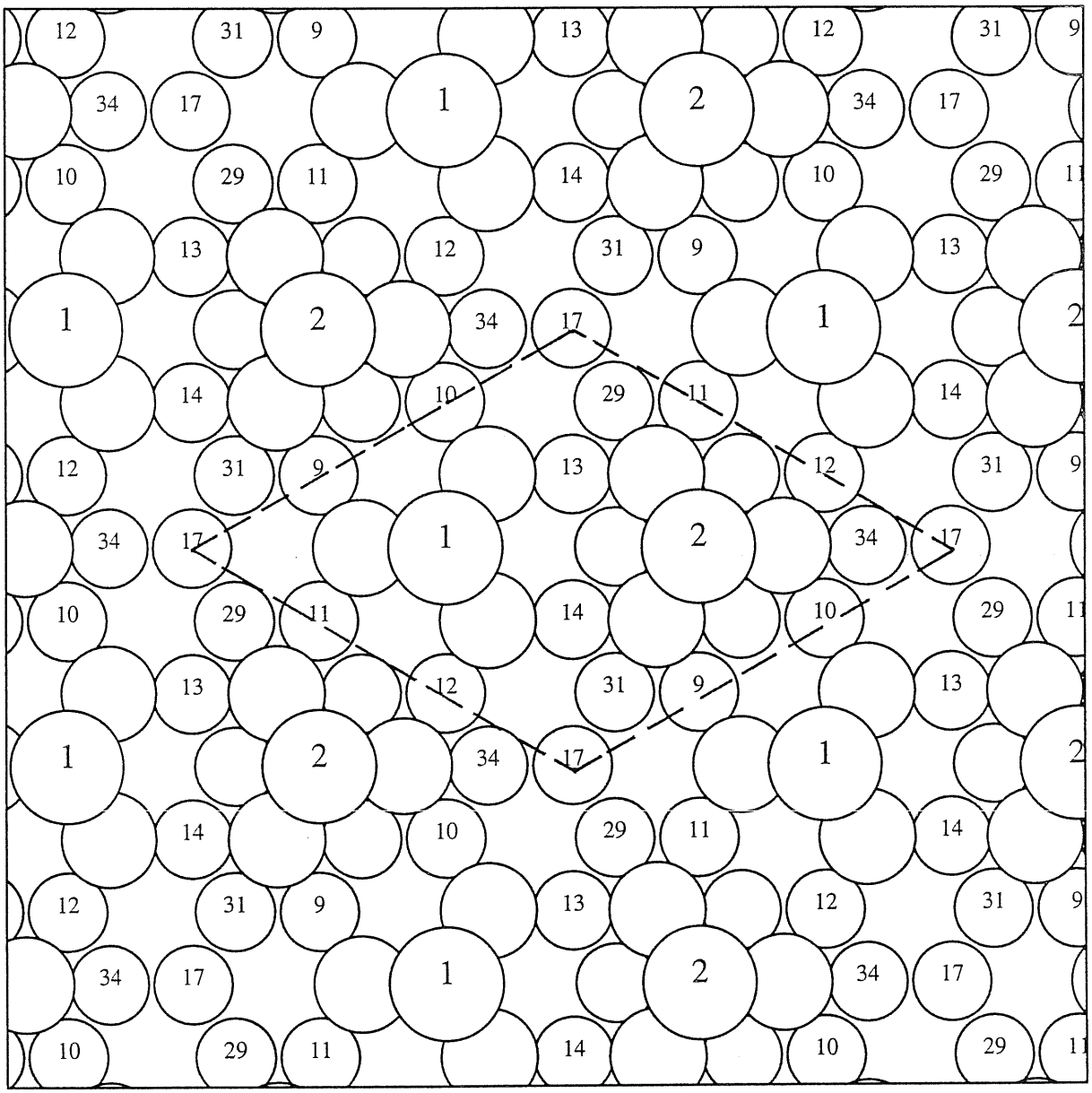

Figure 3.10: Top view of the initial atomic configuration for the DAS-(3 × 3) reconstruction on α-Sn(111). The numbers labeled on atoms correspond to those in Table 3.8. Please compare it with Fig. 3.11.

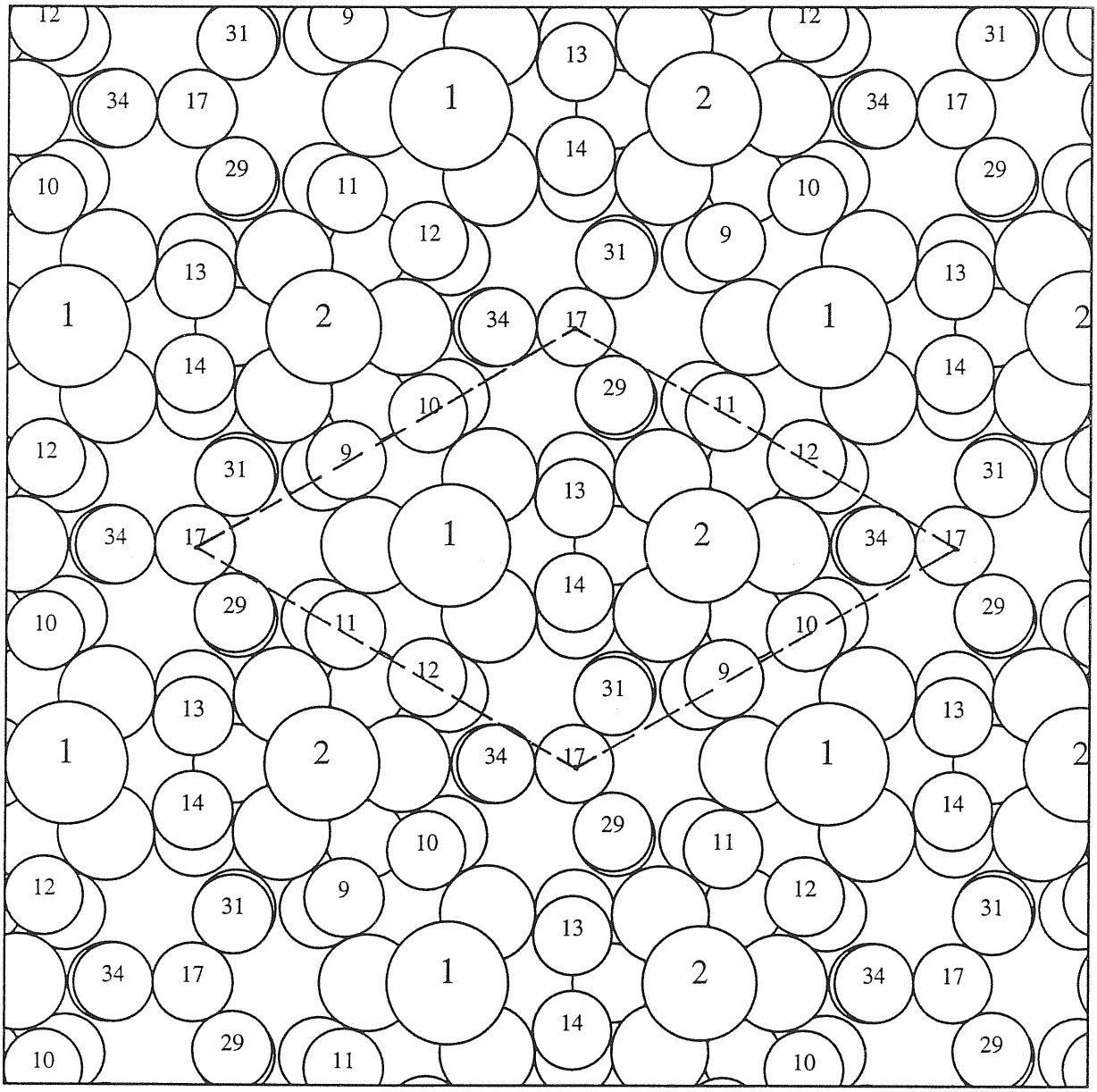

Figure 3.11: Top view of the final optimized atomic configuration for the DAS-(3×3) reconstruction on α-Sn(111). The numbers labeled on atoms correspond to those in Table 3.8. The atoms 9 and 10, 11 and 12, 13 and 14 are dimerized. The hole is located above atom 17. Four atoms 17 form the vertices of the unit cell.

stantially higher (about 90 meV/(1 × 1 cell)) than that of (2 × 2) adatom-restatom reconstruction(see Table 3.7). The relaxed atomic coordinates of the top six layers are reported in Table 3.8, and Fig. 3.11 schematically depicts the optimized DAS (3 × 3) reconstruction. We see that the atoms at the border between the two regions (type B and C) have indeed spontaneously dimerized. The three atoms in the first layer below the adatom move slightly closer to the adatom. The atoms beneath the adatoms are strongly pushed down, as in the (2 × 2) adatom-restatom reconstruction. The initial mirror symmetry between the two adatoms is lifted with a buckling of roughly 0.11 Å. After optimization, we also tested that increasing the number of k-points from one to six (equivalent to fifty-four k-points in the (1 × 1) ISBZ) does not modify the results.

3.5.2 The $\sqrt{3}^2$ Reconstruction

We now consider the $\sqrt{3}^2$ reconstruction. Unlike the DAS-(3×3) reconstruction, the $\sqrt{3}^2$ reconstruction is readily built. In one 3×3 unit cell, we can place one, or two, or three adatoms. Here we only consider the three adatoms case. Our calculation slab contains twelve layers (including two adatom-layers) with inversion symmetry across the slab center, as in the DAS-(3 × 3) case. The total number of atoms in the slab is ninety-six with 11 Å vacuum. The k-points sampling and energy-cutoff are the same as that of the DAS-(3×3) calculation. In order to remove the original $\sqrt{3} \times \sqrt{3}$ symmetry constraint, the starting atomic configuration was set by moving the three adatoms in slightly non-equivalent manner relative to each other. Then we relaxed the slab, following the calculated Hellmann-Feynman forces. The inequivalence of

the three adatoms is increased by relaxation. If, on the contrary, the three adatoms had become identical, an adatom $\sqrt{3} \times \sqrt{3}$ reconstruction (rest atom free) would be recovered.

After a long relaxation, the atomic configuration reached the equilibrium. The calculated surface energy turned out to be 0.694 eV/(1 × 1 cell), still quite higher (roughly 75 meV/(1×1 cell)) than that of the 2×2 adatom-restatom reconstruction, but somewhat lower (15 meV/(1×1 cell) than that of the DAS-(3×3) reconstruction. Looking at Table 3.7, we see that the $\sqrt{3}^2$ reconstruction is roughly degenerate with the 2×1 π-bonded chain reconstruction. The optimized atomic coordinates of the top six layers are reported in Table 3.9. The final inequivalence among the three adatoms consists in a height difference, or buckling, of 0.16 Å and 0.32 Å . Of the three adatoms *a*, *b* and *c*, *b* is 0.16 Å higher than *a*, and *c* 0.16 Å higher than *b*. The atoms in the first layer neighboring the adatoms are pushed slightly outwards, contrary to the 2×2 adatom-restatom reconstruction, whereas atoms in the second layer beneath the adatoms are pushed down as usual. On the whole, this reconstruction is so compact that the atoms have hardly any space to move.

This 3×3 structure can be seen as a Charge-Density-Wave (CDW) distortion over the bare $\sqrt{3} \times \sqrt{3}$ adatom structure, very much like in the low-temperature state of α-Pb/Ge(111)[57]. Since the driving force for the $\sqrt{3}\times\sqrt{3} \rightarrow 3\times3$ distortion is most likely the 2-dimensional (adatom dangling bond) Fermi surface, it is clear that a much more accurate k-point sampling than the one adopted here should have been required. After relaxation, we increased the number of k-points from one to six. It turned out that the surface energy changed less than 9 meV/(1×1cell).

3.5.3 Discussion

Our (3 × 3) adatom-only reconstruction models are energetically higher than the theoretical adatom-restatom ground state of the α-Sn(111) surface.

The adatom reconstruction that adsorbs the maximum number of dangling bonds on (111) surfaces is the $(\sqrt{3} \times \sqrt{3})$ adatom reconstruction without rest atoms, which reduces the dangling bonds from three to one in each unit cell, while in the (2 × 2) adatom-restatom reconstruction the dangling bonds are reduced from four to two in each unit cell. However, the 2 × 2 adatom-restatom reconstruction is lower in energy. The reason appears to be that for the 2 × 2 adatom-restatom reconstruction there is an energy gap in the surface state bands around the Fermi level due to the electron charge transfer from the adatom to the rest atom, causing the surface to become insulating. In particular, the charge transfer mechanism plays an even more important role for the reconstructions on α-Sn surfaces than on Si and Ge surfaces. For $\sqrt{3} \times \sqrt{3}$ adatom reconstruction, there is no restatom, and no charge transfer. Furthermore, there is always one dangling bond per unit cell, thus the surface is metallic. Similarly, no matter how we arrange or reconstruct the adatoms and atoms in (3 × 3) α-Sn(111) surface cell, there is always an odd number of dangling bonds left, and the surface is metallic, at least within a band picture. Moreover there are no restatoms in the DAS-(3 × 3) and in the $\sqrt{3}^2$ reconstructions. Of course, if we had only one or two adatoms instead of three in the 3 × 3 unit cell, then there would be rest atoms, but seemingly too many dangling bonds would remain.

In our calculations for the (3 × 3) reconstructions, we did not consider spin-polarization effects, which might possibly be important, since there are unpaired

electrons. However, it is unlikely that inclusion of spin-polarization could bring about the 80 meV/(1×1 cell) energy gain necessary to make the 3×3 reconstructions energetically lower than the 2 × 2 adatom-restatom reconstruction. Finally, there could still be other models for 3 × 3 structures which we failed to guess.

3.6 Metallic Overlayers

The presence of a metallic phase (β-Sn) energetically very close to the α phase, suggests the additional possibility that, at least in principle, an insulator-to-metal transition might take place at the surfaces of α-Sn, for example, through the formation of a thin β-Sn metallic overlayer. This was proposed to be the case, e.g., in gallium[9] where, based on calculations similar to those presented here, a metallic bilayer of Ga-III was predicted to stabilize the surface of α-Ga better than any other reconstruction. In our case, however, we encounter the problem, that no low-index β-Sn plane appears to match epitaxially, not even approximately, the α-Sn (111) lattice. Tentatively, we have calculated the surface energy of several structures obtained by covering the α-Sn(111) surface with strained epitaxial (100), (110), (111), and (221) planes of β-Sn. None of these surfaces gave a surface energy comparable, let alone lower, than the ideal (111) surface, all our results being higher with respect to the (2 × 2) adatom / restatom reconstruction by more than 0.45 eV/(1 × 1)$cell$. This negative result cannot of course be taken as a guarantee that metallic overlayers do not form at the α-Sn surface, since other more complex configurations, beyond our present fantasy, might have to be considered. The situation with respect to metallization remains therefore open.

An indirect indication against metallization is nonetheless provided by surface energies. One can expect metallization to be favored, in fact, in cases where the metal has a much lower surface free energy. In our case, however, the T=0 K calculated surface energy of reconstructed α-Sn (111), $E_{surf} \approx 540\ mJ/m^2$, is substantially lower than even the room temperature free energy measured for β-Sn[58], namely 670 mJ/m^2. This suggests that metallization has no reason to take place in the ground state. However, it could still be attained close to the α-Sn to β-Sn bulk transformation temperature.

Table 3.7: Calculated surface energies, absolute and relative, of different optimized reconstructions for α-Sn (111) surface.

Structure	E_{surf} [eV/(1×1 cell)]	E_{surf} $[mJ/m^2]$	ΔE [eV/(1×1 cell)]	vert. relax. or buckl.[a] (Å)
ideal	0.940	837	0.000	0
fully relaxed	0.933	831	-0.007	0.02
2 × 1 buckled	0.732	652	-0.217	1.23
(3 × 3)-DAS	0.709	631	-0.231	0.11[b]
2 × 1 π-bonded chain	0.697	621	-0.243	1.15
2×2-adatom (H_3)	0.696	620	-0.244	0.54 (restatom)
3 × 3-'CDW' ($\sqrt{3}^2$)	0.694	618	-0.246	0.16[c]
2×2-adatom (T_4)	0.626	558	-0.314	0.81 (restatom)
c(4×2)-adatom (T_4)	0.610	543	-0.330	0.74 (restatom)
metallized	$\geq$ 1.06	944	$\geq$ 0.121	

[a] Vertical relaxation is relative to initial bulk-like positions, and buckling is difference between relaxation of two atoms.

[b] The buckling between the two adatoms in one unit cell.

[c] In one chosen unit cell three adatoms a, b and c can be alternatively higher 0.16 Å, namely b 0.16 Å higher than a, then c 0.16 Å higher than b.

Table 3.8: Initial, and optimized atomic positions of the α-Sn (111) 3 × 3 dimer-adatom-stacking-fault (DAS) reconstructed surface. In the hexagonal supercell, coordinates are given by $\mathbf{r} = c_1\mathbf{a}_1 + c_2\mathbf{a}_2 + c_3\mathbf{a}_3$, where $\mathbf{a}_i$ is defined in the conventional cubic coordinate system as $\mathbf{a}_1 = (a_0/2)(-1, 2, -1)$, $\mathbf{a}_2 = (a_0/2)(-1, 0, 1)$, $\mathbf{a}_3 = (a_0/3)(1, 1, 1)$ and a_0 (= 6.446 Å) is the lattice parameter.The unit cell has three dimers A, B, and C.

	Atom	Initial			Optimal		
	no.	c_1	c_2	c_3	c_1	c_2	c_3
adatom	1	.500	1.500	2.375	.500	1.500	2.574
adatom	2	1.000	3.000	2.375	1.000	3.000	2.544
1st-layer							
	3	.333	1.000	2.125	.342	1.026	2.154
	4	.833	1.500	2.125	.816	1.500	2.154
	5	.333	2.000	2.125	.342	1.974	2.154
	6	1.167	2.500	2.125	1.156	2.531	2.115
	7	.667	3.000	2.125	.687	3.000	2.115
	8	1.167	3.500	2.125	1.156	3.469	2.115
2nd-layer							
dimer-A	9	.500	.500	1.875	.587	.593	1.879
dimer-A	10	1.000	1.000	1.875	.910	.916	1.879
dimer-B	11	.000	1.000	1.875	.003	1.177	1.879
dimer-B	12	.000	2.000	1.875	.003	1.823	1.879
dimer-C	13	1.000	2.000	1.875	.910	2.084	1.879
dimer-C	14	.500	2.500	1.875	.587	2.407	1.879
	15	.500	1.500	1.875	.500	1.500	1.765
	16	1.000	3.000	1.875	1.000	3.000	1.734

3rd-layer							
	17	.000	.000	1.125	.000	.000	1.287
	18	.500	.500	1.125	.500	.489	1.146
	19	.000	1.000	1.125	-.005	.995	1.146
	20	1.000	1.000	1.125	1.005	.995	1.146
	21	.500	1.500	1.125	.500	1.500	1.019
	22	.000	2.000	1.125	-.005	2.005	1.146
	23	1.000	2.000	1.125	1.005	2.005	1.146
	24	.500	2.500	1.125	.500	2.511	1.146
	25	1.000	3.000	1.125	1.000	3.000	.991
4th-layer							
	26	.333	1.000	.875	.327	.982	.877
	27	.833	1.500	.875	.845	1.500	.877
	28	.333	2.000	.875	.327	2.018	.877
	29	1.333	2.000	.875	1.344	1.967	.900
	30	.833	2.500	.875	.827	2.480	.865
	31	.333	3.000	.875	.311	3.000	.900
	32	1.333	3.000	.875	1.347	3.000	.865
	33	.833	3.500	.875	.827	3.520	.865
	34	1.333	4.000	.875	1.344	4.033	.900
5th-layer							
	35	.333	1.000	.125	.333	1.000	.125
	36	.833	1.500	.125	.833	1.500	.125
	37	.333	2.000	.125	.333	2.000	.125
	38	1.333	2.000	.125	1.333	2.000	.125
	39	.833	2.500	.125	.833	2.500	.125
	40	.333	3.000	.125	.333	3.000	.125
	41	1.333	3.000	.125	1.333	3.000	.125
	42	.833	3.500	.125	.833	3.500	.125
	43	1.333	4.000	.125	1.333	4.000	.125

Table 3.9: Initial, and optimized atomic positions of the α-Sn(111) 3×3 'CDW' ($\sqrt{3}^2$) reconstructed surface. In the hexagonal supercell, coordinates are given by $\mathbf{r} = c_1\mathbf{a}_1 + c_2\mathbf{a}_2 + c_3\mathbf{a}_3$, where $\mathbf{a}_i$ is defined in the conventional cubic coordinate system as $\mathbf{a}_1 = (a_0/2)(-1, 2, -1)$, $\mathbf{a}_2 = (a_0/2)(-1, 0, 1)$, $\mathbf{a}_3 = (a_0/3)(1, 1, 1)$ and a_0 (= 6.446 Å) is the lattice parameter.

	Atom	Initial			Optimal		
	no.	c_1	c_2	c_3	c_1	c_2	c_3
adatom	1	.000	.000	2.375	.000	.000	2.673
adatom	2	1.000	3.000	2.375	1.000	3.000	2.628
adatom	3	.500	1.500	2.375	.500	1.500	2.585
1st-layer							
	4	.167	.500	2.125	.148	.444	2.166
	5	.667	1.000	2.125	.654	1.039	2.127
	6	.167	1.500	2.125	.192	1.500	2.127
	7	1.167	1.500	2.125	1.204	1.500	2.166
	8	.667	2.000	2.125	.654	1.961	2.127
	9	.167	2.500	2.125	.148	2.556	2.166
	10	1.167	2.500	2.125	1.151	2.546	2.148
	11	.667	3.000	2.125	.697	3.000	2.148
	12	1.167	3.500	2.125	1.151	3.454	2.148
2nd-layer							
	13	.000	.000	1.875	.000	.000	1.749
	14	.500	.500	1.875	.495	.494	1.954
	15	.000	1.000	1.875	.000	.989	1.954
	16	1.000	1.000	1.875	1.005	1.005	1.954
	17	.500	1.500	1.875	.500	1.500	1.743
	18	.000	2.000	1.875	.000	2.011	1.954
	19	1.000	2.000	1.875	1.005	1.995	1.954
	20	.500	2.500	1.875	.495	2.506	1.954
	21	1.000	3.000	1.875	1.000	3.000	1.751

3rd-layer							
	22	.000	.000	1.125	.000	.000	1.015
	23	.500	.500	1.125	.500	.499	1.181
	24	.000	1.000	1.125	.000	.999	1.181
	25	1.000	1.000	1.125	1.001	1.000	1.181
	26	.500	1.500	1.125	.500	1.500	1.000
	27	.000	2.000	1.125	.000	2.001	1.181
	28	1.000	2.000	1.125	1.001	2.000	1.181
	29	.500	2.500	1.125	.500	2.501	1.181
	30	1.000	3.000	1.125	1.000	3.000	1.012
4th-layer							
	31	.333	1.000	.875	.327	.980	.882
	32	.833	1.500	.875	.847	1.500	.882
	33	.333	2.000	.875	.327	2.020	.882
	34	1.333	2.000	.875	1.328	2.016	.880
	35	.833	2.500	.875	.827	2.482	.883
	36	.333	3.000	.875	.344	3.000	.880
	37	1.333	3.000	.875	1.345	3.000	.883
	38	.833	3.500	.875	.827	3.518	.883
	39	1.333	4.000	.875	1.328	3.984	.880
5th-layer							
	40	.333	1.000	.125	.333	1.000	.125
	41	.833	1.500	.125	.833	1.500	.125
	42	.333	2.000	.125	.333	2.000	.125
	43	1.333	2.000	.125	1.333	2.000	.125
	44	.833	2.500	.125	.833	2.500	.125
	45	.333	3.000	.125	.333	3.000	.125
	46	1.333	3.000	.125	1.333	3.000	.125
	47	.833	3.500	.125	.833	3.500	.125
	48	1.333	4.000	.125	1.333	4.000	.125

4 The α-Sn (100) Surfaces

4.1 Introduction

Epitaxial growth of α-Sn on InSb has been reported very recently by several experimental groups [59, 6], with α-Sn film thicknesses as high as 2500 Å for α-Sn/InSb(100), and 100 Å for α-Sn/InSb(111). LEED and RHEED data show that α-Sn(100) displays a variety of reconstructions, in particular a two-domain (2×1), a p(2×2), and a c(4×4), which prevail successively for increasing film thicknesses on the InSb(100) substrate. The same, or very similar, reconstructions are also present in Si and Ge (100). In fact, it is now universally accepted that the reconstructions of these two surfaces fundamentally arise from the formation of surface dimers. In particular, asymmetric-dimers are considered as building blocks for the observed reconstructions such as 2×1, $c(4 \times 2)$, $p(2 \times 2)$ and so on. The similarity in the reconstruction periodicities observed on α-Sn(100) to those of Si(100) and Ge(100) suggests that dimer-based reconstructions should play a fundamental role also on α-Sn(100). However, no direct evidence for the existence of dimers has been produced so far for α-Sn(100), nor has any quantitative hint been provided of their geome-

try, of the magnitude of the buckling (if any), and of the electronic and vibrational properties which would substantiate the dimer hypothesis.

We have therefore carried out a first study of the atomic and electronic structure of α-Sn(100) in order to provide a sounder basis for further experimental investigations. Our conclusion is that dimers are indeed formed and stable on this surface. The main unexpected feature which we find is the giant magnitude of the asymmetric buckling, predicted to be as large as 1 Å , a factor of about 2.5 larger than that measured in Si(100) [11]. As a consequence, the electronic charge transfer within the dimer is also large. A well-defined dimer related surface resonance is also predicted in the surface vibrational spectrum. As for the true ground state periodicity, among the possible high order reconstructions $p(4 \times 1)$, $p(2 \times 2)$, $c(2 \times 2)$, $c(4 \times 2)$ and $c(4 \times 4)$, we find that the best are indeed $c(4 \times 2)$ and $p(2 \times 2)$ which are almost degenerate. Generally, the energy spread among these possibilities is anyway small.

As usual in supercell calculations, (unless otherwise specified in the following) we have modeled the surface using a periodically repeated slab of 12 Sn monolayers with inversion symmetry through the center of the slab, with a vacuum layer of 11 Å . The initial atomic positions are chosen according to the calculated equilibrium bulk lattice spacing ($a_o = 6.446$ Å). We freeze the two innermost middle layers, and allow all other layer atoms to relax according to the calculated Hellmann-Feynman forces. The relaxation lasts until the forces are less than 5meV/Å. From the construction of our slab, the surface energies E_{surf} are defined as usual

$$E_{surf} = (E_{slab} - NE_{bulk})/2 \quad , \tag{4.1}$$

where E_{slab} is the total energy of the slab, E_{bulk} is the energy per atom of bulk α-Sn

as computed in section II of Chapter II [E_{bulk}=-96.753 eV/atom], and N is the total number of atoms in the slab. The factor 1/2 accounts for two identical surfaces as required by the inversion symmetry in our slab. For (1×1), (2×1), $p(4 \times 1)$, $p(2 \times 2)$, $c(2 \times 2)$, $c(4 \times 2)$ and $c(4 \times 4)$ surfaces, we used slabs with 1 atom per layer, 2 atoms per layer, 4 atoms per layer, 4 atoms per layer, 2 atoms per layer, 4 atoms per layer, and 8 atoms per layer, respectively.

K-point sampling: A set of four special k-points is chosen to sample the (2×1) rectangular ISBZ [42] for the (2×1) symmetric dimer structure, which is equivalent to a set of eight k-points in the (1×1) square ISBZ. For our surface calculations of the 2×1 asymmetric dimer structure, $p(4 \times 1)$, $p(2 \times 2)$, $c(2 \times 2)$ and $c(4 \times 4)$ reconstructions, we take the k-point set equivalent to the set of four special k-points in the 2×1 ISBZ, respectively. For instance, in the 2×1 asymmetric dimer case, the equivalent k-point set is eight k-points due to lower symmetry operation in the 2×1 Surface Brillouin Zone. In order to check the effect of the k-point sampling in our surface calculations, we increased the k-point set to one equivalent to a set of sixteen special k-points in the 2×1 ISBZ for every one of the mentioned structures. No meaningful changes took place. On the other hand, among all considered structures there is one exception, namely, the $c(4 \times 2)$ reconstruction. It is impossible to find a k-point set in the $c(4 \times 2)$ oblique ISBZ which is exactly equivalent to the set of four k-points in the 2×1 rectangular ISBZ. In this case, we sampled four special k-points in the $c(4 \times 2)$ oblique ISBZ. We had also to repeat the ideal Sn(100) surface calculation using a $c(4 \times 2)$-geometry-like slab, which was considered as a reference state. We then performed the $c(4 \times 2)$ reconstruction calculation. After

relaxation, we also checked that increasing the k-point number from four to sixteen in $c(4\times2)$ oblique ISBZ changed little of the calculated results. We are thereby able to compare the different reconstructed surface energies with each other.

4.2 The Unreconstructed α-Sn (100) Surface

We started by considering the ideal α-Sn (100) surface since the details of its atomic and electronic structure will show the basic driving forces towards more stable reconstructions, and as a reference state for all reconstructions. The calculated α-Sn ideal (100) surface energy turns out to be 1.405 eV/(1×1 cell) (Table 4.3). The corresponding ideal surface electronic band structure is reported in Fig.4.1.

It is seen that several surface bands cross the gap regions of the projected bulk energy bands. In particular, since on the ideal α-Sn (100) surface, each surface atom has two dangling bonds, the latter give rise to two surface state bands in the fundamental gap region. The splitting between these two surface state bands indicates that a non-negligible interaction exists between the two dangling bonds, which lifts their original degeneracy. This is also reflected by electron charge density in Fig.4.3 left and right panels, which respectively corresponds to surface states S_1 and S_2 at $\bar{K}$ in the ISBZ. Since the original sp^3 orbitals of the surface atom are partially dehybridized back to their $s-$ and $p-$components, the surface states in fundamental gap are correspondingly split into prevalently s-like states (so-called dangling bond states, see Fig. 4.3 left panel) and prevalently p-like states, and the two p-type orbitals of neighbor surface atoms slightly overlap (so-called bridge bond states, see Fig.4.3 right panel). The total charge distribution (Fig.4.2) however,

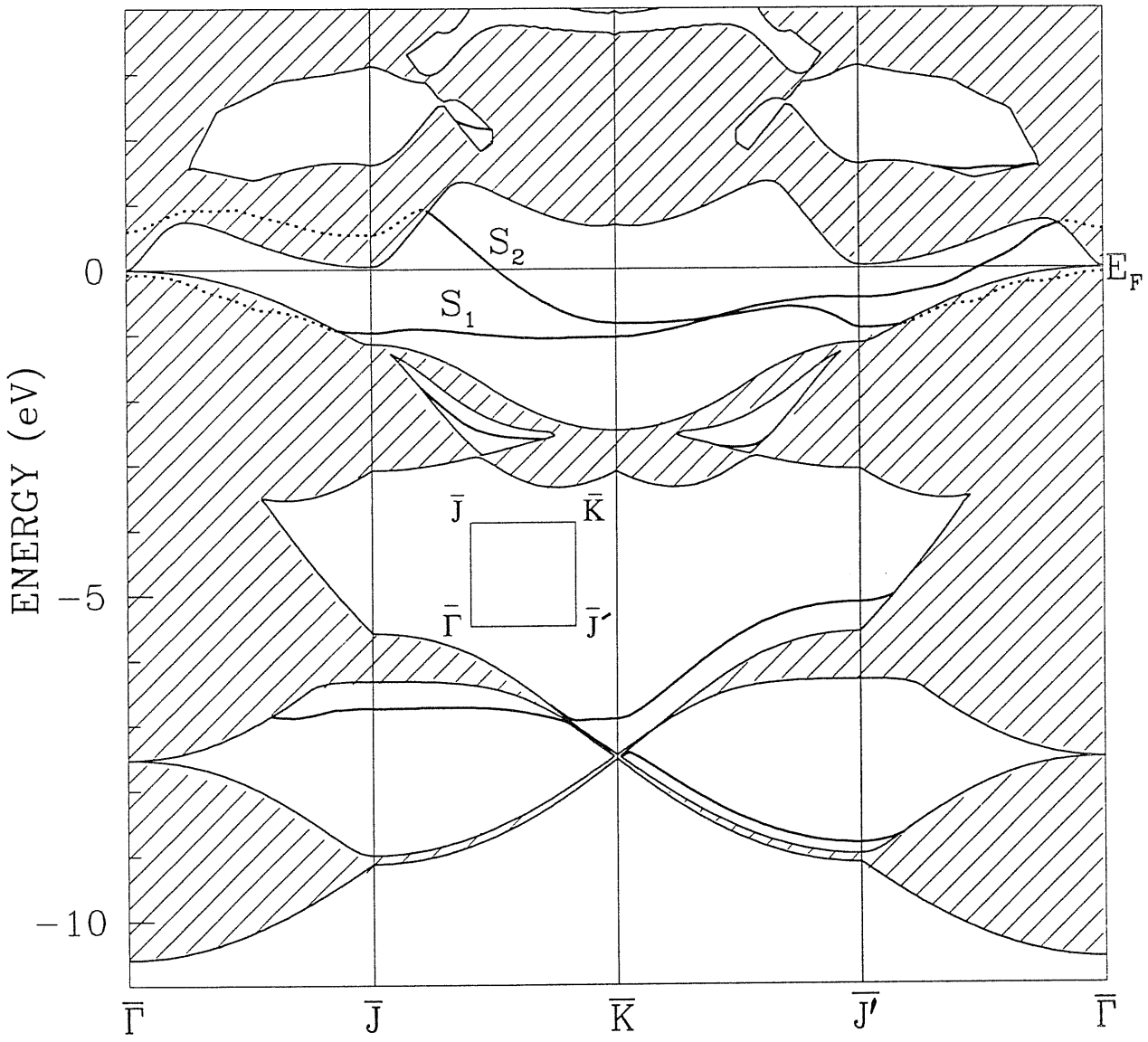

Figure 4.1: Surface electronic band structure of the ideal α-Sn(100) surface reported along high-symmetry lines of the (1 × 1) square irreducible Brillouin zone. The Fermi level is set to zero. Shaded areas correspond to surface-projected bulk states, while thicker lines correspond to surface states, dotted lines to surface resonances. The irreducible surface Brillouin zone is given in the inset. Note the quite large dispersion of surface bands S_1 and S_2. The surface bands S_1 and S_2 do not cross.

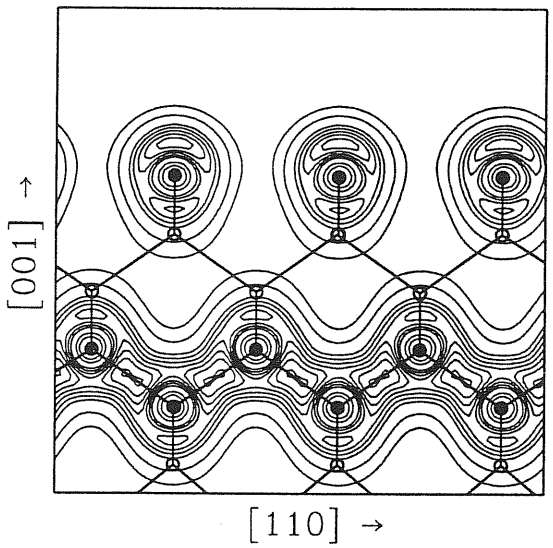

Figure 4.2: Geometry, and total electron density contour of the ideal (1 × 1) surface, on the (110) plane passing through the Sn atoms represented by full circles, empty circles indicate the out-plane Sn atoms, and thicker straight lines indicate bonds between Sn atoms. Contour lines are separated by 0.005 (a.u.). Note the electrons localized on top atoms, and no bonds formed between the top atoms.

shows that in the ideal surface there is no bond among neighboring surface atoms, and the electrons are highly localized around them. The protrusive character of such electronic states suggests that the work function of the ideal α-Sn(100) surface should be rather high. We computed the planar and macroscopic averages of the Hartree potential, reported in Fig.4.5(a), and obtained a value for the work function of 4.68 eV (Table 4.1). We also calculated the important LDOS, which is reported in Fig.4.4. The two surface bands (shown as shaded regions in Fig. 4.4 (a)), are clearly seen to be located at the two sides of the Fermi level, and they are clearly related to the surface layer and to the second layer only. Therefore, even though

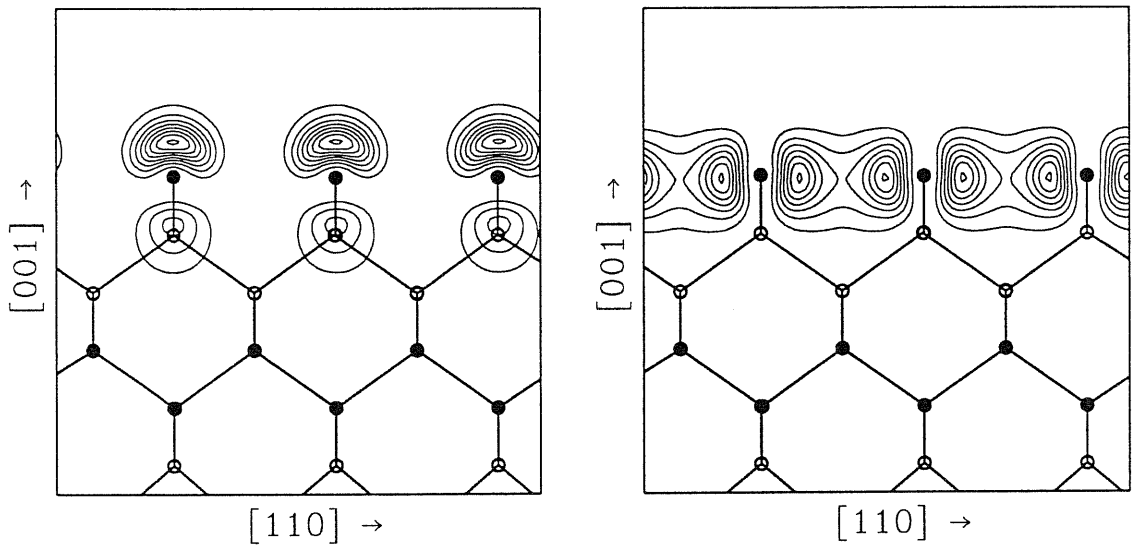

Figure 4.3: Electron density contours of the surface S_1 eigenstate (left panel, dangling bond state D) and surface S_2 eigenstate (right panel, bridge bond state Br) of the ideal (1×1) surface at $\bar{K}$, on the (110) plane passing through the Sn atoms represented by full circles, empty circles indicate the out-plane Sn atoms, and thicker straight lines indicate bonds between Sn atoms. Contour lines are separated by 0.002 (a.u.). Note in the left panel a much high degree of electron charge localization on top atoms, and in the right panel a very weak correlation exists between two neighbor top atoms.

the Fermi level crosses the surface bands in the fundamental gap (see Fig.4.1), the ideal α-Sn (100) surface displays an almost negligible density of states at the Fermi level, like the ideal Si(100)[60] surface, due to the large dispersion of the surface bands in the fundamental gap. Nevertheless, the very high value of the surface energy, as well as the presence of surface states with a high degree of electron charge localization, all suggest that this ideal surface should be unstable towards relaxation and/or reconstruction, as on Si and Ge(100).

The atomic positions in the slab were therefore allowed to relax according to

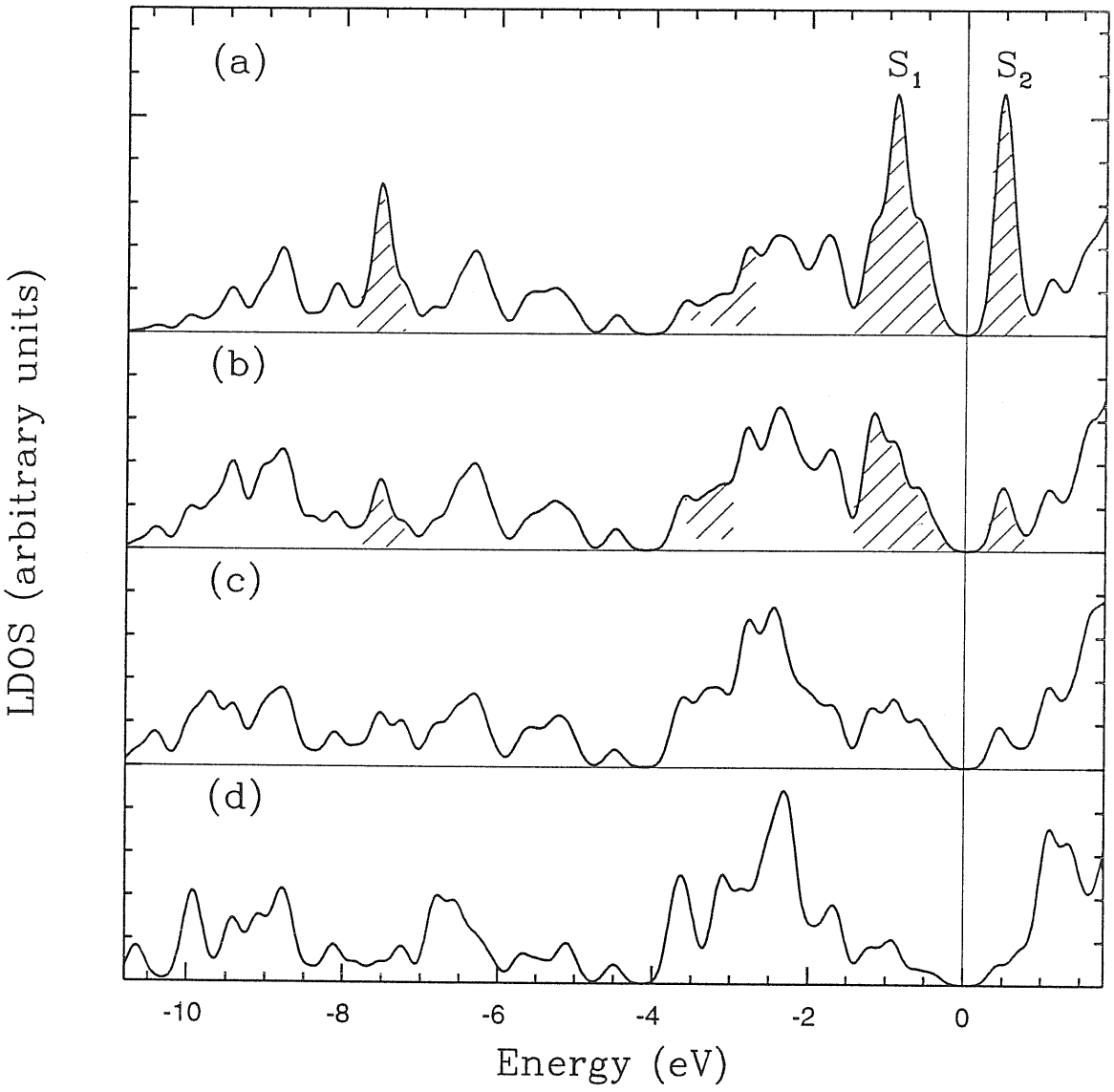

Figure 4.4: Layer-projected density of states (LDOS) for the 1×1 ideal α-Sn (100) surface (12-layers slab calculation). The Fermi level is set to zero. In panel (a), (b), (c) and (d) the solid curves are, respectively, the density of states (DOS) projected on the surface layer, the second layer, the third layer and the center layer (sixth layer) whereas the DOS projected on the center layer produced a good bulk DOS. The LDOS of panel (c) very similar to that of panel (d) indicates that the surface states are primarily related to the surface layer and second layer structure. Shaded areas indicate the surface states. Note the zero-gap semiconducting feature of LDOS in panel (a).

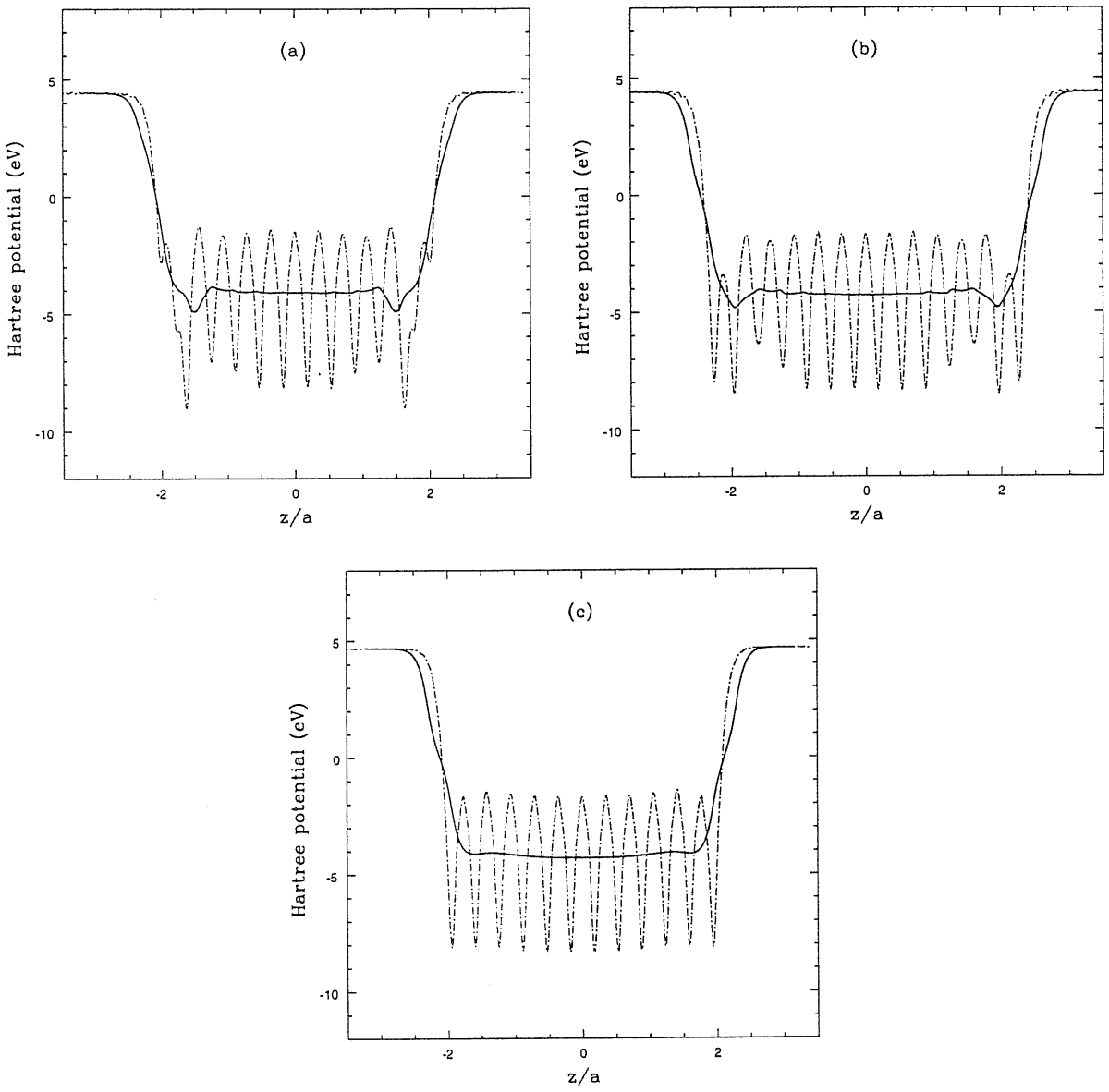

Figure 4.5: Planar averaged Hartree potential along the [001] direction (dash-dotted line), and its macroscopic average $\bar{V}_H$ defined in eq.(2.11) (solid line). The Fermi level is set to zero. The distance along the [001] direction is in units of $a = 8.613(a.u.)$. Panels (a), (b) and (c) are, respectively, for 2×1 asymmetric dimer reconstructed α-Sn surface, 2×1 symmetric dimer reconstructed α-Sn surface, and 1×1 ideal α-Sn surface. Note in each panel the minimum value points of dash-dotted line correspond to the layer atom positions along [001] direction.

Table 4.1: Calculated work functions Φ, respectively, for the 2×1 asymmetric dimer reconstructed, the 2×1 symmetric dimer reconstructed and the ideal unreconstructed α-Sn (100) surfaces

Structure	Asymmetric dimer	Symmetric dimer	Ideal
Φ (eV)	4.43	4.42	4.68

the calculated Hellmann-Feyman forces. We first relaxed the positions preserving the (1×1) surface periodicity. This leads to a gain in surface energy of only 23 meV/(1×1 cell) and a vertical inward relaxation of only 0.071 Å in the surface atoms, indicating that only proper reconstructions with higher periodicity are likely to lower the energy.

In the following sections we consider the possible reconstructions of α-Sn(100) with larger surface unit cells.

4.3 The 2×1 Dimer Reconstructions

4.3.1 The Symmetric Case

We first ignored the subtleties related to higher periodicities and focused on the understanding of the basic building block of all (100) reconstructions, namely the formation of surface dimers. Accordingly we first restrict our analysis to a (2×1) surface unit cell. We constructed a trial symmetric dimer structure in which the two surface atoms are dimerized, and all bond lengths, including the dimerized bond, are initially set equal to the bulk bond length. We also would like to require the mirror symmetry along [110] to be preserved in our slab. However, it is impossible

to have a mirror symmetry in a slab of twelve layers with inversion symmetry, while this can be done with ten or fourteen layers. In the present calculation, we chose a slab of fourteen layers with inversion symmetry, plus the required mirror symmetry along [110]. In this case we froze the four innermost layers, and relaxed all other layers.

Full relaxation of the atomic positions in the (2×1) *symmetric* dimer reconstruction leads, as expected, to a dramatic lowering of surface energy to 0.906 eV/(1×1 cell), 0.499 eV/(1×1 cell) lower than the ideal surface(see Table 4.3). This lowering is related to the formation of the Sn-Sn surface dimers which reduce the number of the dangling bonds to one per atom. It can also be traced back to the opening of a gap between the bonding and antibonding states of the dimer, indicated by the surface bands S_4 and S_5 in the surface band structure calculated at the converged 2×1 geometry (Fig. 4.6). The total electron charge density in Fig. 4.7 confirms that a strong bond forms in the surface dimer. The LDOS (Fig. 4.9) however shows that the surface is still metallic, as the symmetric dimer Si(100) and Ge(100) surfaces[10, 14, 15, 61], due to the presence of two half-filled bands of almost degenerate surface states related to the left dangling bonds of the outermost surface atoms (now each surface atom has only one dangling bond left). This is clearly reflected by the charge density distributions of the surface states S_1 and S_2 at $\bar{K}$ reported in Fig. 4.8 upper and lower panels, respectively. The mirror symmetry between the two remaining dangling bonds in the dimer is clearly seen. Besides the surface bands S_1 and S_2, there are other surface bands S_3, S_4 and S_5 in fundamental gap region, which will similarly appear in the following asymmetric dimer case and will

be discussed there. The final relaxed atomic coordinates for the symmetric dimer calculation are given in Table 4.4. The dimer bond length is 2.90 Å (bulk bond length is 2.79 Å). Looking at the charge density maps of Fig. 4.3 and Fig. 4.8, we note that the electrons are more delocalized around the top surface atoms than on the ideal α-Sn(100) surface. We thus expected that in this case the surface work function should be lower than that of the ideal α-Sn(100) surface. We have computed the planar and macroscopic averages of the Hartree potential, and reported them in Fig. 4.5(b). The surface work function turns out to be 4.42 eV, in the symmetric dimer case indeed smaller than that of the ideal α-Sn(100) surface (see Table 4.1).

Finally, the presence of half-filled dangling bonds and of metallic surface bands in the fundamental gap suggests that the symmetric dimer reconstruction should still be unstable towards any distortion that may lift the residual near-degeneracy of the surface states S_1 and S_2.

4.3.2 The Asymmetric Case

We now allow the two surface atoms to be slightly non-equivalent, thereby breaking the [110] mirror symmetry. We then calculate the Hellmann-Feyman forces to guide the relaxation of atomic structure. Even though the inequivalence of the surface atoms is initially minute, it grows to a considerable buckling immediately after relaxation.

The surface energy is much lowered by allowing the dimers to become asymmetric. Full relaxation of the atomic positions in the (2×1) *asymmetric* dimer

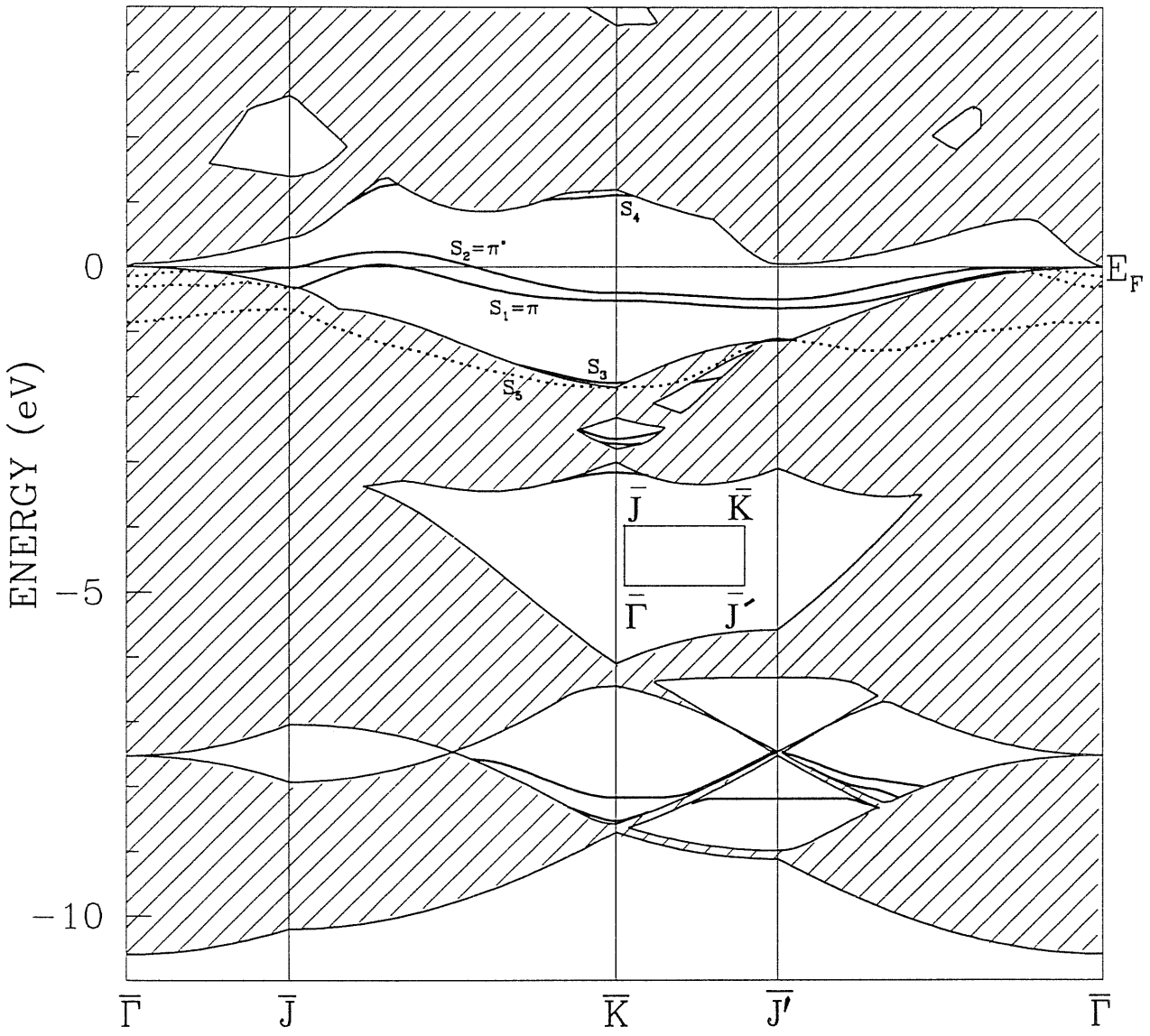

Figure 4.6: Surface electronic band structure of the (2×1) symmetric dimer reconstructed surface reported along high-symmetry lines of the (2×1) rectangular irreducible Brillouin zone. The Fermi level is set to zero. Shaded areas correspond to surface-projected bulk states, while thicker lines correspond to surface states. The irreducible surface Brillouin zone is given in the inset. Note the quasi-degenerate surface bands S_1 and S_2 primarily distributed nearby the Fermi level, and its metallic feature.

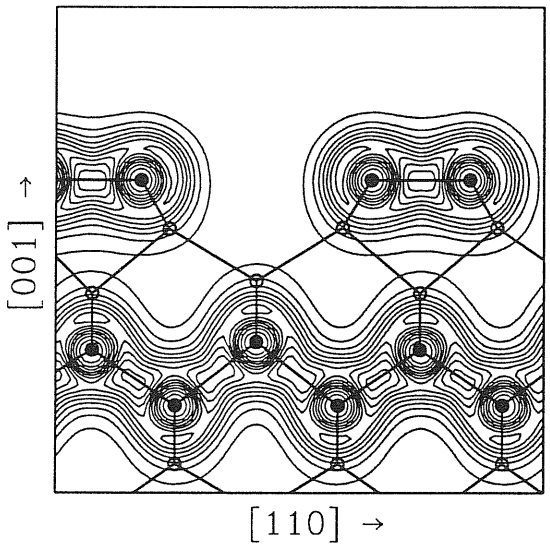

Figure 4.7: Geometry, and total electron density contour of the (2 × 1) symmetric dimer reconstructed surface, on the (110) plane passing through the Sn atoms represented by full circles, empty circles indicate the out-plane Sn atoms, and thicker straight lines indicate bonds between Sn atoms. Contour lines are separated by 0.005 (a.u.). Note a strong covalent bond formed in the dimer.

reconstruction leads in fact to a final surface energy of 0.787 eV/(1×1 cell), 0.119 eV/(1×1 cell) lower that the symmetric case. The atomic coordinates of the fully relaxed asymmetric dimer reconstruction are reported in Table 4.5. This very large energy gain is accompanied by a giant buckling of the dimer ($b = 1.01$ Å, $\omega = 21.01°$, see inset of Fig. 4.12).

The surface electronic band structure of the asymmetric dimer structure is reported in Fig. 4.10. As expected, the large buckling of the surface dimer leads to the opening of a large surface energy gap between surface bands S_1 and S_2, compared with the symmetric dimer case (see Fig.4.10 and 4.6). The Fermi level lies in this gap, and the asymmetric dimer reconstruction is insulating. The buckling of the surface dimer causes the sp^3 covalent orbitals of the surface atoms to partially

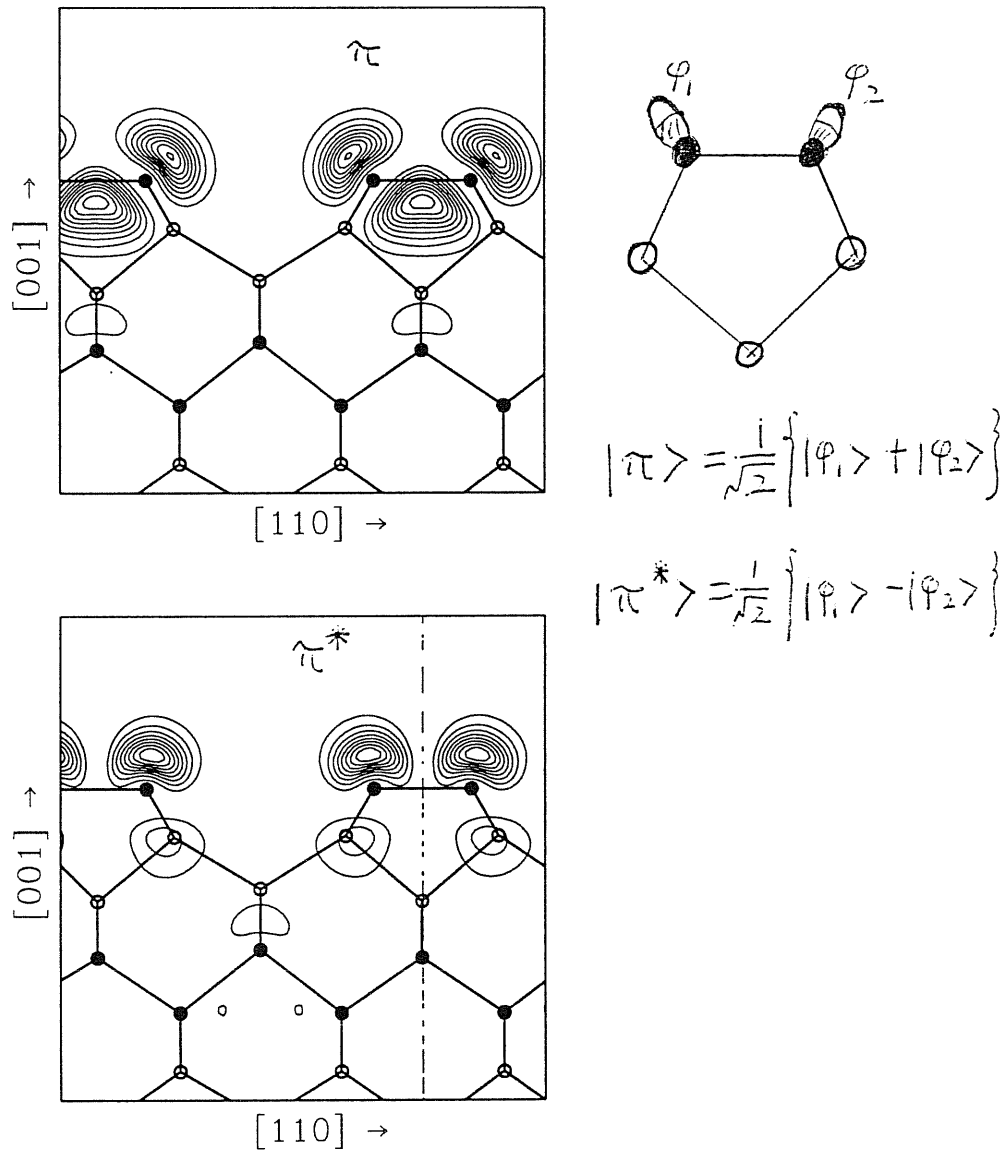

Figure 4.8: Electron density contours of the surface S_1 eigenstate (the upper panel, π state) and of the surface S_2 eigenstate (the lower panel, π^* state) in the (2×1) symmetric dimer reconstruction at $\bar{K}$, on the (110) plane passing through the Sn atoms represented by full circles, empty circles indicate the out-plane Sn atoms, and thicker straight lines to bonds among Sn atoms. Contour lines are separated by 0.0005 (a.u.). Note the mirror symmetry between the two dimer atoms.

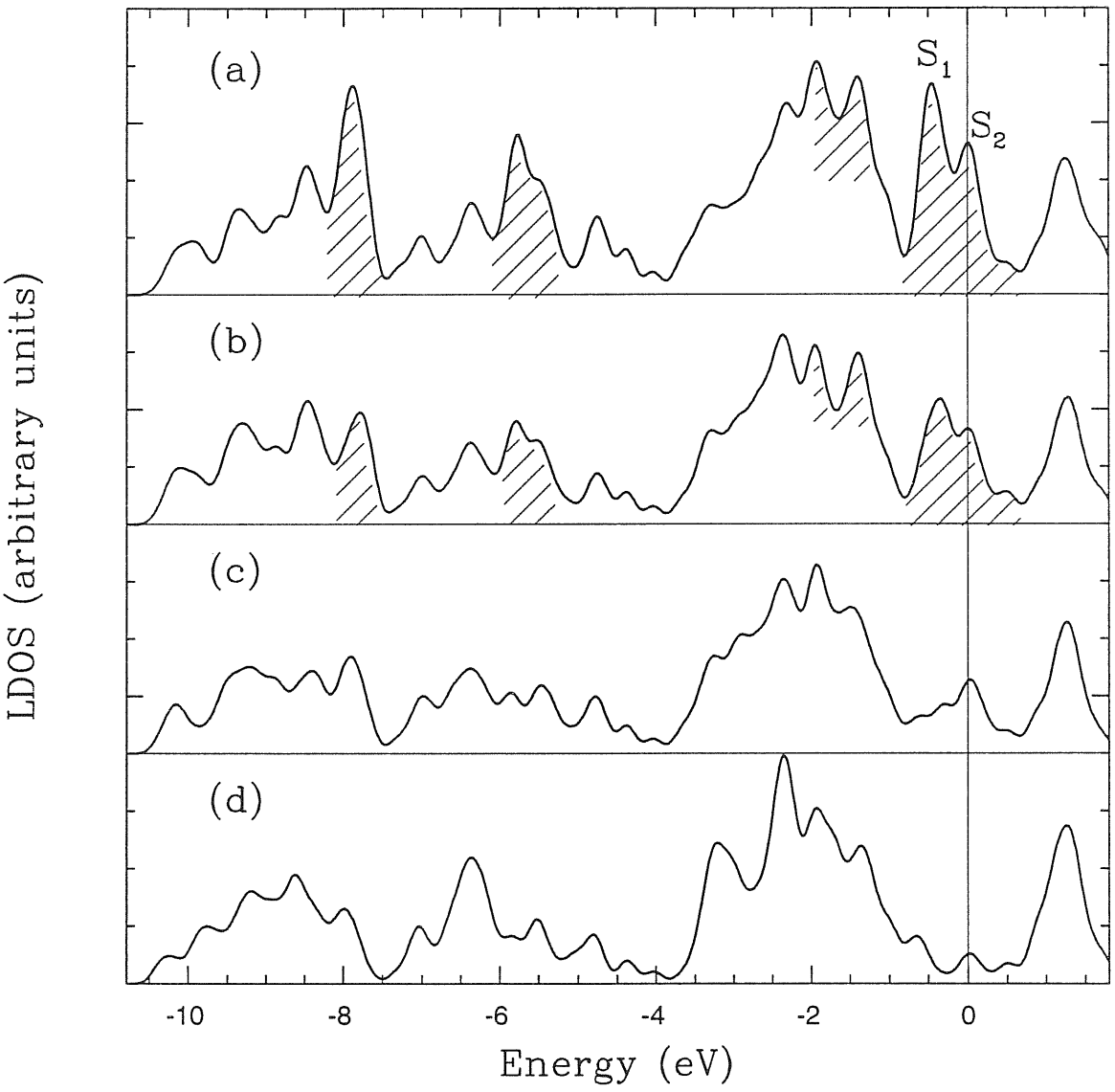

Figure 4.9: Layer-projected density of states (LDOS) for the 2 × 1 symmetric dimer reconstructed α-Sn (100) surface (14-layers slab calculation). The Fermi level is set to zero. In panel (a), (b), (c) and (d) the solid curves are, respectively, the density of states (DOS) projected on the surface layer, the second layer, the third layer and the center layer (seventh layer) whereas the DOS projected on the center layer produced a good bulk DOS. The LDOS of panel (c) very similar to that of panel (d) indicates that the surface states are primarily related to the surface layer and second layer reconstructure. Shaded areas indicate the surface states. Note the "good" metallic feature of LDOS in panel (a).

dehybridize. The dangling bonds on the outward and inward surface atoms are becoming prevalently s-like and p-like, respectively. According to the usual mechanism, an electronic charge transfer from the inward atom to the outward atom takes place. The completely filled surface states labeled with S_1 in the surface band structure of Fig. 4.10 are mainly localized on the outward surface atom with mostly s-like character (Fig.4.13 upper panel), and the empty surface states labelled with S_2 are mainly localized on the inward surface atom with mostly p-like character (Fig. 4.13 lower panel). These behaviors are very similar to those of Si(100) and Ge(100) surfaces[62]. We can now analyze the other surface bands S_3, S_4 and S_5 present in the fundamental gap region. The electron charge density distributions of Fig. 4.14 upper panels show that the filled surface states S_3 and the empty surface states S_4 are 'back bond' surface states related to the second surface layer atoms. The surface band S_5 is closely related to the bond formed in the asymmetric buckled dimer (Fig. 4.14 lower panel). The total charge density distribution, reported in Fig. 4.12, shows the total charge accumulation in the bonding region of the asymmetric dimer.

The calculated LDOS for the asymmetric dimer surface is reported in Fig. 4.11. If we compare it with Fig. 4.9, we see that the surface states around the Fermi level in Fig. 4.9 are here split into two components, and are pushed at the two sides of the Fermi level in Fig. 4.11. Both the LDOS and the surface band structure of Fig. 4.10 show that a gap of about 1.2 eV separates the two surface bands. It is therefore predicted that a surface optical obsorption peak should be observed with surface-sensitive techniques such as infrared reflectivity, electron-energy loss spectroscopy

(EELS), or photoemission, due to excitations across this gap.

The electron transfer connected with the formation of such a highly distorted surface dimer is relatively large, and should give rise to an observable shift in the core level position of the dimer atoms. A calculation of this shift is planned for the near future.

Moreover, the electron transfer connected with the dimer buckling will be strongly modulated by that particular surface vibration, or "rocking mode" [63], which modulates the buckling. We have extracted an approximation to the eigenvector of this mode by examining the coordinate evolution in the last few steepest descent iterations during relaxation, from zero buckling to the final large buckling geometry. Using this approximate eigenvector we have calculated the frozen-phonon frequency (ν_r) of the "rocking mode" at $k = 0$, and found a value of $\nu_r = 4.8$ THz. The bulk Raman phonon frequency (ν_b) of α-Sn is calculated to be, in our approximations, $\nu_b = 5.97$ THz (the experimental value is $\nu_b = 6.0$ THz [64]). The dipole-active rocking mode is therefore predicted to resonate with bulk vibrations, falling however in a region of relatively low bulk density of phonon states (see Fig. 4.15), and should be visible in high-resolution EELS. It is of interest to notice that the same rocking mode is predicted to lie, in the asymmetric buckled structure of Si(100)[63], at $\nu_r \sim 6$ THz, well below the bulk zone-center Raman phonon ($\nu_b \sim 16$ THz). This difference is attributable to the stronger buckling of the α-Sn dimer. We then calculated the effective charge corresponding to this dipole-active "rocking mode". Starting with the optimized atomic configuration (Table 4.5) of the 2 × 1 asymmetric dimer reconstruction, we shrunk slightly (0.1 Å) the surface asymmetric dimers

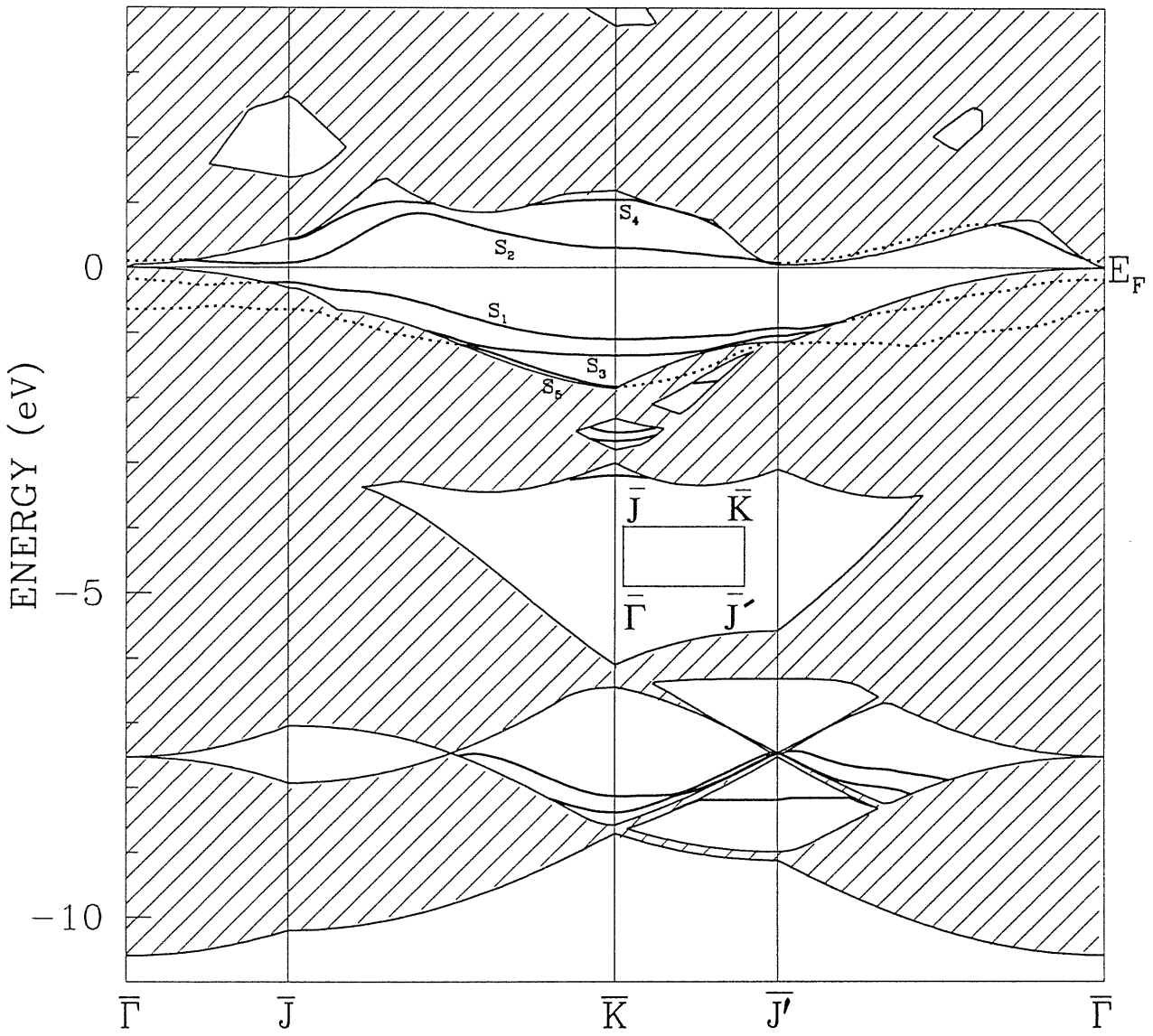

Figure 4.10: Surface electronic band structure of the α-Sn(100) (2 × 1) asymmetric dimer reconstructed surface reported along high-symmetry lines of the (2 × 1) rectangular irreducible Brillouin zone. The Fermi level is set to zero. Shaded areas correspond to surface-projected bulk states, while thicker lines correspond to surface states. The irreducible surface Brillouin zone is given in the inset. Note the surface bands S_1 and S_2 well separated in energy due to the large buckling tetween the dimer atoms, and the Fermi level in between them.

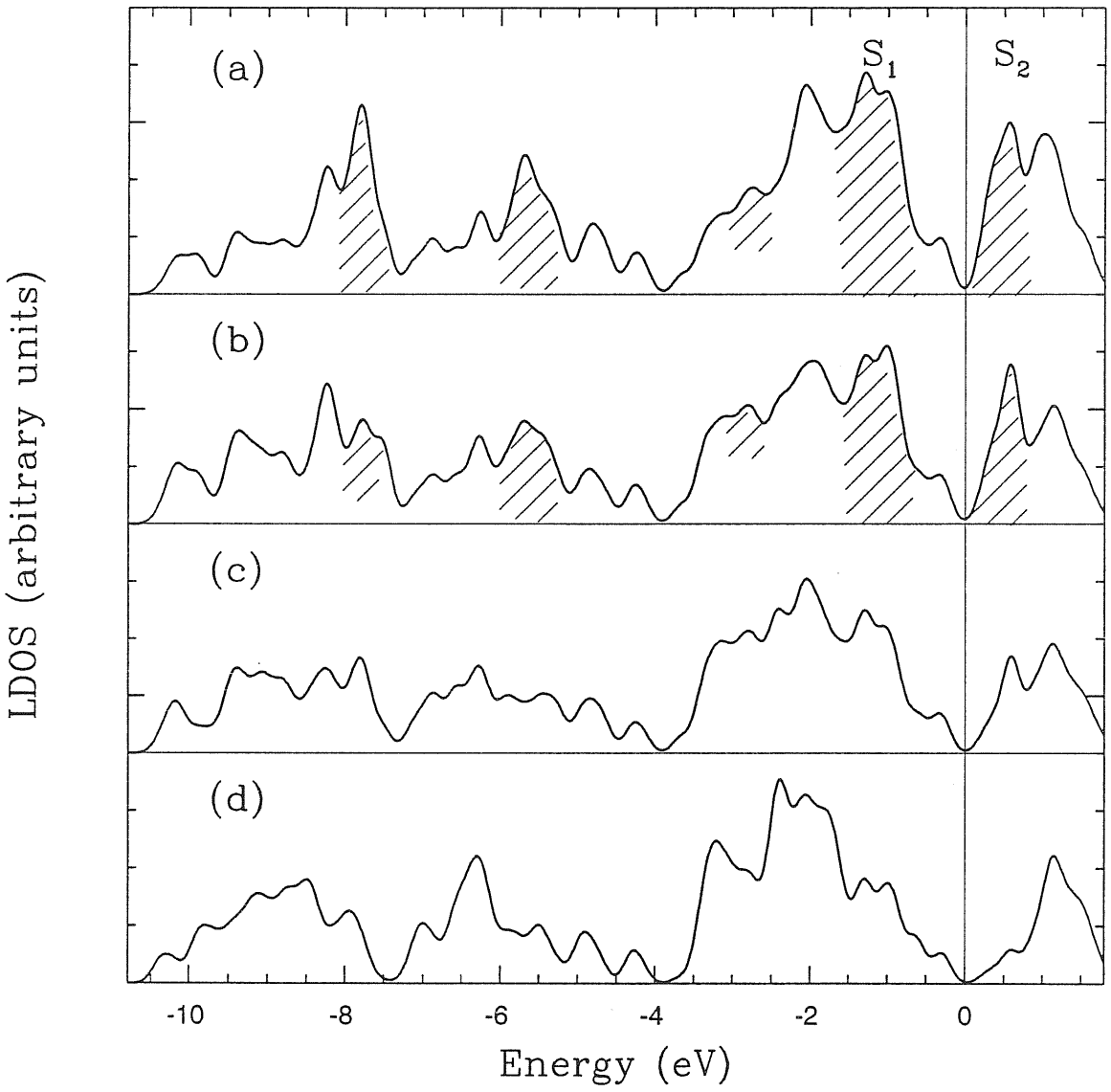

Figure 4.11: Layer-projected density of states (LDOS) for the 2×1 asymmetric dimer reconstructed α-Sn (100) surface (12-layers slab calculation). The Fermi level is set to zero. In panel (a), (b), (c) and (d) the solid curves are, respectively, the density of states (DOS) projected on the surface layer, the second layer, the third layer and the center layer (sixth layer) whereas the DOS projected on the center layer produced a good bulk DOS. The LDOS of panel (c) very similar to that of panel (d) indicates that the surface states are primarily related to the surface layer and second layer reconstructure. Shaded areas indicate the surface states. Note the insulating feature of LDOS in panel (a).

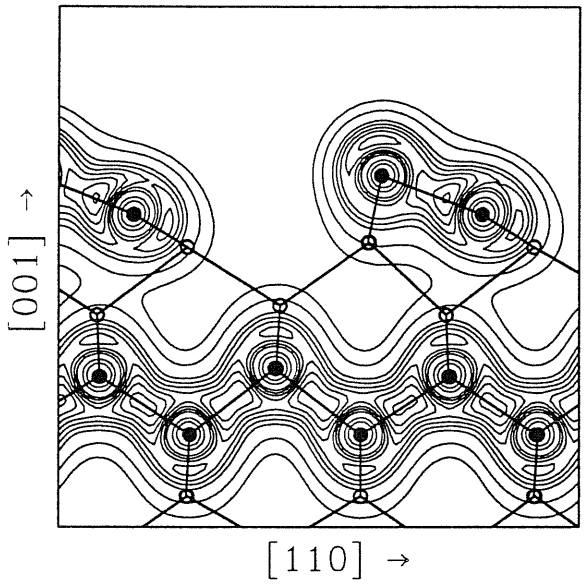

Figure 4.12: Geometry, and total electron density contour of the (2 × 1) asymmetric dimer reconstructed surface, on the (110) plane passing through the Sn atoms represented by full circles, empty circles indicate the out-plane Sn atoms, and thicker straight lines to bonds among Sn atoms. Contour lines are separated by 0.005 (a.u.). Note a giant buckling between the two dimer atoms, and a strong covalent bond formed in the dimer.

along the [001] direction. The effective charge was calculated by means of the King-Smith-Vanderbilt formula[65], and turned out to be 0.8e. This large vibrating dipole should make the rocking mode observation feasible.

The large charge transfer from the down atom to the up atom of the asymmetric dimer should, if screening effects are ignored, induce an increase of the surface work function relative to that of the symmetric dimer case. We computed, as in the

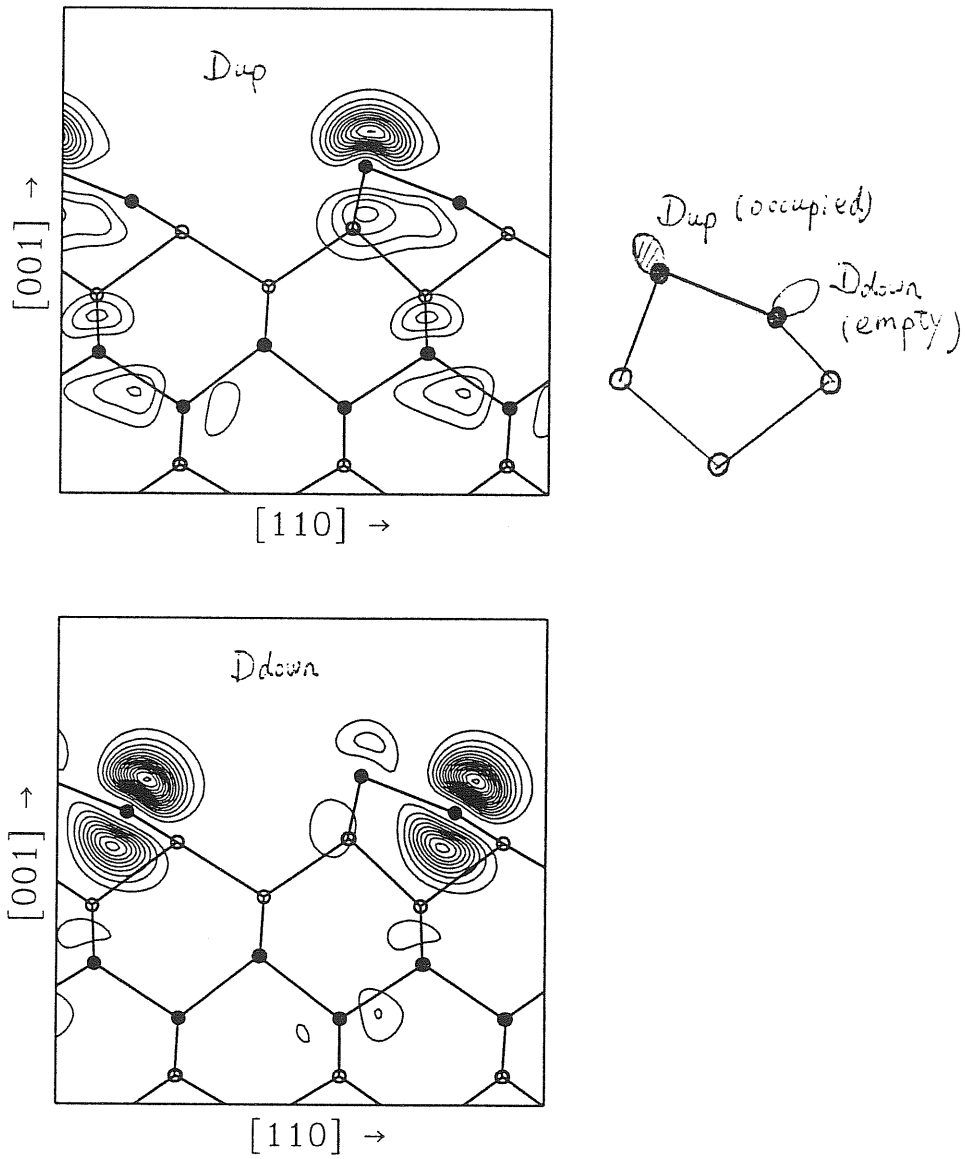

Figure 4.13: Electron density contours of the filled surface S_1 eigenstate (the upper panel, filled up state D_{up}) and of the empty surface S_2 eigenstate (the lower panel, empty down state D_{down}) in the (2×1) asymmetric dimer reconstruction at $\bar{K}$, on the (110) plane passing through the Sn atoms represented by full circles, empty circles indicate the out-plane Sn atoms, and thicker straight lines to bonds among Sn atoms. Contour lines are separated by 0.0005 (a.u.). Note the strong s-like state feature in the upper panel and the strong p-like state feature in the lower panel.

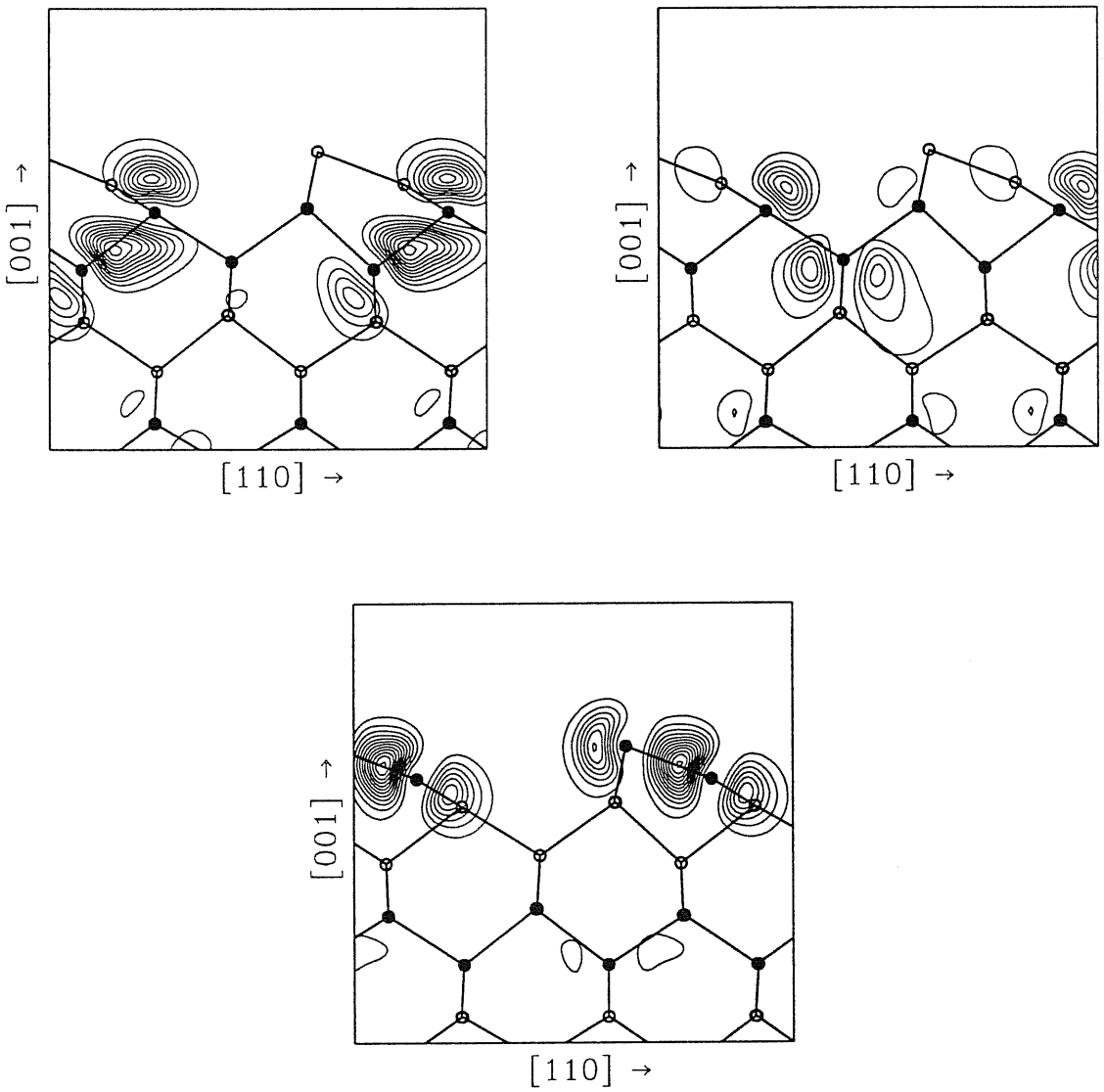

Figure 4.14: Electron density contours of the filled surface S_3 eigenstate (upper left panel), of the empty surface S_4 eigenstate (upper right panel), and of the filled surface S_5 eigenstate (lower panel) in the (2×1) asymmetric dimer reconstruction at $\bar{K}$, on the (110) plane passing through the Sn atoms represented by full circles, empty circles indicate the out-plane Sn atoms, and thicker straight lines to bonds among Sn atoms. Contour lines are separated by 0.0005 (a.u.). Note in the upper left and right panels the back-bond surface states S_3 and S_4 related to the first layer atoms whereas the electrons localized, and in the lower panel surface state S_5 corresponding to the formation of bonding in the dimer.

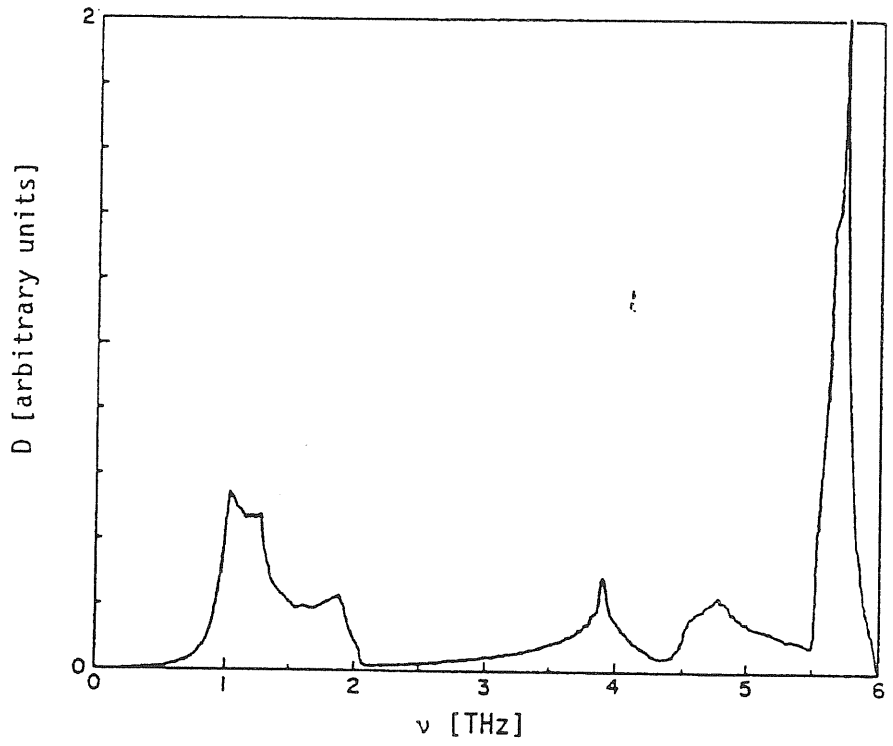

Figure 4.15: The phonon spectrum for α-Sn. From Ref. [64]. Note there is a gap around 4.4 THz.

symmetric dimer case, the planar and macroscopic averages of the Hartree potential, reported in Fig.4.5(c), and found that the surface work function is instead 4.43 eV, very much the same as that of the symmetric dimer surface (Table 4.1). Hence, we concluded that the screening effects are very strong, which is reasonable as Sn is a semimetal. Therefore the measurement of the surface work function can not make a distinction bewteen the asymmetric dimer reconstruction and the symmetric dimer reconstruction. The fundamental difference between them lies in the electronic band

structure, as mentioned above, the former being insulating, with a 1.2 eV energy gap in the surface bands, the latter being metallic.

4.4 Reconstructions Based on Asymmetric Dimers

4.4.1 Brief Review

In Si(100) and Ge(100) surfaces, a series of reconstructions are observed in experiments [66, 67, 68, 69, 70], such as (2×1), $c(4 \times 2)$, $p(2 \times 2)$, $c(2 \times 2)$, $c(4 \times 4)$, and $(2 \times n)$ where $6 < n < 10$. Several of the above reconstructions commonly coexist on those surfaces. The 2×1 reconstruction is a room temperature phase. The $(2 \times n)$ reconstructions $(6 < n < 10)$ are instead obtained by rapid quenching from high temperatures, they are metastable, and decay with first-order kinetics[67]. Exposing (2×1) surfaces to a hydrogen dosage, and annealing at 570-690°C, induces the formation of a $c(4 \times 4)$ reconstruction on Si(100)[71, 72]. Finally, the $c(4 \times 2)$, $p(2 \times 2)$, and $c(2 \times 2)$ reconstructions predominate at low temperatures. As for the groud state, theoretical calculations[16, 15, 61] and experiments[68, 70] confirm that the $c(4 \times 2)$ or $p(2 \times 2)$ are nearly degenerate.

Pandey[73] proposed a "missing dimer defect" model to account for the observed complicated reconstructions on (100) surfaces. However, *ab initio* calculation by Roberts and Needs[61] showed the missing dimer defect model to be energetically higher than the 2×1 asymmetric dimer model. Currently, only the metastable reconstructions $(2 \times n)$ $(6 < n < 10)$ and $c(4 \times 4)$ reconstruction are explained in terms of the missing dimer defect model: the former as the ordering of excess missing dimer defects[67], the latter as an ordered structure with missing dimer defects

formed on the basic 2×1 structure[72]. The stable reconstructions 2×1, $c(4 \times 2)$, $p(2 \times 2)$ and $c(2 \times 2)$ are instead believed to be formed by different arrangements of two non-equivalent asymmetric dimers (see Fig. 4.16).

Generally speaking, the reconstructions based on asymmetric dimers as building blocks can be classified, according to the group theoretical argument[74, 75], in three families, namely, a "2×1" family with a (2×1) backbone, a "2×2" family with a (2×2) backbone, and a "$c(2 \times 2)$" family with a $c(2 \times 2)$ backbone. Among them, the reconstructions belonging to the "2×2" family have only one half of the surface atoms dimerized in their unit cells, and they are never observed in experiments. The typical reconstruction geometries of the "2×1" and "$c(2 \times 2)$" families are instead schematically shown in Fig. 4.16.

The surface energies of reconstructions belonging to the same family are very similar, and their structures are connected by transformation paths that do not involve breaking of bonds among the surface and bulk. Thus, structural transitions within each family can readily take place. The surface energies of the "$c(2 \times 2)$" family are higher than those of the "2×1" family, for Si(100) and Ge(100) surfaces[16]. Moreover, structural transitions from the "$c(2 \times 2)$" family to the "2×1 family are hindered, since a huge amount of energy is needed to break and displace the strong dimer bonds and the bonds related to the domain walls when these two families of reconstructions coexist on the surfaces. In practice, the realization of a given reconstruction strongly depends upon the surface-preparation conditions. In some special conditions, both "2×1" and "$c(2 \times 2)$" families can be created on the same surface with stable domain walls among them[76, 68].

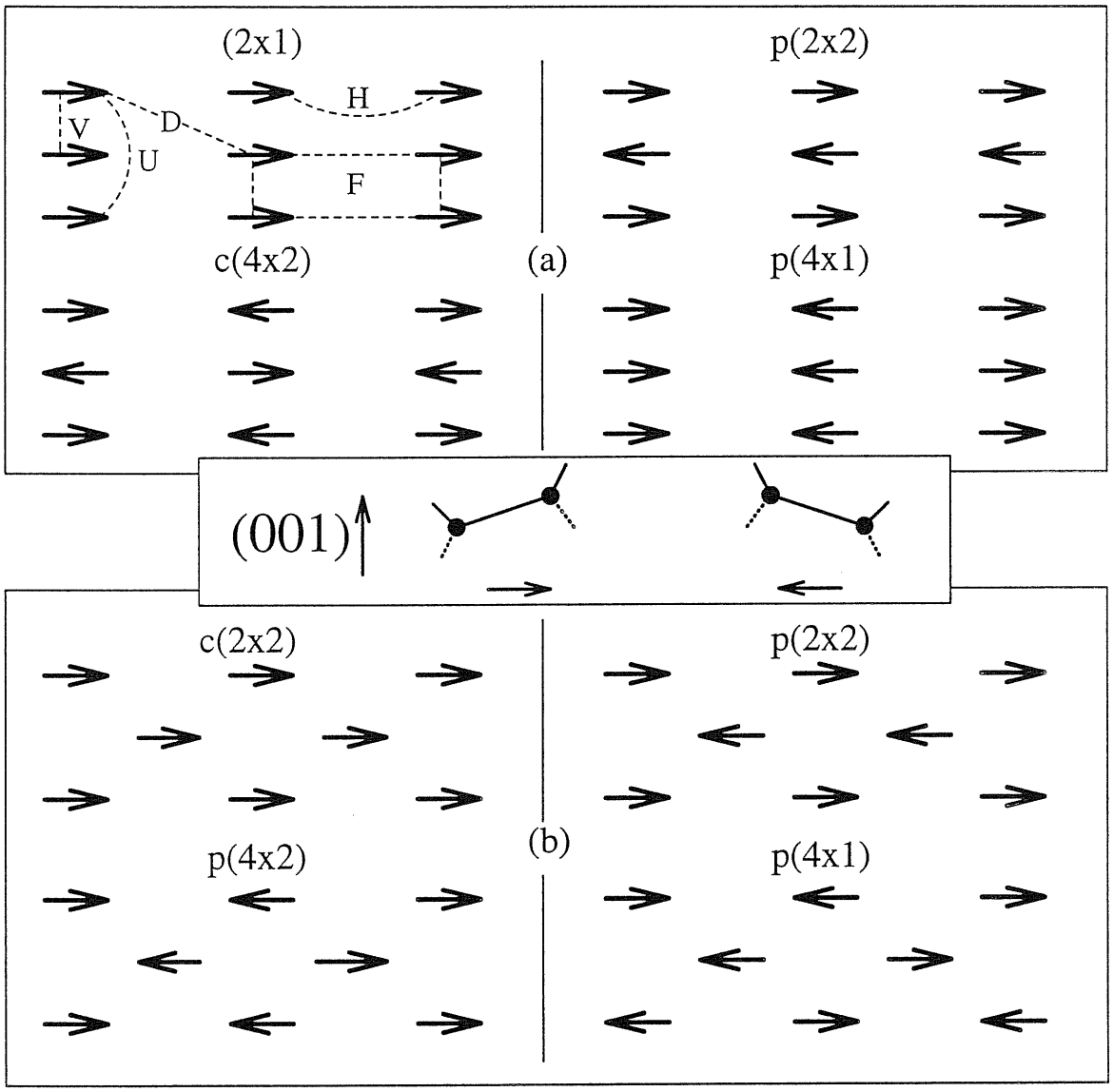

Figure 4.16: Arrangements of asymmetric buckled dimers on α-Sn(100) for the "2 × 1" family (a), and "$c(2 \times 2)$" family (b). Side views of the oppositely oriented asymmetric dimers are shown in the inset. Coupling constants corresponding to the mapped Ising-Hamiltonian (4.2) are indicated for the "2 × 1" family (a).

The recent RHEED experiment by Yuen *et al*[6] discovered reconstructions such as two-domain 2×1, $c(2 \times 2)$, $p(2 \times 2)$, and $c(4 \times 4)$ also on α-Sn(100) surfaces. It is tempting to assign these reconstructions on Sn(100) to the same mechanisms proposed for Si(100) and Ge(100), asymmetric dimers being the basic building blocks, and perhaps missing dimer defects being involved. However, we have to remind ourselves that in the experiment[6] the Sn(100) surface is obtained by molecular beam epitaxy onto InSb(100), and the role of the misfit strain energy could be very important[77], as indicated by successive transformations as a function of epitaxial layer thickness[6].

We therefore carried out a series of surface energy calculations for some of the possible higher-order reconstructions, in order to clarify their hierarchy on α-Sn(100). Our calculated surface energies for the considered reconstructions are schematically shown in Fig.4.17, and Table 4.3 summarizes our calculated results.

We constructed the atomic configurations starting from the previously calculated symmetric-dimer and asymmetric-dimer data. We then relaxed the atomic configurations guided by the calculated Hellmann-Feynman forces. The computational method and related aspects such as the energy cutoff and the k-point sampling have been described in the previous chapter and sections.

4.4.2 $c(2 \times 2)$ Reconstruction

We here consider the "$c(2 \times 2)$" family of reconstructions (Fig. 4.16(b)). Since it is known that on Si(100)[16] the basic $c(2 \times 2)$ reconstruction has the lowest energy among this family, we chose the $c(2 \times 2)$ reconstruction as the representative of the

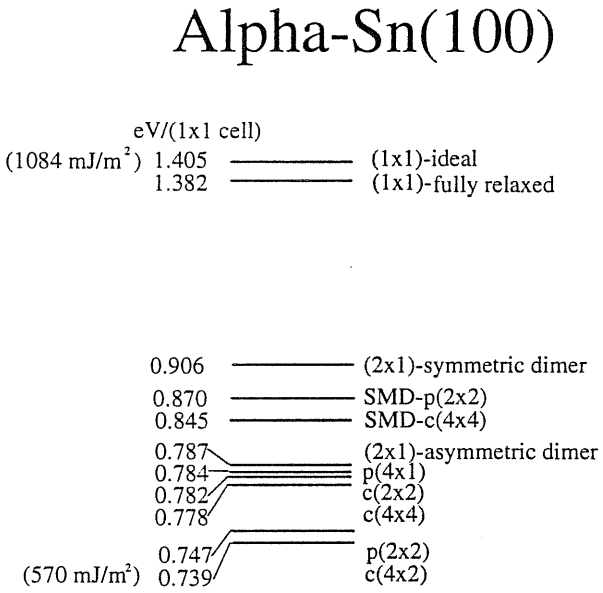

Figure 4.17: The calculated surface energies for α-Sn(100) surfaces

"$c(2 \times 2)$" family on α-Sn(100). We first constructed the atomic configuration using the symmetric dimer coordinates (Table 4.4), then we relaxed it. The calculated surface energy is 0.883 eV/(1 × 1 cell), slightly lower than that of the 2×1 symmetric dimer reconstruction (Table 4.3), but much higher (0.096 eV/(1 × 1 cell)) than that of the 2×1 asymmetric dimer reconstruction (Table 4.3).

Next, we removed the mirror symmetry between the two dimerized atoms, allow the dimer to become asymmetric, and let the atomic configuration relax to equilibrium. The optimized atomic configuration of the top six layers is reported in Table 4.6. The dimer buckling is 1.03 Å, almost identical to that of 2×1 asymmetric dimer reconstruction (Table 4.3). The surface energy is 0.782 eV/(1 × 1 cell), which is also almost identical to that of the 2×1 asymmetric dimer reconstruction (Table

4.3). The similarity shown by this calculation between the $c(2 \times 2)$ reconstructions of Sn(100) and Si(100), suggests that other "$c(2 \times 2)$" family reconstructions are also not competitive in the search for low temperature stable phases. We therefore concentrate our attention on the "2×1" family reconstructions.

4.4.3 $p(4 \times 1)$ Reconstruction

Within the "2×1" family, the $p(4 \times 1)$ reconstruction, to our knowledge, has never been observed in experiments. However, the calculation of the surface energy for this reconstruction, will provide, combined with other "2×1" family reconstructions calculations, a relevant information about the interaction structure of dimers on (100) surfaces. This will enable us, in Sect. 4.4.6, to study some finite temperature properties of α-Sn(100) surfaces.

The initial atomic configuration is constructed using the asymmetric dimer coordinates (Table 4.5), and equilibrium was reached after a short relaxation. Table 4.7 gives the optimized atomic positions of the top six layers. The buckling of the dimers is 0.964 Å, a little smaller if compared with 2×1 asymmetric dimers. The calculated surface energy is 0.784 eV/(1×1 cell), almost degenerate with the 2×1 asymmetric dimer reconstruction.

We notice that the mirror symmetry about [110] (the dimer itself is in $[1\bar{1}0]$ direction) between the two dimers and also that between the atoms in layers below are slightly lifted (see Table 4.7) (also in the following calculations). This is because the original C_2 symmetry about [001] of a semi-infinite surface is absent in the slab, as in the *ab initio* calculation for Ge(100) by Needels *et. al.* [78]. In Ref.[78], it was

confirmed by recovering this symmetry by hands that this was a negligible effect for the surface energy.

4.4.4 $c(4 \times 2)$ Reconstruction

Ab initio calculations[15, 78] have shown that the $c(4 \times 2)$ reconstruction is the most favorable in Si(100) and Ge(100), and the large-thickness data for α-Sn grown on InSb(100) also show a $c(4 \times 2)$ structure. The $c(4 \times 2)$ reconstruction is obviously one of the best candidates for the true ground state of α-Sn(100).

We have constructed the initial atomic configuration using the asymmetric dimer coordinates (Table 4.5). At variance with the previous cases, here the surface unit cell is not square or rectangular, but is instead oblique. We carefully dealt with the k-point sampling, as described in Sect. 4.1. We first relaxed this atomic configuration to equilibrium with four special k-points in the $c(4 \times 2)$ ISBZ. We then increased the number of k-points to sixteen special points, and found the calculated surface energy to be converged within 3 meV/(1×1 cell). The final atomic positions of the top six layers are reported in Table 4.8. The buckling of the dimer is 1.06 Å, a little larger than in the 2×1 asymmetric dimer case. The final surface energy is 0.739 eV/(1×1 cell), i.e. 48 meV/(1×1 cell) lower than that of the 2×1 asymmetric dimer reconstruction.

We mention here that the reflection symmetry through the (110) plane in the optimized atomic configuration is a little broken, as also happened in previous *ab initio* calculations for the $c(4 \times 2)$ reconstruction on Ge(100)[78]. This is attributable to the fact that the k-integration over the $c(4 \times 2)$ oblique ISBZ cannot be sampled

exactly to make the electron charge density retain this symmetry in an exact manner. However, we do not believe that this slight asymmetry has any consequences, and we ignore it.

4.4.5 $p(2 \times 2)$ Reconstruction

The $p(2 \times 2)$ reconstruction is the other good candidate for the true ground state of α-Sn(100). We started our calculation from the atomic configuration constructed through an appropriate arrangement of asymmetric dimers (Table 4.5), and we relaxed the atoms to the optimal positions. We give the optimized atomic positions of the top six layers in Table 4.9. The buckling of the dimer is here 1.05 Å. As expected, the calculated surface energy of 0.747 eV/(1×1 cell) is very close to that of the $c(4 \times 2)$ reconstruction. These two structures are calculated to be almost degenerate also in Si(100) and Ge(100) surfaces. Experimental data[6] show that the $p(2 \times 2)$ structure prevails when the coverage of α-Sn grown on InSb is between 500 Å and 1000 Å , while $c(4 \times 2)$ structure is not seen.

In order to provide a comparison with future experiments, we have calculated the electronic band structure of the $p(2 \times 2)$ reconstruction and reported it in Fig. 4.18. The main features of the band structure are identical to those observed for the 2×1 asymmetric dimer reconstruction, namely, the filled surface band and empty surface band are separated by a gap of about 1.2 eV and they both lie in the fundamental gap region of the projected bulk band structure. Also the surface rocking mode frequency (4.8 THz) and effect charge (0.8 e), as well as the surface work function (4.43 eV) should be the same, within our accuracy, as those of the 2×1 asymmetric

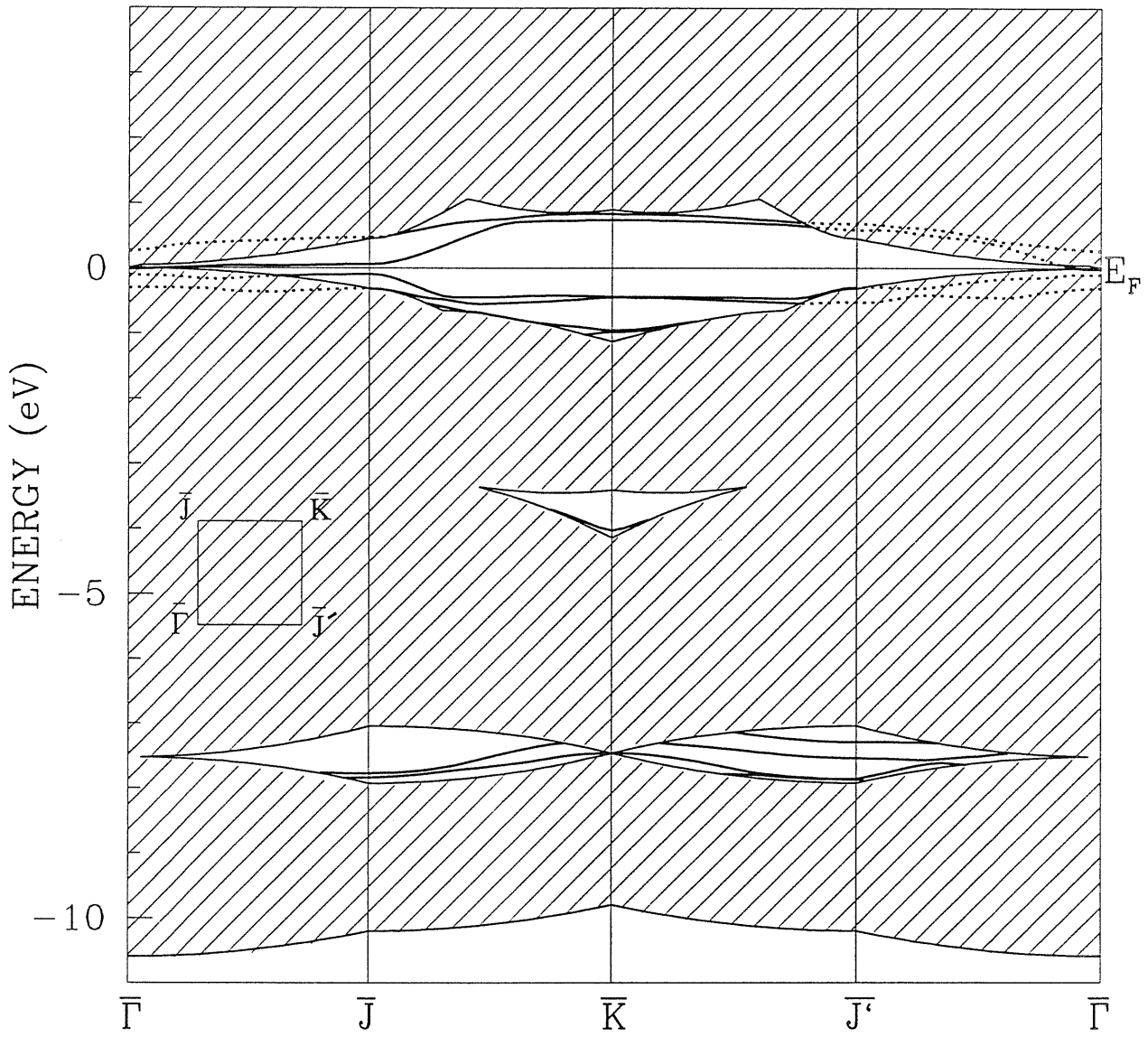

Figure 4.18: Surface electronic band structure of the α-Sn(100) $p(2 \times 2)$ reconstructed surface reported along high-symmetry lines of the (2×2) square irreducible Brillouin zone. The Fermi level is set to zero. Shaded areas correspond to surface-projected bulk states, while thicker lines correspond to surface states. The irreducible surface Brillouin zone is given in the inset. Note that the surface bands in the fundamental gap region are well separated in energy.

dimer reconstruction.

4.4.6 Interaction between Asymmetric Dimers: Phenomenological

Based on the above results, we can develop a phenomenological model for the interaction among asymmetric dimers which are basic building blocks for the reconstructions on Sn(100). We do this in analogy with the work of Ihm *et al*[16] on Si(100). Two possible orientations can be assigned to the asymmetric dimers. The dimer orientations can therefore be represented by the two possible states of an Ising spin-1/2. In this view, the $c(4 \times 2)$ reconstruction corresponds to the antiferromagnetic phase, the $p(2 \times 2)$ to the layered-antiferromagnetic phase, and so on. Assuming that the energy differences between the possible reconstructions with asymmetric dimers are primarily due to the interaction among the asymmetric dimers, we are able to map these reconstructions onto an effective two-dimensional Ising model, in which the energy differences between different reconstructions are translated into a set of interaction energies of the Ising model. There is an abundance of existing results and powerful computational tools for the two-dimensional Ising model[79, 80]. Using this mapping, it was originally predicted that in Si(100) and Ge(100) surfaces, a second-order phase transition takes place from the ordered reconstruction, $c(4\times2)$ or $p(2\times2)$, to a disordered 2×1 structure with a transition temperature in the range of 200 to 250 K[16]. Even if this model is not rich enough to describe in detail the true phase transition (seen experimentally around 170 K on Si and Ge (100)[81, 82]) it does set the right temperature scale.

The following is the effective Ising Hamiltonian corresponding to the "2×1"

family reconstructions, which includes all interactions up to twice the surface atom spacing (as illustrated in Fig.4.16(a))[16],

$$\begin{aligned} -\mathcal{H} = \; & V\sum_{ij}\sigma_{ij}\sigma_{ij+1} + H\sum_{ij}\sigma_{ij}\sigma_{i+1j} + D\sum_{ij}\sigma_{ij}\sigma_{i+1j\pm1} \\ & + U\sum_{ij}\sigma_{ij}\sigma_{ij+2} + F\sigma_{ij}\sigma_{ij}\sigma_{ij+1}\sigma_{i+1j}\sigma_{i+1j+1}, \end{aligned} \tag{4.2}$$

where σ_{ij} is the Ising spin at the lattice site (ij) with two possible values ±1. In practice, the couplings U and F are set to zero since they give the same contribution to the ground-state energy for all considered reconstructions, and also because we lack the sufficient informations to determine them (fortunately, they are not the nearest neighbor couplings). The other coupling constants V, H and D can be extracted from the energy differences among the calculated "2×1" family reconstructions.

Since the potential barrier for flipping dimers is about 120 meV/(1×1 cell)(this value corresponds to the energy difference between asymmetric dimer and symmetric dimer), a very large barrier if compared with the energy differences between the considered reconstructions, here the spin wave mechanism in this effective Ising model is negligible at low temperatures. Thus, considering the configurations 2×1, $p(2\times2)$, $c(4\times2)$ and $p(4\times1)$ leads to the following set of equations for the interaction energies per dimer:

$$-\mathcal{H}_{2\times1} = V + H + 2D, \tag{4.3}$$

$$-\mathcal{H}_{p(2\times2)} = -V + H - 2D, \tag{4.4}$$

$$-\mathcal{H}_{c(4\times2)} = -V - H + 2D, \tag{4.5}$$

$$-\mathcal{H}_{p(4\times1)} = V - H - 2D. \tag{4.6}$$

Using the results of Table 4.3, we subtract equation (4.3) from equations (4.4),

(4.5) and (4.6), respectively, and we obtain,

$$\begin{aligned} 2(V+2D) &= -80\ meV/dimer\ , \\ 2(V+H) &= -96\ meV/dimer\ , \\ 2(H+2D) &= -6\ meV/dimer\ . \end{aligned} \tag{4.7}$$

This yields the following values for the coupling constants:

$$V = -42.5\ meV/dimer\ , \quad H = -5.5\ meV/dimer\ , \quad D = 1.25\ meV/dimer\ . \tag{4.8}$$

The effective Ising Hamiltonian (4.2) is now completely determined, similarly to the previous work on Si(100) and Ge(100)[16]. One could, at this point, employ the renormalization group or Monte Carlo simulations to calculate and predict the thermodynamic quantities and critical properties, such as, the second-order phase transition temperature from ordered phase to disordered phase[16]. Such an approach is, for the time being, outside the scope of this thesis. Comparing the effective Ising Hamiltonian (4.2) with that of Si(100)[16], the ratio of the leading terms V between them is 42.5/26, ~ 1.63. Thus, roughly speaking, the disordering transition temperature on α-Sn(100) can be obtained from the transition temperature on Si(100) (about 250 K) as $1.63 \times 250K \approx 400K$.

An alternatively and more reliable way to compute the transition temperature is to consider the simpler effective Ising Hamiltonian containing nearest-neighbor interactions only. This is obtained if the couplings D, U and F in Hamiltonian (4.2) are set to zero. Physically, the interactions among dimers originate from their electric dipoles, thus the main contribution to the interaction energies comes from the nearest neighbor interaction. This is confirmed by the solution (4.8), where the coupling D is much smaller than the others. In fact, such a simplified effective Ising

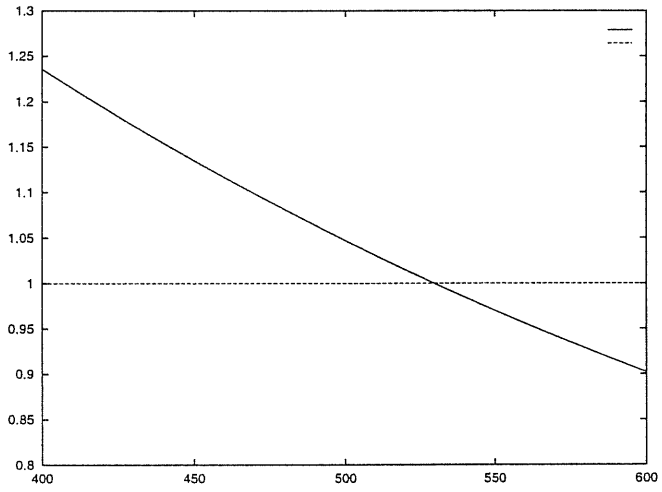

Figure 4.19: Equation (4.9) is numerically solved.

Hamiltonian is a standard Onsager lattice model, for which a complete collection of well-documented exact results exists[83]. In particular, for a given Onsager lattice, there is a single critical temperature T_c below which the Onsager lattice possesses a spontaneous magnetization. Above T_c a disordered phase prevails. This critical temperature T_c can be obtained[83] as a solution of the following equation:

$$|z_1 z_2| + |z_1| + |z_2| = 1 \ , \tag{4.9}$$

where $z_1 = \tanh(\beta V)$, $z_2 = \tanh(\beta H)$ and $\beta = 1/k_B T$, k_B being the Boltzmann's constant. The couplings V and H can be easily derived using the surface energies

of the $c(4 \times 2)$, $p(2 \times 2)$, and 2×1 asymmetric dimer reconstructions as,

$$V = -40\ meV/dimer\ , \quad H = -8\ meV/dimer\ . \tag{4.10}$$

Fig. 4.19 shows the solution of equation (4.9) obtained using the parameters (4.10). One can see that the phase transition temperature, from the ordered reconstruction, $p(2 \times 2)$ or $c(4 \times 2)$, to a disordered 2×1 phase, for Sn(100) is roughly 530 K. This temperature is much higher than the transition temperature of bulk α-Sn into β-Sn (290 K). Even if α-Sn(100) can be clearly stabilized epitaxially on a substrate, as is the case on InSb(100), it seems unlikely that this dimer disordering phase transition might become observable on α-Sn(100).

4.4.7 $c(4 \times 4)$ Reconstruction

A $c(4 \times 4)$ reconstruction was also observed to prevail for larger layer thickness of α-Sn(100) grown on InSb(100) between 1000 Å and 2500 Å [6]. Hence this reconstruction also competes for the true ground state.

In this subsection, we consider the $c(4 \times 4)$ reconstruction without missing dimer defects. It is easy to map the $c(4 \times 4)$ reconstructions onto the effective Ising Hamiltonian (4.2), and analyze its possibility of competing for the ground state. In the last subsection we have shown that the energy gain of the ordered reconstructed phase was mainly arising from the 'antiferromagnetic' interaction energy $-V$. Actually, no matter how we arrange the asymmetric dimers in the $c(4 \times 4)$ unit cell, the 'antiferromagnetic' interaction energies $-V$ are always balanced by the 'ferromagnetic' interaction energies V, so that they cancel each other. We can therefore speculate that the surface energy of the $c(4 \times 4)$ reconstructions is close to that of

2×1 asymmetric dimer reconstruction, and is thus disfavored for the ground state, as compared with $p(2 \times 2)$ and $c(4 \times 2)$ reconstructions.

Since this seems at variance with experiment, we decided to evaluate microscopically the surface energy for one of the $c(4 \times 4)$ reconstructions. Again, its initial atomic configuration is constructed from the asymmetic dimer coordinates (Table 4.5). This is the most costly calculation we have performed since a total of 96 Sn atoms are contained in the slab. The final relaxed atomic positions of the top three layers are listed in Table 4.10. We see that the buckling of dimers is 1.02 Å. The calculated surface energy is 0.778 eV/(1×1 cell), very close as actually suggested by the Ising modeling to the surface energy (0.787 eV/(1×1 cell)) of 2×1 asymmetric dimer case. We can thus conclude that our $c(4 \times 4)$ reconstruction is not competitive in the form assumed.

4.4.8 Reconstructions Containing Missing Dimer Defects

Upon removal of a dimer from (100) surfaces, the atoms underneath immediately will form new bonds with an overall reduction of two in the number of dangling bonds, and some energy gain is introduced. However, this process is also likely to introduce a considerable amount of strain into the system, and should be largely disfavored if the fraction of the removed dimers is large. As mentioned in the Introduction, both *ab initio* calculations[61] and experiments[67] confirm that reconstructions with missing dimer defects are very high in energy, and they only appear as metastable phases, or high-temperatures phases on Si(100). A similar situation is expected on Sn(100) surfaces.

In this subsection we consider two possible missing dimer defect reconstructions, and we calculate their surface energies as representative of the whole class. First, we consider the so-called "single missing dimer $p(2 \times 2)$ reconstruction" in which the surface cell is constructed taking the $p(2 \times 2)$ cell, and removing one of the dimers. Such a reconstruction corresponds to a large fraction (1/2) of dimers being removed. The present calculation is technically similar to that of the previous $p(2 \times 2)$ reconstruction. The starting atomic configuration is taken from the previous optimized $p(2 \times 2)$ coordinates (Table 4.9), with removing of a dimer. We have then fully relaxed it. The final atomic positions of the top six layers are reported in Table 4.11. The buckling of the remaining dimers turns out to be 1.05 Å, while the atoms underneath rearrange substantially giving rise to the formation of new bonds, about 3.40 Å long. They thus are very weak bonds (the bulk bond is 2.79 Å long). The optimized surface energy is 0.870 eV/(1 × 1 cell) much higher than that of the 2×1 asymmetric dimer reconstruction, as expected. Our calculation indicates that the strain energy, induced by removal of the dimer and by the subsequent rebonding of the second-layer atoms, largely overcomes the energy gain brought about by elimination of the two dangling bonds.

Next we consider the so-called "single missing dimer $c(4 \times 4)$ reconstruction", where, as its name suggests, the surface cell is taken to be the $c(4 \times 4)$ cell, and one of four dimers is removed. This reconstruction corresponds to a smaller fraction (1/4) of dimers being removed. Several arrangements of a missing dimer defect are possible in the $c(4 \times 4)$ surface cell. However, they are expected to be roughly degenerate based upon the approach of mapping the dimers onto the Ising-spin Hamiltonian.

For the microscopic calculation, we have constructed the initial atomic configuration using the relaxed $c(4 \times 4)$ atomic positions (Table 4.10), and removed one dimer. After a quite long relaxation process, we obtained the equilibrium atomic positions, listed for the top four layers in Table 4.12. The surface energy of this reconstruction is 0.845 eV/(1 × 1 cell), which is still substantially higher than that of the 2×1 asymmetric dimer reconstruction.

In conclusion, removal of dimers on α-Sn(100) appears to be too costly in all cases. In particular, it does not provide an explanation for the $c(4 \times 4)$ structure observed on α-Sn(100) grown on InSb(100), which remains at this stage an open problem.

4.4.9 Discussion

If looking at Table 4.3, and Table 4.5 to 4.10, it is found that in all reconstructions considered, the asymmetric dimers are essentially identical, namely have the same buckling (about 1 Å), buckling angles (about 21°), and bond lengths (about 2.83 Å), including the missing dimer defect reconstructions. Except for the $c(4 \times 2)$ and $p(2 \times 2)$ reconstructions which are lowest, all surface energies are identical within 10 meV/(1 × 1 cell) with respect to that of the 2×1 asymmetric dimer reconstruction (excluding the missing dimer reconstructions, much higher). Moreover the electronic band structures of the $p(2 \times 2)$ and 2×1 asymmetric dimer reconstructions are very similar. All these show that in possible reconstructions of α-Sn(100) the asymmetric buckled dimers have rigid structures, and the energy gain induced by them are identical.

Table 4.2: The magnitude of buckling, the bond length, and the buckling angle of a dimer in C, Si, Ge, and α-Sn (100) surfaces.

	buckling length (Å)	bond length (Å)	buckling angle
C[a]	0	1.37	0°
Si[b]	0.4	2.47	9°
Ge[c]	0.74	2.46	17.5°
α-Sn[d]	1.01	2.82	20.99°

[a] Reference [10] (calculated value).
[b]Reference [11, 84] (measured value).
[c]Referenec [12] (measured value).
[d]This work.

Why do the $c(4 \times 2)$ and $p(2 \times 2)$ reconstructions have the lowest surface energy, at least in the calculations? In Sect. 4.4.6, we have phenomenologically dealt with this question based upon the mapping of 2×1 family reconstructions onto the effective Ising model, and found that the primary contribution to the energy gain of the $c(4 \times 2)$ and $p(2 \times 2)$ reconstructions relative to others is the nearest neighbor antiferromagnetic interaction $-V$.

Physically, it has been shown for Ge(100) surfaces[78] that the energy gain, of $c(4 \times 2)$ and $p(2 \times 2)$ reconstructions with respect to the 2×1 asymmetric dimer one, comes primarily from the relaxations of the atoms in the layer below the dimers. In Ref. [78] two calculations were done for the $c(4 \times 2)$ reconstruction on Ge(100), in one of which the second-layer atoms were allowed to relax, and in the other

one the second-layer atoms were fixed to their corresponding bulk positions, and it was found that the latter was almost degenerate with the 2×1 asymmetric dimer case, and the former brought about an energy gain of 0.05 eV/dimer due to the relaxation of the second-layer atoms. Here we have also done the similar calculation for α-Sn(100) $p(2 \times 2)$ reconstruction. We fixed the second layer atoms (of course, including the two innermost layer atoms) in their bulk-like positions, and relaxed all other atoms. The surface energy turned out to be 0.818 eV/(1×1 cell). Looking at Fig.4.20 and checking Tables 4.8, 4.9 and 4.5, we see that for the $c(4\times2)$ and $p(2\times2)$ reconstructions the atoms in the second layer have free space to move towards the "up" atom of the dimer and away from the "down" atom along the [110] direction (note the dimer itself lies in $[1\bar{1}0]$ direction). In $p(2 \times 2)$ or $c(4 \times 2)$ they do that, in order to keep the bond length close to the bulk value. On the other hand, in the 2×1 asymmetric dimer reconstruction they can not do it along [110] for lack of space due to their two sides being both the up dimer atoms or down dimer atoms. Moreover, the positions of the second-layer atoms are similar for $c(4\times2)$ and $p(2\times2)$ reconstructions, which explains why they are energetically quite close. The surface energy of the $p(4 \times 1)$ reconstruction is a little lower (3 meV/(1×1 cell)) than that of the 2×1 asymmetric dimer one, which can again be understood by noting that atoms in the second layer have more freedom along the $[1\bar{1}0]$ direction in the former. The difference along the $[1\bar{1}0]$ direction between the $c(4 \times 2)$ and $p(2 \times 2)$ reconstructions is the same as that between the $p(4 \times 1)$ and the 2×1 asymmetric dimer reconstructions. It is thus understood why the $c(4\times2)$ reconstruction is a bit lower (8 meV/(1×1 cell)) in energy than the $p(2 \times 2)$ one.

In conclusion, we have found that a basic 2×1 asymmetric dimer should be responsible for the reconstructions of α-Sn(100). The dimer buckling is predicted to be $\sim 21°$ or ~ 1 Å , much larger than the corresponding ones for Si and Ge(100), which is again in the trend from C to Si, to Ge , and to α-Sn (see Table 4.2). The associated surface state gap should be at least 1.2 eV (LDA calculations only provide a lower bound). A surface rocking mode resonance having a frequency of 4.8 THz, is predicted with a large effective charge. It should be visible in the surface phonon spectrum at $\vec{k}_{//} = 0$. The lowest energy reconstructions are found to be the $c(4 \times 2)$ and $p(2 \times 2)$, which are energetically almost degenerate.

Experimental observations on epitaxially grown films of α-Sn(100) on InSb(100) reveal, as a function of increasing thickness, the sequence $2\times1 \rightarrow p(2\times2) \rightarrow c(4\times4)$. We believe we have a good picture for the first two, while we do not understand the $c(4 \times 4)$ structure. More work is also needed in order to understand what disfavors the $c(4 \times 2)$ relative to the $p(2 \times 2)$, and why the basic 2×1 structure prevails for small thicknesses.

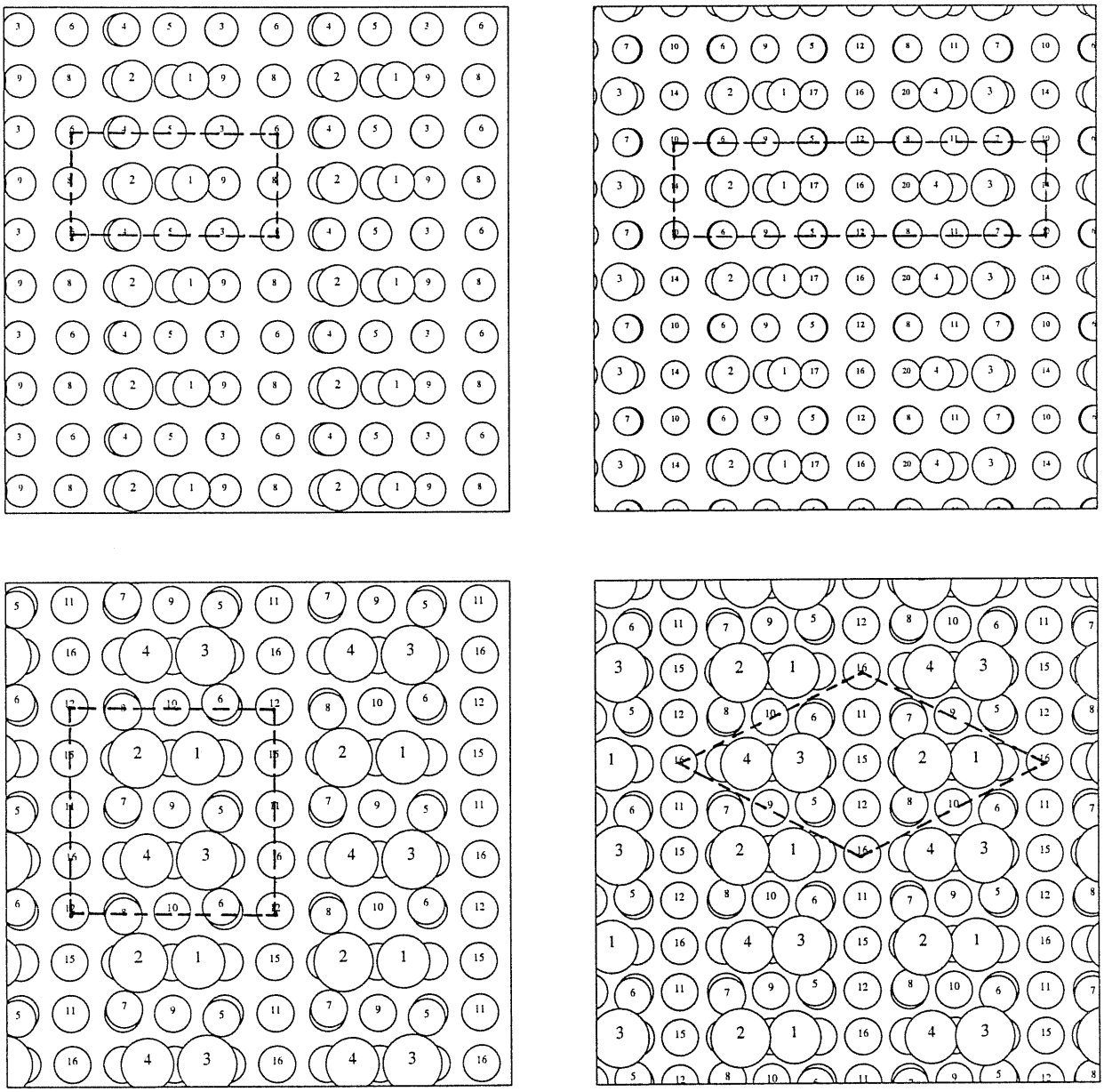

Figure 4.20: Top view of the optimized 2 × 1 asymmetric dimer (upper left panel), $p(4 \times 1)$ (upper right panel), $p(2 \times 2)$ (lower left panel) and $c(4 \times 2)$ (lower right panel) reconstructions. The numbers labeled on the atoms correspond to those in Table 4.5, 4.7, 4.9 and 4.8, respectively.

Table 4.3: Calculated surface energies, absolute E_{surf} and relative ΔE, dimer buckling b, dimer buckling angle ω, and dimer bond length d of different optimized reconstructions for α-Sn (100) surface. In the table SMD indicates single missing dimer.

Structure	E_{surf}		ΔE	b	ω	d
	[eV/(1×1 cell)]	$[mJ/m^2]$	[eV/(1×1 cell)]	(Å)		(Å)
ideal	1.405	1084	0.000			
fully relaxed	1.382	1066	-0.023			
2×1 symmetric	0.906	699	-0.499	0	0°	2.90
SMD-$p(2 \times 2)$	0.870	671	-0.535	1.05	21.15°	2.91
SMD-$c(4 \times 4)$	0.845	652	-0.560	1.09	22.29°	2.87
2×1 asymmetric	0.787	607	-0.618	1.01	20.99°	2.82
$p(4 \times 1)$	0.784	605	-0.621	0.964	20.06°	2.81
$c(2 \times 2)$	0.782	603	-0.623	1.03	20.88°	2.89
$c(4 \times 4)$	0.778	600	-0.627	1.02	20.80°	2.87
$p(2 \times 2)$	0.747	576	-0.658	1.06	21.60°	2.88
$c(4 \times 2)$	0.739	570	-0.666	1.06	21.67°	2.87

Table 4.4: Optimized atomic positions of the α-Sn(100) symmetric dimer 2 × 1 reconstructed surface, and the corresponding bulk-like (Ideal) positions. In the rectangular supercell, coordinates are given by $\mathbf{r} = c_1\mathbf{a}_1 + c_2\mathbf{a}_2 + c_3\mathbf{a}_3$, where $\mathbf{a}_i$ is defined in the conventional cubic coordinate system as $\mathbf{a}_1 = (a_0/2)(1,1,0)$, $\mathbf{a}_2 = (a_0/2)(1,-1,0)$, $\mathbf{a}_3 = a_0(0,0,-1)$ with a_0=12.181 a.u.=6.446 Å as α-Sn lattice parameter. The unit cell has one symmetric dimer.

	Atom	Ideal			Optimized		
	no.	c_1	c_2	c_3	c_1	c_2	c_3
dimer-layer							
	1	.250	-.500	1.375	.250	-.318	1.349
	2	.250	.500	1.375	.250	.318	1.349
2nd-layer							
	3	-.250	-.500	1.125	-.250	-.492	1.132
	4	-.250	.500	1.125	-.250	.492	1.132
3rd-layer							
	5	-.250	.000	.875	-.250	.000	.869
	6	-.250	1.000	.875	-.250	1.000	.893
4th-layer							
	7	.250	.000	.625	.250	.000	.618
	8	.250	1.000	.625	.250	1.000	.637
5th-layer							
	9	.250	-.500	.375	.250	-.507	.378
	10	.250	.500	.375	.250	.507	.378
6th-layer							
	11	-.250	-.500	.125	-.250	-.500	.125
	12	-.250	.500	.125	-.250	.500	.125

Table 4.5: Optimized atomic positions of the α-Sn(100) asymmetric dimer 2×1 reconstructed surface, and the corresponding bulk-like (Ideal) positions. In the rectangular supercell, coordinates are given by $\mathbf{r} = c_1\mathbf{a}_1 + c_2\mathbf{a}_2 + c_3\mathbf{a}_3$, where $\mathbf{a}_i$ is defined in the conventional cubic coordinate system as $\mathbf{a}_1 = (a_0/2)(1,1,0)$, $\mathbf{a}_2 = (a_0/2)(1,-1,0)$, $\mathbf{a}_3 = a_0(0,0,-1)$ with a_0=12.181 a.u.=6.446 Å as α-Sn lattice parameter. The unit cell has one asymmetric dimer.

	Atom	Ideal			Optimized		
	no.	c_1	c_2	c_3	c_1	c_2	c_3
dimer-layer							
dimer-down	1	.500	.250	1.375	.500	.550	1.266
dimer-up	2	.500	1.250	1.375	.500	1.128	1.423
2nd-layer							
	3	.000	.250	1.125	.000	.247	1.133
	4	.000	1.250	1.125	.000	1.208	1.154
3rd-layer							
	5	.000	.750	.875	.000	.755	.859
	6	.000	1.750	.875	.000	1.717	.899
4th-layer							
	7	.500	.750	.625	.500	.740	.612
	8	.500	1.750	.625	.500	1.744	.642
5th-layer							
	9	.500	.250	.375	.500	.233	.376
	10	.500	1.250	.375	.500	1.252	.377
6th-layer							
	11	.000	.250	.125	.000	.250	.125
	12	.000	1.250	.125	.000	1.250	.125

Table 4.6: Optimized atomic positions of the α-Sn(100) $c(2 \times 2)$ reconstructed surface, and the corresponding bulk-like (Ideal) positions. In the square supercell, coordinates are given by $\mathbf{r} = c_1\mathbf{a}_1 + c_2\mathbf{a}_2 + c_3\mathbf{a}_3$, where $\mathbf{a}_i$ is defined in the conventional cubic coordinate system as $\mathbf{a}_1 = (a_0/2)(1.1, 0)$, $\mathbf{a}_2 = (a_0/2)(1, -1, 0)$, $\mathbf{a}_3 = a_0(0, 0, -1)$ with a_0=12.181 a.u.=6.446 Å as α-Sn lattice parameter. The unit cell has one asymmetric dimer.

	Atom	Ideal			Optimized		
	no.	c_1	c_2	c_3	c_1	c_2	c_3
dimer-layer							
dimer-up	1	.500	.250	1.375	.500	.409	1.414
dimer-down	2	.500	1.250	1.375	.500	1.001	1.255
2nd-layer							
	3	.000	.250	1.125	.033	.264	1.133
	4	.000	1.250	1.125	-.033	1.264	1.133
3rd-layer							
	5	.000	.750	.875	-.031	.757	.876
	6	.000	1.750	.875	.031	1.757	.876
4th-layer							
	7	.500	.750	.625	.500	.758	.647
	8	.500	1.750	.625	.500	1.757	.602
5th-layer							
	9	.500	.250	.375	.500	.272	.375
	10	.500	1.250	.375	.500	1.240	.375
6th-layer							
	11	.000	.250	.125	.000	.250	.125
	12	.000	1.250	.125	.000	1.250	.125

Table 4.7: Optimized atomic positions of the α-Sn(100) $p(4 \times 1)$ reconstructed surface, and the corresponding bulk-like (Ideal) positions. In the rectangular supercell, coordinates are given by $\mathbf{r} = c_1\mathbf{a}_1 + c_2\mathbf{a}_2 + c_3\mathbf{a}_3$, where $\mathbf{a}_i$ is defined in the conventional cubic coordinate system as $\mathbf{a}_1 = (a_0/2)(1,1,0)$, $\mathbf{a}_2 = (a_0/2)(1,-1,0)$, $\mathbf{a}_3 = a_0(0,0,-1)$ with a_0=12.181 a.u.=6.446 Å as α-Sn lattice parameter. The unit cell has two dimers A and B.

	Atom	Ideal			Optimized		
	no.	c_1	c_2	c_3	c_1	c_2	c_3
dimer-layer							
dimer-A-down	1	.500	.250	1.375	.500	.567	1.271
dimer-A-up	2	.500	1.250	1.375	.500	1.147	1.421
dimer-B-up	3	.500	2.250	1.375	.500	2.351	1.419
dimer-B-down	4	.500	3.250	1.375	.500	2.932	1.271
2nd-layer							
	5	.000	.250	1.125	.000	.265	1.138
	6	.000	1.250	1.125	.000	1.229	1.150
	7	.000	2.250	1.125	.000	2.272	1.148
	8	.000	3.250	1.125	.000	3.236	1.140
3rd-layer							
	9	.000	.750	.875	.000	.769	.861
	10	.000	1.750	.875	.000	1.749	.910
	11	.000	2.750	.875	.000	2.734	.860
	12	.000	3.750	.875	.000	3.749	.890
4th-layer							
	13	.500	.750	.625	.500	.752	.613
	14	.500	1.750	.625	.500	1.751	.650
	15	.500	2.750	.625	.500	2.747	.612
	16	.500	3.750	.625	.500	3.751	.634
5th-layer							
	17	.500	.250	.375	.500	.246	.375
	18	.500	1.250	.375	.500	1.265	.378
	19	.500	2.250	.375	.500	2.234	.377
	20	.500	3.250	.375	.500	3.255	.375
6th-layer							
	21	.000	.250	.125	.000	.250	.125
	22	.000	1.250	.125	.000	1.250	.125
	23	.000	2.250	.125	.000	2.250	.125
	24	.000	3.250	.125	.000	3.250	.125

Table 4.8: Optimized atomic positions of the α-Sn(100) $c(4 \times 2)$ reconstructed surface, and the corresponding bulk-like (Ideal) positions. In the oblique supercell (two side lengths of the surface cell are $\sqrt{2}\,a_0$ and $\sqrt{2.5}\,a_0$, respectively, and the angle of the two sides is 116.57°), coordinates are given by $\mathbf{r} = c_1\mathbf{a}_1 + c_2\mathbf{a}_2 + c_3\mathbf{a}_3$, where $\mathbf{a}_i$ is defined in the conventional cubic coordinate system as $\mathbf{a}_1 = (a_0/2)(1,1,0)$, $\mathbf{a}_2 = (a_0/2)(1,-1,0)$, $\mathbf{a}_3 = a_0(0,0,-1)$ with a_0=12.181 a.u.=6.446 Å as α-Sn lattice parameter. The unit cell has two dimers *A* and *B*.

	Atom	Ideal			Optimized		
	no.	c_1	c_2	c_3	c_1	c_2	c_3
dimer-layer							
dimer-*A*-down	1	.500	.250	1.375	.501	.506	1.259
dimer-*A*-up	2	.500	1.250	1.375	.509	1.093	1.423
dimer-*B*-up	3	1.500	.250	1.375	1.500	.421	1.424
dimer-*B*-down	4	1.500	1.250	1.375	1.508	1.008	1.259
2nd-layer							
	5	.000	.250	1.125	-.042	.278	1.135
	6	1.000	.250	1.125	1.042	.278	1.134
	7	.000	1.250	1.125	.050	1.237	1.136
	8	1.000	1.250	1.125	.966	1.234	1.132
3rd-layer							
	9	.000	.750	.875	-.008	.758	.856
	10	1.000	.750	.875	.993	.756	.854
	11	.000	1.750	.875	.002	1.756	.899
	12	1.000	1.750	.875	.998	1.757	.898
4th-layer							
	13	.500	.750	.625	.493	.755	.608
	14	1.500	.750	.625	1.494	.748	.607
	15	.500	1.750	.625	.500	1.754	.639
	16	1.500	1.750	.625	1.500	1.754	.644
5th-layer							
	17	.500	.250	.375	.499	.242	.377
	18	1.500	.250	.375	1.500	.240	.373
	19	.500	1.250	.375	.500	1.265	.374
	20	1.500	1.250	.375	1.500	1.263	.377
6th-layer							
	21	.000	.250	.125	.000	.250	.125
	22	1.000	.250	.125	1.000	.250	.125
	23	.000	1.250	.125	.000	1.250	.125
	24	1.000	1.250	.125	1.000	1.250	.125

Table 4.9: Optimized atomic positions of the α-Sn(100) $p(2 \times 2)$ reconstructed surface, and the corresponding bulk-like (Ideal) positions. In the square supercell, coordinates are given by $\mathbf{r} = c_1\mathbf{a}_1 + c_2\mathbf{a}_2 + c_3\mathbf{a}_3$, where $\mathbf{a}_i$ is defined in the conventional cubic coordinate system as $\mathbf{a}_1 = (a_0/2)(1,1,0)$, $\mathbf{a}_2 = (a_0/2)(1,-1,0)$, $\mathbf{a}_3 = a_0(0,0,-1)$ with a_0=12.181 a.u.=6.446 Å as α-Sn lattice parameter. The unit cell has two dimers A and B.

	Atom	Ideal			Optimized		
	no.	c_1	c_2	c_3	c_1	c_2	c_3
dimer-layer							
dimer-A-down	1	.500	.250	1.375	.500	.505	1.267
dimer-A-up	2	.500	1.250	1.375	.500	1.094	1.429
dimer-B-up	3	1.500	.250	1.375	1.500	.423	1.431
dimer-B-down	4	1.500	1.250	1.375	1.500	1.009	1.266
2nd-layer							
	5	.000	.250	1.125	-.044	.279	1.140
	6	1.000	.250	1.125	1.044	.279	1.140
	7	.000	1.250	1.125	.044	1.236	1.139
	8	1.000	1.250	1.125	.956	1.236	1.139
3rd-layer							
	9	.000	.750	.875	-.001	.757	.859
	10	1.000	.750	.875	1.001	.757	.859
	11	.000	1.750	.875	.000	1.757	.903
	12	1.000	1.750	.875	1.000	1.757	.903
4th-layer							
	13	.500	.750	.625	.500	.761	.611
	14	1.500	.750	.625	1.500	.743	.609
	15	.500	1.750	.625	.500	1.766	.645
	16	1.500	1.750	.625	1.500	1.744	.646
5th-layer							
	17	.500	.250	.375	.500	.249	.376
	18	1.500	.250	.375	1.500	.232	.377
	19	.500	1.250	.375	.500	1.273	.378
	20	1.500	1.250	.375	1.500	1.257	.377
6th-layer							
	21	.000	.250	.125	.000	.250	.125
	22	1.000	.250	.125	1.000	.250	.125
	23	.000	1.250	.125	.000	1.250	.125
	24	1.000	1.250	.125	1.000	1.250	.125

Table 4.10: Optimized atomic positions of the α-Sn(100) $c(4 \times 4)$ reconstructed surface, and the corresponding bulk-like (Ideal) positions. In the square supercell, coordinates are given by $\mathbf{r} = c_1\mathbf{a}_1 + c_2\mathbf{a}_2 + c_3\mathbf{a}_3$, where $\mathbf{a}_i$ is defined in the conventional cubic coordinate system as $\mathbf{a}_1 = (a_0/2)(1,1,0)$, $\mathbf{a}_2 = (a_0/2)(1,-1,0)$, $\mathbf{a}_3 = a_0(0,0,-1)$ with a_0=12.181 a.u.=6.446 Å as α-Sn lattice parameter. The unit cell has four dimers *A*, *B*, *C*, and *D*.

	Atom	Ideal			Optimized		
	no.	c_1	c_2	c_3	c_1	c_2	c_3
dimer-layer							
dimer-*A*-up	1	.500	.250	1.375	.500	.409	1.421
dimer-*A*-down	2	.500	1.250	1.375	.500	.998	1.261
dimer-*B*-down	3	1.500	.250	1.375	1.474	.525	1.260
dimer-*B*-up	4	1.500	1.250	1.375	1.511	1.109	1.420
dimer-*C*-down	5	.500	2.250	1.375	.500	2.549	1.252
dimer-*C*-up	6	.500	3.250	1.375	.500	3.126	1.409
dimer-*D*-down	7	-.500	.250	1.375	-.475	.525	1.261
dimer-*D*-up	8	-.500	1.250	1.375	-.512	1.109	1.420
2nd-layer							
	9	.000	.250	1.125	.049	.265	1.130
	10	1.000	.250	1.125	.950	.265	1.130
	11	-1.000	.250	1.125	-.991	.252	1.132
	12	.000	2.250	1.125	-.009	2.252	1.132
	13	.000	1.250	1.125	-.043	1.226	1.135
	14	1.000	1.250	1.125	1.042	1.226	1.135
	15	-1.000	1.250	1.125	-.999	1.217	1.147
	16	.000	3.250	1.125	-.002	3.218	1.147
3rd-layer							
	17	.000	.750	.875	.001	.749	.854
	18	1.000	.750	.875	1.000	.749	.853
	19	-1.000	.750	.875	-.995	.759	.858
	20	.000	2.750	.875	-.004	2.759	.858
	21	.000	1.750	.875	-.001	1.735	.888
	22	1.000	1.750	.875	1.002	1.735	.887
	23	-1.000	1.750	.875	-1.002	1.734	.904
	24	.000	3.750	.875	.002	3.734	.903

4th-layer							
	25	.500	.750	.625	.500	.739	.607
	26	1.500	.750	.625	1.501	.748	.607
	27	-.500	.750	.625	-.500	.749	.607
	28	.500	2.750	.625	.500	2.743	.614
	29	.500	1.750	.625	.500	1.745	.635
	30	1.500	1.750	.625	1.509	1.752	.640
	31	-.500	1.750	.625	-.509	1.752	.640
	32	.500	3.750	.625	.500	3.741	.643
5th-layer							
	33	.500	.250	.375	.500	.228	.374
	34	1.500	.250	.375	1.499	.238	.373
	35	-.500	.250	.375	-.499	.238	.374
	36	.500	2.250	.375	.500	2.238	.374
	37	.500	1.250	.375	.500	1.252	.374
	38	1.500	1.250	.375	1.501	1.260	.375
	39	-.500	1.250	.375	-.501	1.261	.375
	40	.500	3.250	.375	.500	3.253	.376
6th-layer							
	41	.000	.250	.125	.000	.250	.125
	42	1.000	.250	.125	1.000	.250	.125
	43	-1.000	.250	.125	-1.000	.250	.125
	44	.000	2.250	.125	.000	2.250	.125
	45	.000	1.250	.125	.000	1.250	.125
	46	1.000	1.250	.125	1.000	1.250	.125
	47	-1.000	1.250	.125	-1.000	1.250	.125
	48	.000	3.250	.125	.000	3.250	.125

Table 4.11: Optimized atomic positions of the α-Sn(100) "single missing dimer" $p(2 \times 2)$ reconstructed surface, and the corresponding bulk-like (Ideal) positions. In the square supercell, coordinates are given by $\mathbf{r} = c_1\mathbf{a}_1 + c_2\mathbf{a}_2 + c_3\mathbf{a}_3$, where $\mathbf{a}_i$ is defined in the conventional cubic coordinate system as $\mathbf{a}_1 = (a_0/2)(1,1,0)$, $\mathbf{a}_2 = (a_0/2)(1,-1,0)$, $\mathbf{a}_3 = a_0(0,0,-1)$ with a_0=12.181 a.u.=6.446 Å as α-Sn lattice parameter. The unit cell has one left dimer *A*.

	Atom	Ideal			Optimized		
	no.	c_1	c_2	c_3	c_1	c_2	c_3
dimer-layer							
dimer-*A*-down	1	.500	.250	1.375	.500	.426	1.213
dimer-*A*-up	2	.500	1.250	1.375	.500	1.021	1.375
	3	1.500	.250	1.375	removed	removed	removed
	4	1.500	1.250	1.375	removed	removed	removed
2nd-layer							
	5	.000	.250	1.125	-.109	.271	1.178
	6	1.000	.250	1.125	1.109	.271	1.178
	7	.000	1.250	1.125	.129	1.251	1.076
	8	1.000	1.250	1.125	.871	1.251	1.076
3rd-layer							
	9	.000	.750	.875	-.014	.726	.873
	10	1.000	.750	.875	1.014	.726	.873
	11	.000	1.750	.875	.004	1.801	.893
	12	1.000	1.750	.875	.996	1.801	.893
4th-layer							
	13	.500	.750	.625	.500	.747	.628
	14	1.500	.750	.625	1.500	.741	.609
	15	.500	1.750	.625	.500	1.760	.633
	16	1.500	1.750	.625	1.500	1.734	.642
5th-layer							
	17	.500	.250	.375	.500	.250	.372
	18	1.500	.250	.375	1.500	.226	.377
	19	.500	1.250	.375	.500	1.254	.382
	20	1.500	1.250	.375	1.500	1.252	.375
6th-layer							
	21	.000	.250	.125	.000	.250	.125
	22	1.000	.250	.125	1.000	.250	.125
	23	.000	1.250	.125	.000	1.250	.125
	24	1.000	1.250	.125	1.000	1.250	.125

Table 4.12: Optimized atomic positions of the α-Sn(100) "single missing dimer" $c(4 \times 4)$ reconstructed surface, and the corresponding bulk-like (Ideal) positions. In the square supercell, coordinates are given by $\mathbf{r} = c_1\mathbf{a}_1 + c_2\mathbf{a}_2 + c_3\mathbf{a}_3$, where $\mathbf{a}_i$ is defined in the conventional cubic coordinate system as $\mathbf{a}_1 = (a_0/2)(1,1,0)$, $\mathbf{a}_2 = (a_0/2)(1,-1,0)$, $\mathbf{a}_3 = a_0(0,0,-1)$ with a_0=12.181 a.u.=6.446 Å as α-Sn lattice parameter. The unit cell has three asymmetric dimers A, B, and C.

	Atom	Ideal			Optimized		
	no.	c_1	c_2	c_3	c_1	c_2	c_3
dimer-layer							
dimer-A-up	1	.500	.250	1.375	.498	.415	1.417
dimer-A-down	2	.500	1.250	1.375	.498	.999	1.250
dimer-B-down	3	1.500	.250	1.375	1.537	.491	1.244
dimer-B-up	4	1.500	1.250	1.375	1.483	1.074	1.415
dimer-C-down	5	-.500	.250	1.375	-.540	.491	1.247
dimer-C-up	6	-.500	1.250	1.375	-.483	1.075	1.418
	7	.500	2.250	1.375	removed	removed	removed
	8	.500	3.250	1.375	removed	removed	removed
2nd-layer							
	9	.000	.250	1.125	.018	.274	1.140
	10	1.000	.250	1.125	.977	.273	1.140
	11	-1.000	.250	1.125	-1.114	.265	1.169
	12	.000	2.250	1.125	.112	2.263	1.170
	13	.000	1.250	1.125	-.041	1.242	1.116
	14	1.000	1.250	1.125	1.037	1.243	1.118
	15	-1.000	1.250	1.125	-.859	1.225	1.093
	16	.000	3.250	1.125	-.139	3.224	1.092
3rd-layer							
	17	.000	.750	.875	-.003	.746	.855
	18	1.000	.750	.875	1.004	.747	.855
	19	-1.000	.750	.875	-1.016	.723	.871
	20	.000	2.750	.875	.018	2.722	.872
	21	.000	1.750	.875	-.001	1.780	.899
	22	1.000	1.750	.875	1.000	1.779	.899
	23	-1.000	1.750	.875	-.989	1.761	.893
	24	.000	3.750	.875	-.009	3.761	.894

4th-layer							
	25	.500	.750	.625	.500	.740	.610
	26	1.500	.750	.625	1.514	.755	.617
	27	-.500	.750	.625	-.512	.754	.616
	28	.500	2.750	.625	.501	2.742	.606
	29	.500	1.750	.625	.499	1.736	.643
	30	1.500	1.750	.625	1.492	1.762	.636
	31	-.500	1.750	.625	-.492	1.763	.634
	32	.500	3.750	.625	.500	3.737	.644
5th-layer							
	33	.500	.250	.375	.500	.229	.378
	34	1.500	.250	.375	1.501	.252	.373
	35	-.500	.250	.375	-.502	.249	.373
	36	.500	2.250	.375	.500	2.226	.377
	37	.500	1.250	.375	.500	1.252	.376
	38	1.500	1.250	.375	1.502	1.264	.378
	39	-.500	1.250	.375	-.502	1.263	.378
	40	.500	3.250	.375	.500	3.254	.374
6th-layer							
	41	.000	.250	.125	.000	.250	.125
	42	1.000	.250	.125	1.000	.250	.125
	43	-1.000	.250	.125	-1.000	.250	.125
	44	.000	2.250	.125	.000	2.250	.125
	45	.000	1.250	.125	.000	1.250	.125
	46	1.000	1.250	.125	1.000	1.250	.125
	47	-1.000	1.250	.125	-1.000	1.250	.125
	48	.000	3.250	.125	.000	3.250	.125

5 Summary, and Conclusions

From our *ab-initio* study of α-Sn(111), we predict that the (111) surface of α-Sn should be unstable in its unreconstructed form, and can be stabilized by various types of reconstructions.

Among the reconstructions not involving adatoms, the (2×1) π-bonded chain model is energetically favored, and is predicted to display a gigantic buckling larger than 1 Å in magnitude. This is in line with the trend towards increasing buckling in going from diamond to Si to Ge (111).

In the presence of adatoms, the adatom-restatom 2×2 reconstruction is found to be optimal energetically, and is thus the strongest candidate for the true ground state of this surface.

Recent LEED data on α-Sn(111) epitaxially grown on InSb(111)[7] display a 3×3 periodicity at low deposition temperatures, irreversibly turning into 2×2 at high temperatures. We tentatively explain the stable 2×2 structure by our adatom-restatom reconstruction.

As an attempt at understanding the metastable 3×3 phase, we have tried a DAS model, and also a distorted $\sqrt{3} \times \sqrt{3}$ adatom structure, suggested by the recent

finding of a similar 3×3 "Charge-Density-Wave"(CDW) state on α-Pb/Ge(111) [57]. The surface energies of these 3×3 structures are substantially higher than that of the 2×2 reconstruction. Among the two models tried, however, the CDW-distorted 3×3 was found to be lower in energy, even if marginally. We may therefore speculate that the observed metastable 3×3 structure could be a distorted $\sqrt{3} \times \sqrt{3}$ adatom structure similar to that of the low temperature α-Pb/Ge(111) phase.

Our *ab initio* calculations of α-Sn(100) indicate that the ideally terminated α-Sn(100) surfaces are also unstable towards reconstructions. The dimerization of the top layer atoms is, like in diamond, Si and Ge, the fundamental mechanism for α-Sn(100) reconstructions with dimers as the basic building blocks for all possible reconstructions. The dimers of α-Sn(100) are buckled with a giant buckling of about 1 Å, in agreement with the trend towards increasing buckling from diamond to Si to Ge (100). The $c(4\times2)$ and $p(2\times2)$ "antiferro" dimer reconstructions are found to be lowest in energy, and should be the ground state phase of the α-Sn(100) surface. A phase transition from an ordered phase, such as, $c(4 \times 2)$ or $p(2 \times 2)$, to a disordered phase is excluded below 500 K due to the strong interactions among the dimers.

LEED data on α-Sn(100) epitaxially grown on InSb(100) indicate, as a function of Sn thickness, first a two-domain 2×1 structure, then a $p(2 \times 2)$, then a $c(4 \times 4)$, and finally the transition to a β-Sn film. Although at this stage the precise mechanism through which the substrate influences these changes of surface periodicities is unknown, it is reasonable to speculate that the phases observed represent switches from slightly different arrangements of buckled dimers. In particular, the 2×1 structure could correspond to the basic dimer cell, while our $p(2 \times 2)$ ground state

is probably a good candidate for the intermediate phase. The final appearance of a $c(4 \times 4)$ remains somewhat mysterious, since all our attempts to build a $c(4 \times 4)$ arrangement of dimers give a higher energy. However, we note that a similar problem arises on Si(100). Exposing of Si(100) (2×1) surfaces to a hydrogen dosage higher than 10^{-2} l, then annealing at 570-690°C, induces the formation of a $c(4 \times 4)$ reconstruction of this surface[71, 72].

It is hoped that these results will stimulate further efforts towards a more detailed understanding of the α-Sn (111) and (100) surfaces.

Acknowledgments

First of all I would like to thank my supervisor Prof. Erio Tosatti for giving me a chance to study in Condensed Matter Sector of SISSA, one of the best in the world, and for introducing and guiding me to study surface sciences. Erio is indeed a great both physicist and teacher. I would also like to thank my supervisors Dr. Guido L. Chiarotti and Dr. Sandro Scandolo for their continuous guidance and assistance in whole course of this work. I am grateful to Dr. Marco Bernasconi for introducing SISSA-DFT Fortran Library to me. He was also involved in the early stage of this work. I am very happy that I can study in SISSA Car-Parrinello Molecular Dynamics Group, from which I benefit more than what I can say. Before I came to SISSA, I knew nothing about the first-principles calculation and surface sciences. Now I am confident that I can do such nice works. Let me express my thanks to them again.

I am also grateful to Prof. R. Resta, Prof. S. Baroni, Dr. S. de Gironcoli, Dario Alfe and Carlo Cavazzoni due to fruitful discussions with them. I am happy to say I have nice working days with my roommates D. Passerone, O. Ciftja, F. Franjic, L. Anton, and P. De Los Rios, and thank them for their helps. In these three years I

also obtained lots of helps from SISSA staff A. Meehan Poretti, S. Gustin, R. Iancer, A. Parma, F. Sparagna. I express my thanks to them. I would also like to express my thanks to my wife Yang Yang for her helps and patience.

This work is performed on SISSA IBM/RISC 6000 machines, and partly on Cray/C90 machines of CINECA.

Prof. Dr. Johannes Pollmann read the draft version of this thesis and gave lots of corrections and instructive suggestions. I thank him very much.

I would like to indicate that this final version of my thesis, optimized by Prof. Erio Tosatti, Dr. Guido L. Chiarotti, and Dr. Sandro Scandolo, is much different with my initial version. This, in this thesis, is another typical example of "semiconductor surface reconstructions" besides those studied.

Bibliography

[1] P.W. Anderson, Phys. Rev. Lett. **34**, 953 (1975).

[2] M. Lannoo, and P. Friedel, *Atomic and Electronic Structure of Surfaces* Springer-Verlag (Berlin 1991).

[3] M. Lannoo, and G. Allan, Phys. Rev. **B 25**, 4089 (1982).

[4] D.L. Rice and J.M. Rowe, Solid State Commun. **7**, 1433 (1969).

[5] David A. Young, *Phase Diagrams of the Elements*, University of California Press (1991).

[6] W. T. Yuen, W. K. Liu, B. A. Joyce, and R. A. Stradling, Semic. Sci. Technol. **5**, 373 (1990).

[7] T. Osaka, H. Omi, K.Yamamoto, and A. Ohtake, Phys. Rev. **B 50**, 7567 (1994).

[8] N. Takeuchi, A. Selloni, and E. Tosatti, Phys. Rev. Lett. **72**, 2227 (1994).

[9] M. Bernasconi, Guido L. Chiarotti, and E. Tosatti, Phys. Rev. Lett. **70**, 3295 (1993).

[10] P. Krüger and J. Pollmann, Phys. Rev. Lett. **74**, 1155 (1995).

[11] Physics of Solid Surfaces, edited by G. Chiarotti, Landolt-Börnstein, New Series, Group III, Vol. 24, Pt. a, page 194, (Springer, Berlin, 1993).

[12] R. Rossmann, H.L. Meyerheim, V. Jahns, J. Wever, W. Moritz, D. Wolf, D. Dornisch, and H. Schulz, Surf. Sci. **279**, 199 (1992).

[13] D.J. Chadi, Phys. Rev. Lett. **43**, 43 (1979).

[14] M. Rohlfing, P. Krüger and J. Pollmann, Phys. Rev. **B 52**, 13753 (1995).

[15] Z. Zhu, N. Shima and M. Tsukada, Phys. Rev. **B 40**, 11868 (1989).

[16] J. Ihm, D.H. Lee, J.D. Joannopoulos, J.J. Xiong, Phys. Rev. Lett. **51**, 1872 (1983).

[17] J. Ihm, A. Zunger and M.L. Cohen, J. Phys. C. **12**, 4409 (1979).

[18] P. Hohenberg, and W. Kohn, Phys. Rev. **136**, B864 (1964).

[19] W. Kohn, and L.J. Sham, Phys. Rev. **140**, A1135 (1965).

[20] D.M. Ceperley and B.J. Alder, Phys. Rev. Lett. **45**, 566 (1980); J.P. Perdew and A. Zunger, Phys. Rev. **B 23**, 5048 (1981).

[21] D.R. Hamann, M. Schluter, and C. Chiang, Phys. Rev. Lett. **43**, 1494 (1979).

[22] G.B. Bachelet, D.R.Hamann and M. Schluter, Phys. Rev. **B 26**, 4199 (1982).

[23] L.Kleinman and D.M. Bylander, Phys. Rev. Lett. **48**, 1425 (1982).

[24] R. Stumpf, X. Gonze and M. Scheffler, unpublished.

[25] E.R. Davidson, Computer Phy. Commun. **53**, 49 (1989).

[26] D.D. Johnson, Phys. Rev. **B 38**, 12087 (1988).

[27] W.H. Press *et al*, *Numerical Recipes*, Cambridge University Press (Cambridge 1986), page 307.

[28] M. Methfessel and A.T. Paxton, Phys. Rev. B **40**, 3616 (1989).

[29] A. Baldereschi, S. Baroni, and R. Resta, Phys. Rev. Lett. **61**, 734 (1988).

[30] R.W.G. Wyckoff, *Crystal Structures*, (Science Publishers, New York, 1982).

[31] C.J. Buchenauer, M.Cardona, and F.H. Pollak, Phys. Rev. **B 3**, 1243 (1971).

[32] J. Donohue, *The Structures of the Elements* (Wiley, New York, 1974).

[33] A. Jayaraman, W. Klement, Jr., and G. C. Kennedy, Phys. Rev. **130**, 540 (1963).

[34] J. Corkill, A. Garcia, and M.L. Cohen, Phys. Rev. B **43**, 9251 (1991).

[35] K.J. Chang and M.L. Cohen, Phys. Rev. **B 31**, 7819 (1985); Phys. Rev. **B 34**, 8581 (1986).

[36] J. Ihm and M.L. Cohen, Phys. Rev. **B 23**, 1576 (1981).

[37] P.W. Bridgman, Proc. Am. Acad. Arts Sci. **77**, 189 (1949).

[38] D. J. Chadi and M. L. Cohen, Phys. Rev. B **8**, 5747 (1973).

[39] N.W. Ashcroft and N.D. Mermin, Solid State Physics (Holt, Rinehart, and Winston, New York,1976), p.461.

[40] In the literature there are few papers available for the electronic band structure of β-Sn (and most of them are not complete), which are M. Miasek, Phys. Rev. **130**, 11 (1963); G. Weisz, Phys. Rev. **149**, 504 (1966); J. E. Craven, Phys. Rev. **182**, 693 (1969); M. A. E. A. Ament and A. R. de Vroomen, J. Phys. F 4. 1359 (1974); A. Svane and E. Antoncik, Phys. Rev. B **35**, 4611 (1987).

[41] Here we also tested the impact of using a slablike geometry and k-point set (k_x, k_y as that in our surface case, and a dense set along the k_z direction) to calculate the bulk energy, as Meade and Vanderbilt did in Ref. [50]. Accordingly, the bulk energy was altered by at most 0.01 eV/atom. This brought a change of the surface energies of 0.05 eV/(1 $\times$ 1 cell). However, the relative energies of different surfaces changed by less than 0.004 eV/(1 $\times$ 1 cell).

[42] S. L. Cunningham, Phys. Rev. B **10**, 4988 (1974).

[43] D. Haneman, Phys. Rev. **121**, 1093 (1961).

[44] N. Takeuchi, A. Selloni, A.I. Shkrebtii, and E. Tosatti, Phys. Rev. B **44**, 13611 (1991).

[45] K.C. Pandey, Phys. Rev. Lett. **47**, 1913 (1981), *ibid.* **49**, 223 (1982).

[46] F. Ancilotto, W. Andreoni, A. Selloni, R. Car, and M. Parrinello, Phys. Rev. Lett. **65**, 3148 (1990).

[47] S. Iarlori, G. Galli, F. Gygy, M. Parrinello, and E. Tosatti, Phys. Rev. Lett. **69**, 2947 (1992).

[48] K. Takayanagi, Y. Tanishiro, M. Takahashi, and S. Takahashi, J. Vac. Sci. Technol. A **3**, 1502 (1985); Surf. Sci. **164**, 367 (1985). .

[49] R. S. Becker, J. A. Golovchenko, and B. S. Swartzentruber, Phys. Rev. Lett. **54**, 2678 (1985); W. E. Packard and M. B. Webb, Surf. Sci. **195**, 371 (1988).

[50] R.D. Meade and D. Vanderbilt, Phys. Rev. B **40**, 3905 (1989).

[51] N. Takeuchi, A. Selloni, and E. Tosatti, Phys. Rev. Lett. **69**, 648 (1992).

[52] S. Pantelides, Phys. Rev. Lett. **58**, 1344 (1987).

[53] Zhong-Yi Lu, Guido L. Chiarotti, S. Scandolo, and E. Tosatti, unpublished.

[54] N. Takeuchi, A. Selloni, and E. Tosatti, Phys. Rev. **B 49**, 10757 (1994).

[55] E. Tosatti, Festkörperprobeleme **15**, 113 (1975).

[56] E. Tosatti, *Electronic Surface and Interface States on Metallic Systems* (eds Bertel, E. and Donath, M.) (World Scientific, Singapore, 1995).

[57] J.M. Carpinelli, H.H. Weitering, E.W. Plummer, and R. Stumpf, Nature **381**, 398 (1996).

[58] V. K. Kumikov and Kh. B. Khokonov, J. Appl. Phys. **54**, 1346 (1983).

[59] R.F.C. Farrow, D.S. Robertson, G.M. Williams, A.G. Cullis, G.R. Jones, I.M. Young, and P.N.J. Dennis, J. Cryst. Growth, **54**, 507 (1981).

[60] Andrew Zangwill, *Physics at Surfaces*, Cambridge University Press, (1988), (page 94).

[61] N. Roberts and R.J. Needs, Surf. Sci. **236**, 112 (1990).

[62] see e.g. P. Krüger and J. Pollmann, Phys. Rev. **B 38**, 10578 (1988).

[63] O.L. Alerhand and E.J. Mele, Phys. Rev. **B 35**, 5533 (1987).

[64] H. Bilz and W. Kress, *Phonon Dispersion Relations in Insulators*, (Springer-Verlag, Berlin Heidelberg, 1979.).

[65] R.D. King-Smith, and D. Vanderbilt, Phys. Rev. **B 47**, 1651 (1993).

[66] R.M. Tromp, R.J. Hamers, and J.E. Demuth, Phys. Rev. Lett. **55**, 1303 (1985) (and references therein).

[67] J.A. Martin, D.E. Savage, W. Moritz, and M.G. Lagally, Phys. Rev. Lett. **56**, 1936 (1986).

[68] R.J. Hamers, R.M. Tromp, and J.E. Demuth, Phys. Rev. **B 34**, 5343 (1986).

[69] J.A. kubby, J.E. Griffith, R.S. Becker, and J.S. Vickers, Phys. Rev. **B 36**, 6079 (1987).

[70] R.S. Becker, B.S. Swartzentruber, and J.S. Visker, J. Vac. Sci. Technol. **A 6**, 472 (1988).

[71] H. Wang, R. Lin, and X. Wang, Phys. Rev. **B 15**, 7712 (1987).

[72] K. Kato, T. Ide, T. Nishimori, and T. Ichinokawa, Surf. Sci. **207**, 177 (1988).

[73] K.C. Pandey, in *Proceedings of the International Conference on the Physics of Semiconductors*, edited by D.J. Chadi, and W.A. Harrison (Springer, New York, 1985), p. 55.

[74] I.P. Ipatova, Yu.E. Kitaev and A.V. Subashiev, Surf. Sci. **110**, 543 (1981).

[75] V.E. Zubkus, P.J. Kundrotas, S.N. Molotkov, V.V. Zatarsi, E.E. Tornau, Surf. Sci. **243**, 295 (1991).

[76] G.J.R. Jones, and B.W. Holland, Solid state Commun. **46**, 651 (1983).

[77] J.C. Phillips, Phys. Rev. Lett. **45**, 905 (1980).

[78] M. Needels, M.C. Payne, and J.D. Joannopoulos, Phys. Rev. Lett. **58**, 1765 (1987).

[79] J.M. van Leeuwen, Phys. Rev. Lett. **34**, 1056 (1975).

[80] *Phase Transition and Critical Phenomena*, edited by C. Domb and M.S. Green (Acadimic, New York, 1976), Vol. 6.

[81] S.D. Kevan, N.G. Stoffel, Phys. Rev. Lett. **53**, 702 (1984).

[82] T. Tabata, T. Aruga, Y. Murata, Surf. Sci. **179**, L63 (1987).

[83] Barry M. McCoy and Tai-Tsun Wu, *The Two-Dimensional Ising Model*, Harvard University Press, (1973), (p.89,90).

[84] B.W. Holland, Surf. Sci. **140**, L269 (1984).